# FLOW AND HEAT TRANSFER PROPERTIES OF MONO CRATERS RHYOLITES—EFFECTS OF TEMPERATURE, WATER CONTENT, AND CRYSTALLINITY

A Thesis presented to the Faculty of the Graduate School
University of Missouri

In Partial Fulfillment
of the Requirements for the Degree
Masters of Science

by
WILLIAM ROMINE
Dr. Alan G. Whittington, Thesis Supervisor
DECEMBER 2008

The undersigned, appointed by the Dean of the Graduate School, have examined the thesis

entitled:

**FLOW AND HEAT TRANSFER PROPERTIES OF MONO CRATERS RHYOLITES—EFFECTS OF TEMPERATURE, WATER CONTENT, AND CRYSTALLINITY**

Presented by William Romine
a candidate for the degree of Master of Science
And hereby certify that in their opinion it is worthy of acceptance.

_____
Alan G. Whittington

_____
Mian Liu

_____
Mark Volkmann

To my Parents, Marc and Cathy—
For helping me build the moral and intellectual foundation to cherish people and to love science.

## ACKNOWLEDGEMENTS

This work is a product of a team of dedicated individuals passionate about what they do. First, I want to extend my thanks to Dr. Alan Whittington, my advisor. I am appreciative of his patience as I learned how to tackle scientific research in the lab and increase my comfort level with computers. I also need to thank Dr. Anne Hofmeister, at Washington University in St. Louis, who graciously devoted her time and facilities to helping us gather thermal diffusivity, FTIR, and microprobe data. Next, I thank Dr. Mian Liu and Dr. Mark Volkmann for giving their time to participate in my thesis committee. Dr. Liu's expertise in computer modeling combined with Dr. Volkmann's knowledge of scientific inquiry and pedagogy helped provide unique perspectives on this experimentally-based project. Third, I am indebted to the Jack Kleinman Foundation for Volcano Research for giving me financial support for field work at Mono Craters during Summer of 2007. Sample collection from the Mono flows served as an integral part of this study and the opportunity to do geology field work was a valuable experience for me. Finally, I need to thank those people closest to me: my parents, Marc and Cathy; my step-parents, Keith and Becky; my grandparents, Lee and Jeri; my brothers, Jerod and Austin, and my best friend, Katie. These people have been with me unshakingly through the highs and lows of the past couple of years. They are always eager to ask me what is going on in the lab, and are never afraid to ask, "How is this lava flow stuff going to help people in the real world?" Inevitably, there are influential, inspiring people I am neglecting to mention—the wonderful people in my life could be a thesis in itself. My hope is that I can use the skills and maturity I've developed during this project to return the warmth I've been given.

# TABLE OF CONTENTS

## LIST OF FIGURES

## LIST OF TABLES

# FLOW AND HEAT TRANSFER PROPERTIES OF MONO CRATERS RHYOLITES—EFFECTS OF TEMPERATURE, WATER CONTENT, AND CRYSTALLINITY

**William Romine**

**Dr. Alan Whittington, Thesis Advisor**

## ABSTRACT

The nature of volcanic processes, including rate of magma ascent, exsolution of volatiles, eruption style, and flow distance, is highly dependent on the viscosity of the associated magma and its ability to transfer heat. We present measurements of the viscosity and thermal diffusivity of Quaternary rhyolitic lava flows from Mono Craters, California. We quantify the effects of temperature, dissolved water content, and crystallinity on viscosity and thermal diffusivity. We use the parallel plate and concentric cylinder methods to obtain viscosity measurements between $5 \times 10^3$ to $8 \times 10^{12}$ Pas, from superliquidus conditions to the glass transition; the laser flash (LFA) method to measure thermal diffusivity of samples between room and subliquidus temperatures. The investigated obsidian samples, collected from three different flow lobes, contain between 0.1 and 1.1 wt.% $H_2O$, and less than 2 vol.% crystals. We also remelted one sample from each lobe in a muffle furnace to produce nearly anhydrous, crystal free glass. We fit our viscosity data to four literature models relevant to rhyolitic melts, two developed specifically for rhyolites and two global models. We add to this by presenting our own models based on the empirical TVF equation and the theory-based Adam-Gibbs equation, finding that the Adam-Gibbs model works slightly better in fitting the data. We also present a model relating thermal diffusivity of the samples to their crystal contents and temperatures below the glass transition. Water has a negligible effect on thermal diffusivity at the low concentrations in the samples studied.

# Chapter 1—Introduction and Background

## 1.1 Introduction

The ability of magma to flow is a major determinant of eruption style. The goal of this study is to determine the effects of temperature, water content, crystallinity, and bubbles on the flow and heat transfer properties of obsidians from Mono Craters, California. This section will review current knowledge of viscosity and thermal diffusivity presented in the literature, including predictive models of viscosity and thermal diffusivity data presented in the literature describing the effect of composition, volatiles, crystals and bubbles on these properties. The field site for this study, Mono Craters, will also be described, including its location, eruptive history, and its importance within the realm of volcanics.

## 1.2 Rhyolites

The Mono-Inyo lava domes and craters are rhyolitic in composition. Rhyolites contain more than 72 wt.% silica. In general, dominant minerals include alkali rich feldspar, quartz, and muscovite, with lesser amounts of amphibole and biotite.

Most volcanic activity starts at the asthenosphere, from which mafic magma rises through the lithospheric mantle. Mafic magma is very hot, approaching temperatures of 1200°C. When this magma reaches the base of the continental crust, partial melting of its silica-rich components (i.e. quartz and feldspars) occurs. Having worked its way through the thick crust of the Eastern Sierra, the melts at Mono Craters are extremely enriched in silica, exceeding concentrations of 75 wt.%, by the time they reach the surface.

Rhyolitic melts tend to be very viscous due to their highly polymerized melt structures, yielding both explosive eruptions and doming. In contrast to effusive eruptions, similar to those in Hawaii and mid-ocean ridges, which extrude fluid magma, rhyolitic eruptions are usually characterized by the ejection of solid volcanic debris, including ash, glass shards, and welded tuff and breccia. When volatiles exsolve slowly, rhyolitic flows can also be effusive, as illustrated by the domes at Mono Craters.

### 1.3 Viscosity

Viscosity is arguably the most important factor controlling magma movement and ascent. It is also the major control on whether rock within the conduit will deform ductily (leading to an effusive eruption) or brittly (leading to an explosive eruption) when subjected to the stresses associated with magma ascent and volatile exsolution. The viscosity of a Newtonian material is defined as the ratio of stress to strain rate (Dingwell, 1995). Over the past forty years, workers have extensively measured and modeled viscosities of rhyolitic silicate melts, as they relate to temperature, water content, and crystal and bubble fractions.

Shaw (1963) and Friedman et al. (1963) made some of the first viscosity measurements on rhyolitic glasses. Shaw (1963) concluded that most granitic melts should have viscosities between $10^7$ and $10^4$ Pas at temperatures at or above the liquidus. At temperatures extending to 100 °C or more below the liquidus, it is expected that the magma would behave virtually as a Newtonian fluid (Shaw, 1963). Bottinga and Weill (1972) and Shaw (1972) expanded on this by proposing that viscosity can be considered to be Arrhenian over a narrow range above and near the liquidus:

$$\log \eta = A + B/T \quad (1.1)$$

where η is viscosity and A and B are constants and T is in K.

More recent viscosity data and models applicable to rhyolites include Stephenson et al (1996), Dingwell et al (1996), Hess and Dingwell (1996), Zhang et al (2003), Giordano et al (2006), Hui and Zhang (2007), and Giordano et al (2008). Stephenson et al (1996) collected viscosity data near the glass transition on six obsidians with water contents between 0 and 0.4 wt.% as the foundation for a model relating viscosity at the glass transition to cooling rate of the glass based on results from previous studies, concluding that activation energy of enthalpy relaxation is identical with that of viscous flow (Scherer, 1984). This study found an Arrhenian relationship between viscosity and temperature over the range of $10^8$ and $10^{11}$ Pas. Over a large temperature range, however, viscosity is not Arrhenian, and is commonly modeled with the TVF equation:

$$\log \eta = A + B/(T-C) \quad (1.2)$$

where η is viscosity, A, B, and C are constants, and T is temperature in K.

Hess and Dingwell (1996) propose a general TVF model for granites and rhyolites to temperature and water content based on a compilation of literature data:

$$\log \eta = [-3.545 + 0.833 \ln(w)] + [9601 - 2368 \ln(w)] / \{T - [195.7 + 32.25 \ln(w)]\} \quad (1.3)$$

where *w* is weight percent water and T is temperature in K. This model allows calculation of the viscosity of hydrous (0-12.5 wt% $H_2O$) leucogranitic melts from $10^2$ to $10^{13}$ Pas. The equation is a multiple nonlinear least-squares regression of a data set of 111 viscosity determinations in the literature (Hess and Dingwell 1996).

Zhang et al. (2003) developed a non-Arrhenian model for Mono Craters obsidians, relating fluidity (1/η) to temperature and water content:

$$\log \eta = -\log\{\exp(18.5611 - 49584/T) + \exp[1.47517 - (1795.5/T)^{1.9448}]x^{1+(1812.2/T)2}\} \quad (1.4)$$

where x is the mole fraction of water on a single oxygen basis and T is in K.

This model is based on experimental data covering a viscosity range of $10^9$ to $10^{15}$ Pas at temperatures and water contents of 570 to 1920 K and 0.0006 to 8.2 wt% respectively. These measurements were based on the kinetics of hydrous species reactions in the melt upon cooling (i.e., based on the equivalence between the glass-transition temperature and the apparent equilibrium temperature), as well as data from bubble-growth experiments (Zhang et al. 2003).

$$H2O_m \text{ (melt)} + O \text{ (melt)} <--> 2OH \text{ (melt)} \quad (1.5)$$

The equilibrium equation used is

$$\eta_{Tae} = \eta_{Tg} = 10^{11.45}/q \quad (1.6)$$

where $\eta_{Tae}$ is the viscosity at the equilibrium temperature, $\eta_{Tg}$ is the viscosity at the glass transition temperature, q is the cooling rate ($Ks^{-1}$), and the unit of the constant $10^{11.45}$ is PaK, which has an estimated uncertainty of +/- 0.2 log units.

Expanded non-Arrhenian, composition dependent models were presented by Giordano et al. (2006), Hui and Zhang (2007), and Giordano et al. (2008). Giordano et al. (2006) performed regressions on 800 experimental data on 44 anhydrous samples over a viscosity range of $10^{-1}$ to $10^{12}$ Pas at temperatures ranging from 700 to 1650 °C. Hui and Zhang (2007) developed a 37 parameter model based on 1451 data points taken from the literature, to be used within a viscosity range from 0.1 to $10^{15}$ Pas, and a temperature range from 573 to 1978 K. Giordano et al. (2008) presented a 17 parameter TVF model based on more than 1770 data points, spanning a viscosity range between $10^{-1}$ and $10^{14}$ Pas. This study relates viscosity to the major oxides found in silicate glasses in addition

to temperature and water content. All three of these models are empirically based on measurements taken from samples sweeping the spectrum of silica concentrations.

One goal of this study is to test these models for rhyolites at low water contents (0.1 to 1 wt.%). This is necessary due to the fact that little viscosity data presently exists at these water contents, at which melts are water saturated at near-surface P-T conditions (e.g. for magma rising out of the conduit). Data collected in this study will fill an important gap in the present data pool, allowing for testing of present models at these water contents.

### 1.4 Thermal Diffusivity

Thermal transport properties play a key role in generation, transport, and crystallization of magma in all tectonic settings. Cooling rate controls the rate of change in viscosity, which is strongly tied to the temperature of the melt, profoundly influencing convection rates of magma bodies as well as the flow distances of lava fields. For intrusive settings, metamorphic timescales of country rock depend strongly on the rate of heat exchange between an intruding magma and its surroundings. Constraining the effects of temperature, water content, and crystals on the thermal conductivity of rock is fundamental to understanding magmatic processes. Conductivity is strongly related to thermal diffusivity:

$$k = D\rho Cp \qquad (1.7)$$

where k is conductivity, D is thermal diffusivity, ρ is density, and Cp is heat capacity.

Until very recently, most thermal diffusivity measurements were made via physical contact of samples with a heat source (e.g., Osako et al. 2004; Hofer and

Schilling 2002). Due to inevitable imperfect contact between sample and heat source, contact methods tend to yield a thermal diffusivity value that is systematically lower than the actual value at low temperatures. In addition, contact measurements on the thin, transparent samples allow significant radiative heat to pass through the sample unabsorbed. Radiative transfer results in a systematic overestimation of D at high temperatures (Lee and Kingerly 1960).

Recently, laser flash analysis (LFA) has emerged as the preferred method of measuring thermal diffusivity. The use of a graphite coating on the sample (Degiovanni et al. 1994) and mathematical models of raw data (Mehling et al. 1998) permit complete removal of direct radiative transfer effects at geologically relevant temperatures due to the fact that there is no contact with the sample. This allows for the isolation of the lattice (phonon) component of thermal diffusivity (Pertermann et al. 2007), yielding measurements with small (+/- 2%) experimental uncertainties (Branlund and Hofmeister 2007).

Recent thermal diffusivity data on felsic minerals and glasses indicate a sharp decrease in D as temperature increases up to 400°C, at which point values begin to level off. Branlund and Hofmeister (2007) observed a six-fold decrease in D for quartz crystals between room temperature and 400°C, while data on orthoclase glasses show a thermal diffusivity decrease of 15% within this range. While the change of thermal diffusivity in crystalline materials can be dramatic, the thermal diffusivity of glasses tends to change relatively little, decreasing about 20% between room temperature and the glass transition, after which thermal diffusivity rapidly drops another 20% (Pertermann

et al., 2008). Of the three phases, the melt has the lowest thermal diffusivity, which stays relatively constant as temperature increases further.

Like temperature, water also tends to lower the thermal diffusivity of geomaterials. Hofmeister et al. (2006) implicates protonation as the cause of this, citing that the degree to which thermal diffusivity is lowered is correlated with H content, and the fact that H is the only impurity of significance in fused silica.

### 1.5 Crystals

The presence of crystals in a melt is known to increase both the viscosity and thermal diffusivity. The effect of crystals on viscosity was first modeled by Einstein (1906, 1911) assuming a small concentration of incompressible spheres in suspension. Roscoe (1952) modified Einstein's equation using a model proposed by Vand (1948), which takes into account the volume of suspension unable to flow due to entrapment between spheres of close proximity. Spera (2000) used this model to modify the Einstein-Roscoe equation, making it more useful when evaluating fluids suspending closely-packed particles. The Einstein-Roscoe equation calculates the increase in viscosity of a material due to increasing crystal volume fraction:

$$\eta = \eta_o (1-R\phi)^{-2.5} \qquad (1.8)$$

where $\eta_o$ is the viscosity of the suspension, $\eta$ is the viscosity of the liquid, $\phi$ is the crystal volume fraction, and R = 1.67 (Marsh, 1981).

Stephenson et al. (1996) used parallel plate viscometry data to evaluate the effectiveness of Eq. 1.1 for different microlite textures in the vol. % range of 0-40% and viscosity range of $10^8$ and $10^{11}$ Pas. They found that, for rod or chain-like microlites

below 5 vol.%, the effect on viscosity is negligible. However, when the microlites form branches or take a spider web appearance, such small volume fractions tend to have a much larger effect on viscosity due to the connectivity of the crystals (Stephenson et al. 1996).

The most recent formulation describing the rheology of crystal-rich melts was proposed by Carrichi et al. (2007), based on data from experiments at high temperatures and strain rates relevant to volcanic conduits. This multi-parameter model was designed to consider the non-Newtonian deformation of crystal-rich (50-80%) magmas at different strain rate conditions.

In our study, viscosity data were taken at low strain rates on melts with very low crystal fractions, warranting the use of the straightforward Einstein-Roscoe formulation.

While crystals tend to inhibit a material's ability to flow, they assist in heat transfer. Within a single crystal, thermal diffusivity is highly dependent on lattice orientation. This was demonstrated in Pertermann et al. (2008), which describes laser flash diffusometry on a gem-quality orthoclase crystal with identifiable faces. Samples were cut from the principle faces (001) and (010), as well as the perpendicular orientation (100). This study shows that heat transfers most efficiently through orientation (010), and least efficiently through orientation (100). Compared to crystals, thermal diffusivity of their analogous glass tends to be lower and exhibits weaker temperature dependence, as their disordered structure makes it more difficult to transfer heat via vibrations (Pertermann et al. 2007). Near 800 K, the thermal diffusivity of the glass is roughly equal to that of the most insulating lattice orientation (100) (Figure 1.1) (Pertermann et al. 2008).

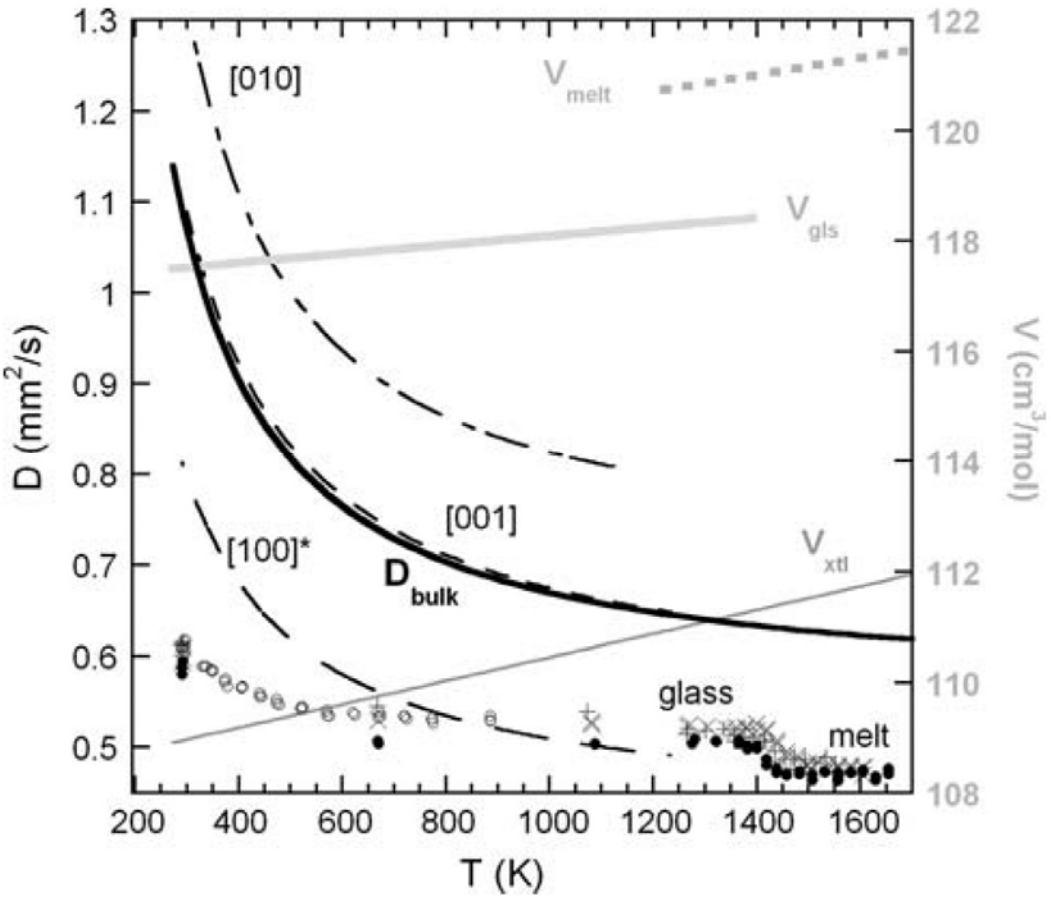


*Figure 1.1. Comparison of thermal diffusivity for orthoclase crystals, glass, and melt. The (010) lattice orientation transfers heat most efficiently, (100) least efficiently. The thermal diffusivity for glass starts relatively low and undergoes a gradual decrease with temperature, intersecting (100) at around 800 K. Figure from Pertermann et al. (2008).*

While there are no models describing the effect of microlites on the thermal diffusivity of silicate glasses, the data shown in Fig. 1.1 suggests that thermal diffusivity will increase with crystal content at a given temperature, with the thermal diffusivity of the crystal-free glass or melt as the lower bound and that of the crystal as the upper bound. Assuming random microlite orientations within the glass (i.e. no flow banding),

the bulk thermal diffusivity of the crystal component can be calculated by averaging the values of the three lattice orientations at a given temperature.

### 1.6 Bubbles

A "bubble" is defined as any void with fluid that is much less viscous than the suspending fluid (Manga and Loewenberg 2001). The relationship of bubble fraction to viscosity is more complex than that of crystals because the presence of bubbles can act to increase or decrease viscosity. Lejeune et al. (1999) measured the viscosity ($10^9$ to $10^{13}$ Pas) of bubble-rich melt at temperatures ranging from 830° to 960°C, at 1 bar pressure. Their data show that low bubble contents (0.06 to 0.13 vol.%) tend to increase the relative viscosity of a melt at temperatures below 850°C. However, at temperatures greater than 850°C, relative viscosity directly decreases, independent of applied stress, with bubble content for all temperatures and bubble volume percentages (Lejeune et al. 1999).

Bubble deformation depends on the relative magnitude of shear stresses that act to deform bubbles compared with the surface tension stresses that act to keep bubbles spherical. The ratio of these two stresses is usually characterized by a dimensionless number called the capillary number:

$$Ca = \text{viscous stresses/surface tension stresses} = (d\gamma/dt)(\eta r/\sigma), \qquad (1.9)$$

where $(d\gamma/dt)$, $\eta$, $r$, and $\sigma$, are the shear rate, suspending fluid viscosity, bubble radius, and surface tension, respectively (e.g. Manga and Loewenberg 2001). Estimates of capillary number in natural lava flows are highly variable, reflecting variations in shear rate and melt viscosity (Manga et al. 1998). At low capillary numbers ($Ca < 0.1$),

bubbles are nearly spherical and relative viscosity increases with porosity (Stein and Spera 2002). For capillary numbers between 0.1 and 10, the emulsions behave as power law fluids (e.g. Taylor 1932) with viscosity dependent on capillary number and porosity (e.g. Rust and Manga 2002). For capillary numbers greater than 10, relative viscosity decreases with porosity, and is independent of capillary number (Stein and Spera 2002). In general, bubbles have a modest effect on the relative viscosity, with viscosity changing by less than a factor of about 3 for volume fractions up to 50% (Manga and Loewenberg 2001).

The effect of bubbles on thermal diffusivity is straightforward, owing to the fact that phonon transfer is much less efficient through gas than through silicate minerals and glasses. During LFA experiments, the onset of bubble growth and vesiculation is marked by a sharp and rapid drop in thermal diffusivity, which suggests that radiative transfer is not very effective.

### 1.7 Mono Craters

Mono Craters is a north-south trending series of rhyolitic flows and domes, associated with the Long Valley Caldera, near Mono Lake in Eastern California. To the south of Mono Craters lies another chain, Inyo Craters. Long Valley Caldera, formed during the large (600 cubic kilometer) Bishop Tuff eruption at ca. 0.76 Ma. Mono Craters began erupting 40 ka, with the most recent eruption occurring around 550 years ago (Bailey, 1989) . The obsidians analyzed in this study come from three vents within the Mono Craters volcanic chain: North Coulee, Northwest Coulee, and South Coulee (Figure 1.2).

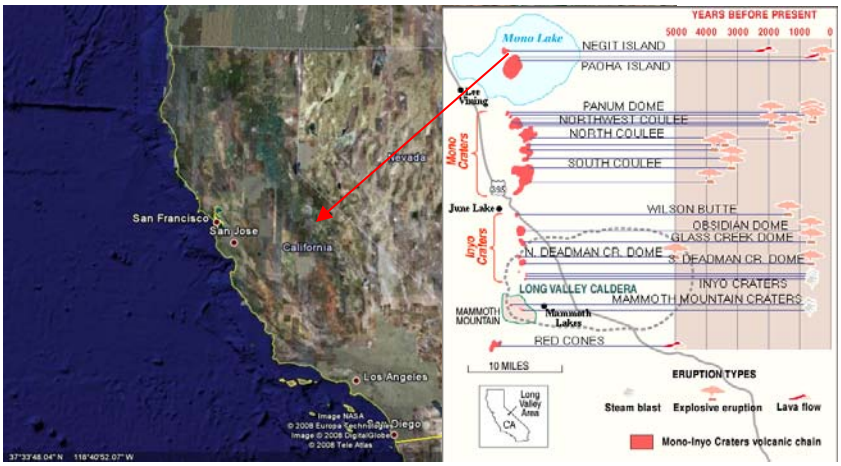


*Figure 1.2. The Long Valley area, located in Eastern California, comprises Long Valley Caldera, the Mono-Inyo volcanic chain, and Mono Lake. Mono Craters have been active and erupting explosively and effusively over the past 4000 years. In this study, we analyze glasses from three vents: North Coulee, Northwest Coulee, and South Coulee. Map from Long Valley Volcano Observatory (lvo.wr.usgs.gov)*

The Mono-Inyo volcanic system as a whole (Figure 1.2) contains both explosive and effusive eruption styles. Both are characterized by slow magma ascent rates (~2 cm/s), comparable to the average effusion rate (~1.6 cm/s) of the dome lavas (Castro et al. 2002), contradicting the view that the explosive eruptions within the Mono-Inyo system are a result of high magma flow rates (Woods and Koyaguchi, 1994). Instead, the explosive eruption dynamics of the Mono-Inyo system are likely driven by rapid exsolution of volatiles within the magma body near the surface. The phreatic eruptions within the Inyo system and at Panum Crater, within the Mono Craters system, are a prime example of this.

While some of the eruptions within the Mono Craters system are rapid and explosive, others are effusive due to the very slow magma ascent and water exsolution rates. The dome formations within the flows analyzed in this study exemplify this. Instead of fragmenting, the lava deforms ductily during dome growth.

The eruptive history of the Long Valley area has proven dramatic over the years, the best-known being the Bishop Tuff eruption. This eruption was one of the largest in the history of North America, releasing 600 cubic kilometers of ash. Significant ash has been found as far away as eastern Kansas and Nebraska (Figure 1.3). Due to the relative

homogeneity of melts in the area (Bailey, 1989), we can apply our understanding of Mono Craters to the entire Long Valley magmatic system. Findings from this study will also be applicable to Yellowstone and other large rhyolitic calderas which have produced the largest eruptions on Earth.

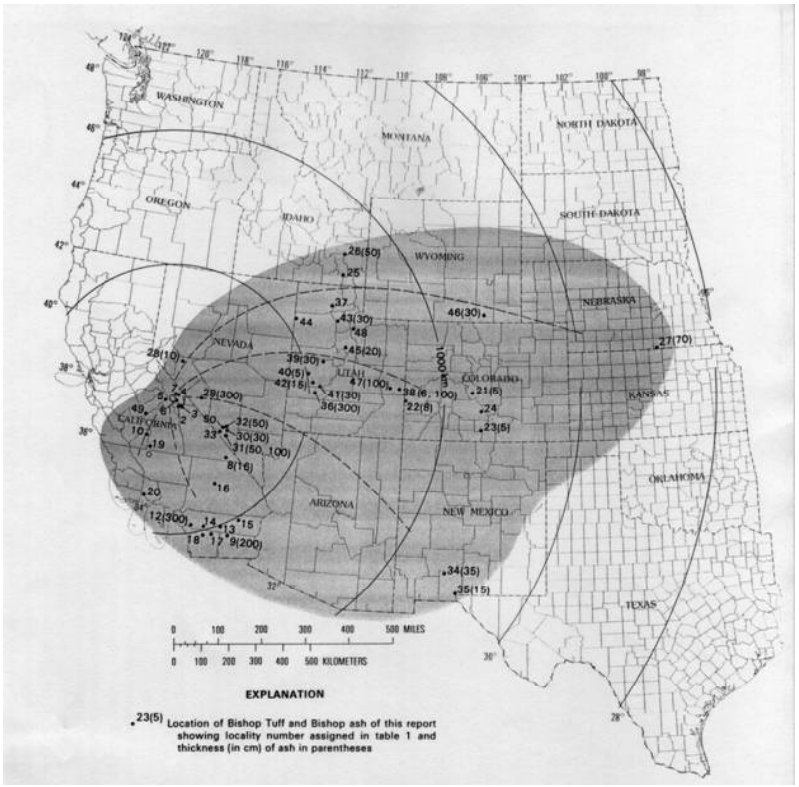


*Figure 1.3. The 0.76 Ma Bishop Tuff eruption deposited 600 km$^3$ of ash as far east as Kansas and Nebraska, covering about a 20% of the continental United States. Map from Izett (1988).*

## 1.8 Summary

- This study aims to constrain the effect of temperature, water content, and crystal fraction on the flow and heat transfer properties of Mono Craters glasses and melts.
- Rhyolitic melts can be modeled as Arrhenian only over narrow viscosity ranges near the glass transition. At large temperature and viscosity ranges, for example

from the glass transition to liquidus temperatures, a non-Arrhenian formulation, such as the TVF equation, is necessary.

- Viscosity decreases with temperature and water content, and increases with crystallinity. The effect of bubbles on viscosity is dependent on capillary number.
- LFA analysis has taken over as the preferred thermal diffusometry method. It eliminates contact losses and radiative transfer, isolating the lattice vibration (phonon) component of heat transfer.
- Thermal diffusivity decreases with water content and porosity, and increases with crystallinity. Due to the random structure of glass, phonon transfer is less efficient through glasses than crystals.
- Mono Craters, the field site, and neighboring Inyo Craters and Long Valley Caldera, have a rich eruptive history and are still active.
- Due to the chemical homogeneity of melts throughout the region, analysis of Mono Craters glasses will help us better understand the entire Long Valley magmatic system.

# Chapter 2—Sample Characterization Methods

## 2.1 Introduction

The glasses used in this study were collected from Mono Craters in the summer of 2007. These were collected from North Coulee (named "MCNC"), Northwest Coulee (named "MCNWC"), and South Coulee (named "MCSC"). In order to constrain the effects of water content and crystallinity on the viscosity and thermal diffusivity of these glasses, it was necessary to measure these quantities. The density of each sample also had to be measured to assist in calculating correct values for water content and viscosity. In this chapter, we outline procedures for sample characterization.

## 2.2 Density measurement

The density of each core was measured using Archimedes' principle and the displacement method, using the Mettler Toledo density determination kit. By comparing the sample's apparent mass in air to that when submerged in distilled water, the density of the sample was calculated using the following equation:

$$\rho = A/(A-B)(\rho_{H2O} - \rho_a) + \rho_a \qquad (2.1)$$

where A is the apparent mass of the sample in air, B is the apparent mass of the sample in distilled water, $\rho_{H2O}$ is the density of distilled water at the temperature of measurement, and $\rho_a$ is the density of air. The apparent mass of each sample, in and out of water, was calculated as the average of three measurements. The density of water at its measured temperature was determined from a temperature-density chart for water, and the density of air was estimated at 0.0012 g/cm$^3$. Repeat measurements show the average precision for density measurements to be better than +/- 0.003 g/cm$^3$.

## 2.3 Analysis of Water Contents via Near-IR Spectroscopy

### *2.3.1 Sample preparation*

Due to the risk of water loss from the melt during viscosity experiments, it was necessary to measure the water content of the sample before and after each experiment. Sample preparation involved cutting a section off the sample, grinding the section to a thickness under 600 microns, and polishing it to a fineness of 5 μm or better. During this process, care had to be taken that the thickness of the section was relatively uniform so section thickness could be measured to an uncertainty under 2%.

### *2.3.2 Spectroscopic analysis*

Sections were analyzed using an evacuated Bomem DA3.02 Fourier transform interferometer with an SiC source, an InSb detector, and a $CaF_2$ beamsplitter. Instrumental accuracy is 0.01 $cm^{-1}$. About 1500 scans were collected at room temperature in a range from ~1200–7000 $cm^{-1}$ at a resolution of 4 $cm^{-1}$. Segments were merged and absorbance ($a$) was calculated from:

$$a = -\log(I_{trans}/I_0) \qquad (2.2)$$

where $I_{trans}$ and $I_0$ are intensities of the sample and reference spectra respectively.

Water content and speciation information was derived from absorbance spectra at wavenumbers, 3570, 4500, and 5200 $cm^{-1}$, which give absorbances due to total water, water as OH-, and water as $H_2O$ respectively (Figure 2.1).

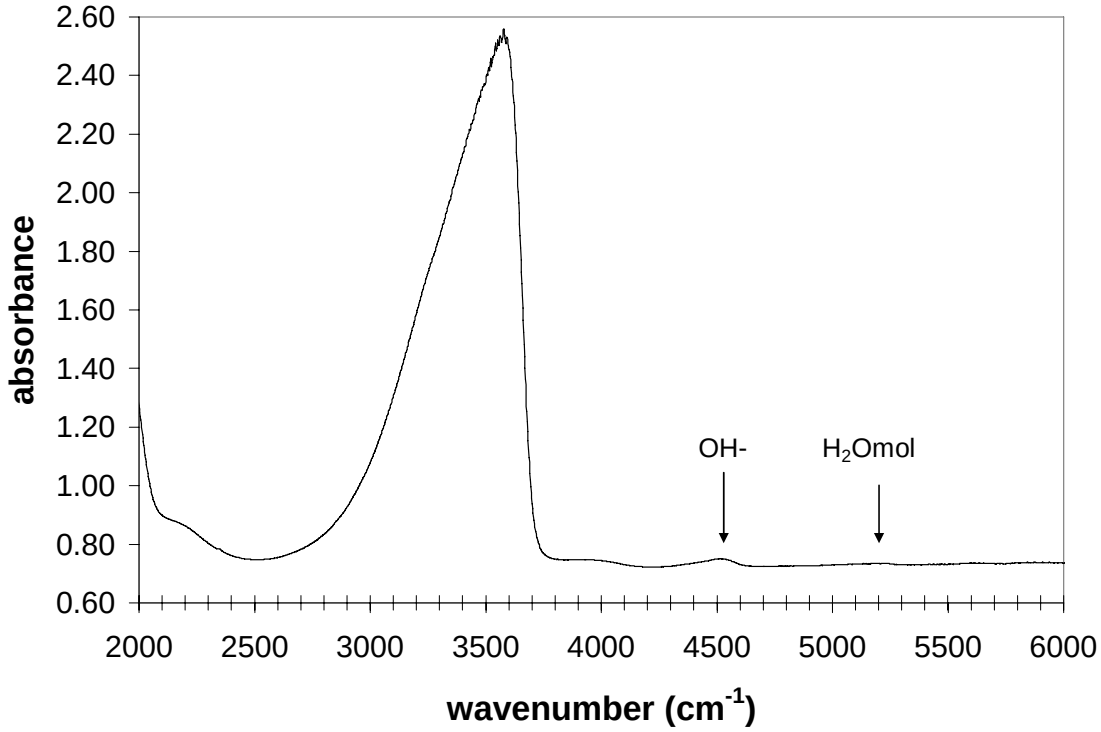


*Figure 2.1. FTIR absorbance spectrum of sample NWCA1B, a rock from Northwest Coulee. The 3500 $cm^{-1}$ peak gives total water, the 4500 $cm^{-1}$ peak gives water as OH-, and the 5200 $cm^{-1}$ peak gives water as molecular $H_2O$.*

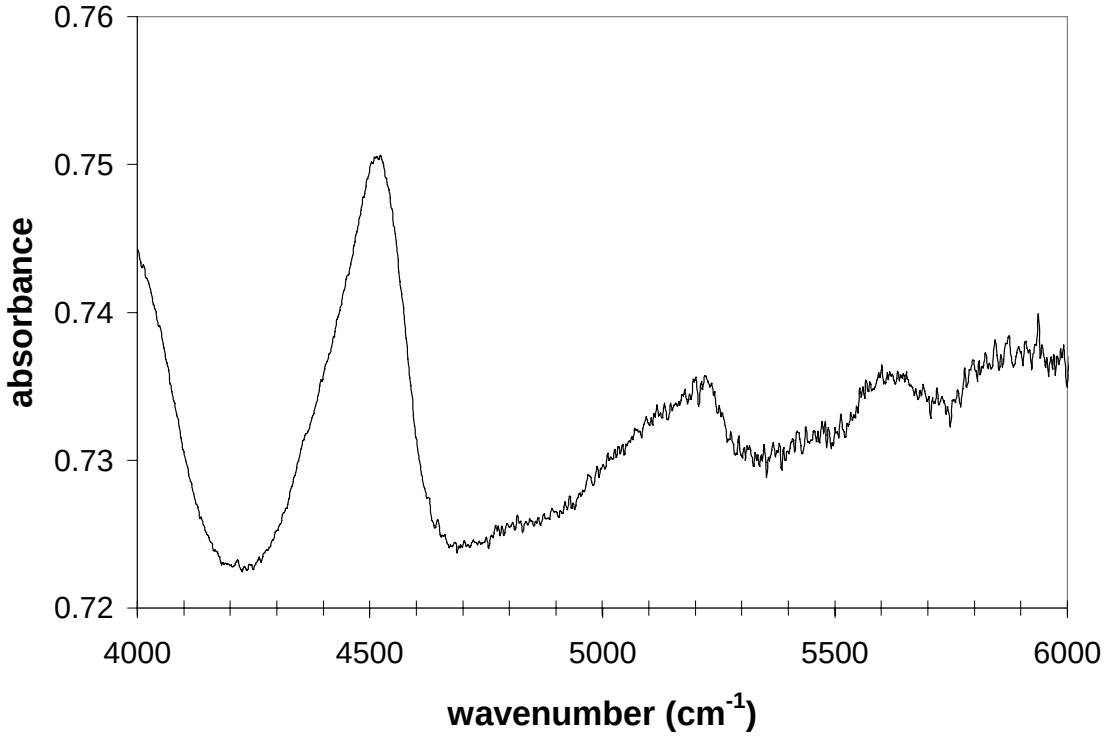


*Figure 2.2. The smaller 4500 $cm^{-1}$ and 5200 $cm^{-1}$ peaks give water as OH- and molecular $H_2O$ respectively.*

Absorbance at a particular band can be converted to weight percent water using the equation:

$$H_2O \text{ wt } \% = 1802\, a/\rho d\varepsilon \qquad (2.3)$$

where $a$ is the absorbance, $\rho$ is sample density in $kg/m^3$, d is sample thickness, and $\varepsilon$ is molar absorptivity, an experimentally-determined calibration constant. The 3570 $cm^{-1}$ band was converted to total water using $\varepsilon = 8$ +/- 1, where section thickness is given in mm (Ihinger et al. 1994). The 4500 and 5200 $cm^{-1}$ bands were converted to water as OH- and water as $H_2O$ using $\varepsilon$ values of 1.73 +/- 0.02 and 1.61+/- 0.05 respectively, and a unit of cm for section thickness (Newman et al. 1986).

## 2.4 Evaluation of Crystal and Bubble Volume Fraction Using Three Methods

As magma becomes more crystalline, its viscosity tends to increase exponentially. In order to find the viscosity of the melt (glass without crystals), viscosity values were corrected based on the crystal volume fraction measured for each obsidian. The effect of bubbles on viscosity is more complex, but the low bubble fractions (as determined from our most porous samples) lead to no significant change in viscosity. Constraining crystal and bubble volume fractions was a three-step process. First, it was necessary to prepare a thin section for each sample. Next, we took a series of micrographs for each thin section. Finally, we analyzed the micrographs using three imaging programs, all of which involve selecting the crystals within the micrograph and finding crystal volume fraction ($\phi$) by dividing the total area of the crystals by the area of the entire micrograph. For randomly distributed crystals, the area fraction is equal to the volume fraction.

### *2.4.1 Preparation of thin sections*

A series of thin sections were prepared from each rock, before and after each parallel plate experiment, with the purpose of visually checking that there were no significant changes in crystallinity or porosity during the experiment. Thin section preparation was a four-step process. First, a rough section needed to be cut from the core used in viscometry, before and after the experiment. Second, the section was polished on one side to a 5 μm fineness and glued to a slide using Crystal Bond epoxy. Third, the section was ground to a thickness of 100-200 μm. Finally, the section was polished with 1 μm alumina powder.

*2.4.2 Micrography*

Two methods were used to image samples in this study. First, a digital camera was used to take photomicrographs in a magnification range between 4x and 20x with plane polarized light and crossed polars. Of these, we found that the plane polar 20x micrographs, covering an area of ~0.25 $mm^2$, offered the clearest rendering of microlite distributions within the glass. These were used for image analysis.

Secondly, 3-D micrographs were taken at 60x with confocal reflection imagery, using an oil immersion lens and a 458 nm laser. An LSM 510 confocal system on a Zeiss Axiovert 200M microscope was used to take 100 micrographs 1 μm apart, from the surface of the section to 100 μm depth. LSM ver. 4.0 SP1 software was used to splice these 2-D micrographs together, creating one 224 x 224 x 100 μm 3-D rendering for each rock in this study, totaling nine. These 3-D images displayed microlite distributions much more clearly than the 2-D light micrographs, and thus were used in the determination of final crystal volume fractions within each rock.

*2.4.3 Image analysis*

Two image analysis programs, Adobe Photoshop ver. 7.0.1 and MetaMorph ver. 6.1, were used to determine the crystal volume fractions suggested by the 2-D renderings, with the purpose of comparing the results given by each. Both programs work on the principle that, due to the difference in the color and hue of the crystals and bubbles from that of their matrix glass, they can be selected from the photograph, allowing the pixels

they comprise to be counted. Results from Adobe Photoshop and MetaMorph were converted to crystal/bubble volume fractions using the equation:

$$\phi = A_{frac} / A_{tot} \qquad (2.4)$$

where $A_{frac}$ is the number of pixels contained in the selected crystals/bubbles, and $A_{tot}$ is the pixel area of the entire micrograph.

The 3-D renderings were analyzed using Imaris ver. 4.5.2 imaging software. As with Adobe Photoshop and MetaMorph, Imaris selects crystals based on their color and hue differences from the matrix glass. Imaris gives crystal selection in units of volume ($\mu m^3$), allowing direct calculation of crystal volume fraction:

$$\phi = V_{frac} / V_{tot} \qquad (2.5)$$

where $V_{frac}$ is the total volume of the crystals, and $V_{tot}$ is the volume of the entire 3-D rendering. Due to the fact that these renderings relied on light reflection as opposed to refraction, the contrast between crystal and matrix glass was sharp, decreasing ambiguity in the crystal selection process.

## 2.5 Analysis of Major Oxides via Electron Microprobe

The final step in the sample characterization process was to find the major element composition of each rock. A JEOL JXA 8200 Superprobe, at Washington University, St. Louis, Missouri, was used to find weight percents of the following oxides: $SiO_2$, $TiO_2$, $Al_2O_3$, $Fe_{total}$, MnO, MgO, CaO, $Na_2O$, $K_2O$, and $P_2O_5$. In doing this, we were able to determine the homogeneity of rocks within and between coulees,

particularly in terms of $SiO_2$. In addition, by comparing rock with remelt, we were able to see which elements were contributing to crystal formation, allowing us to deduce the type of minerals crystallized in each glass. While it is normally easier to do this by looking at the thin section, the small size of the microlites made visual identification difficult.

### 2.6 Summary

- Density was determined using Archimedes' principle. The density value for each glass was used in viscometry and FTIR calculations.
- The 3570, 4500, and 5200 $cm^{-1}$ absorption peaks were used to calculate total water, water as OH-, and molecular water, respectively, within each sample before and after viscometry.
- 2-D light micrographs were used to find crystal and bubble fractions within each sample. Area percents were determined using Adobe Photoshop and MetaMorph, then compared.
- More accurate crystal volume fractions could be obtained from 3-D confocal reflection imagery on bubble-free samples. Crystal volume fractions were determined using Imaris imaging software.
- Electron microprobe analyses were used to determine the major element composition of each obsidian, allowing us to evaluate the homogeneity of Mono Craters glasses and deduce the minerals present by comparing major oxides in the glass to its corresponding crystal-free remelt.

# Chapter 3—Experimental Methods

## 3.1 Introduction

With samples characterized in terms of water content and crystal and bubble fractions, the next step was to collect viscosity and thermal diffusivity data as a function of temperature on both natural and remelted glasses. Viscosity data were collected using parallel plate and concentric cylinder viscometry. Thermal diffusivity data were collected via laser flash analysis (LFA). In LFA, thermal diffusivity is deduced from the time it takes for the energy of a laser pulse to pass through a sample of known thickness. Complete conversion of radiative energy into thermal energy is assumed. This chapter outlines procedures for producing remelted glass as well as the viscometry and diffusometry methods used in this study, including details of sample preparation and data collection.

## 3.2 Remelting

In order to understand the behavior of the magma at Mono Craters under melt conditions, data needed to be collected on remelted rock. Remelt data were used constrain the behavior of water-, crystal-, and bubble-free melt. One rock from Northwest and South Coulees, and two rocks from North Coulee, were fragmented, placed in an alumina crucible, and remelted in a Thermolyne (model 46240) high temperature muffle furnace. Temperatures and durations were set with the following in mind:

i. the remelt needed to be free of water and bubbles.

ii. water needed to exsolve slowly to ensure that the sample did not foam out of the crucible.

iii. the remelt needed to be well-annealed, but free of crystals.

(i) was accomplished by a long duration at a high temperature. The sample was held at a temperature of 1500°C over 7 days, allowing adequate time for water to bubble out of the melt. A slow heating rate was vital for (ii). The sample was heated at 2°C/min from room temperature to 1500°C, with 12-hour dwell times at 900°C and 1200°C respectively. Slow gas exsolution kept the melt from foaming and overflowing the crucible, assuring the safety of the furnace. Slow cooling was essential in achieving a well-annealed remelt, (iii). A 2°C/min cooling rate assured a well-annealed, but crystal-free, product.

## 3.3 Parallel Plate Viscometry

### *3.3.1 Sample preparation*

The core was drilled from the rock or remelt using a 5/16" Starlite diamond core drill bit, producing cylinders approximately 6.6 mm in diameter. A diamond saw was then used to cut the core to a length between 2 and 14 mm. Finally, the ends of the cylinder were ground parallel to each other and polished to a 10 μm fineness. A micrometer was used to measure the sample's length and diameter as well as to ensure the ends of the core were parallel.

### *3.3.2 Data collection*

A Theta Industries Rheotronic III 1000C parallel plate viscometer was used to collect viscosity data in the range $10^8$ to $10^{14}$ Pas (Figure 3.1).

*Figure 3.1. The parallel plate viscometer setup (left). A η-T datum is gathered by placing a cylindrical core (below) under a known stress, and measuring its linear deformation rate at a stable temperature.*

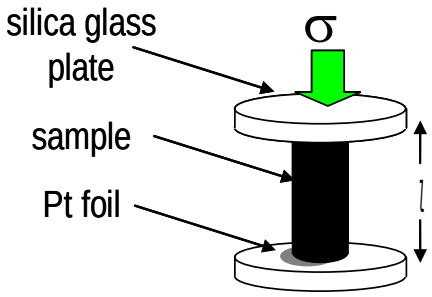


To run an experiment, a core of known dimension was sandwiched between two silica plates; platinum foil was used to improve contact between the plates and the sample. The sample was lowered into a high-temperature furnace, and a 1500g mass was placed above it. A micrometer, built into the machine, measured the length of the sample as it deformed with time. A plot of these measurements is shown in Figure 3.2.

Glass behaves as a visco-elastic material. In other words, it undergoes a gradual transition from elastic to plastic (or viscous) deformation (termed "relaxation") when subjected to a stress. Relaxation time depends on viscosity: ~1s at $10^{10}$ Pas, ~2 min at $10^{12}$ Pas, and ~15 min at $10^{13}$ Pas. This is described by the Maxwell relation:

$$\eta = G\tau, \qquad (3.1)$$

where $\eta$ is viscosity, G is the shear modulus (~ $10^{10}$ Pa) (Dingwell and Webb, 1990), and $\tau$ is relaxation time.

A reliable viscosity measurement takes only the rate of viscous deformation into account.

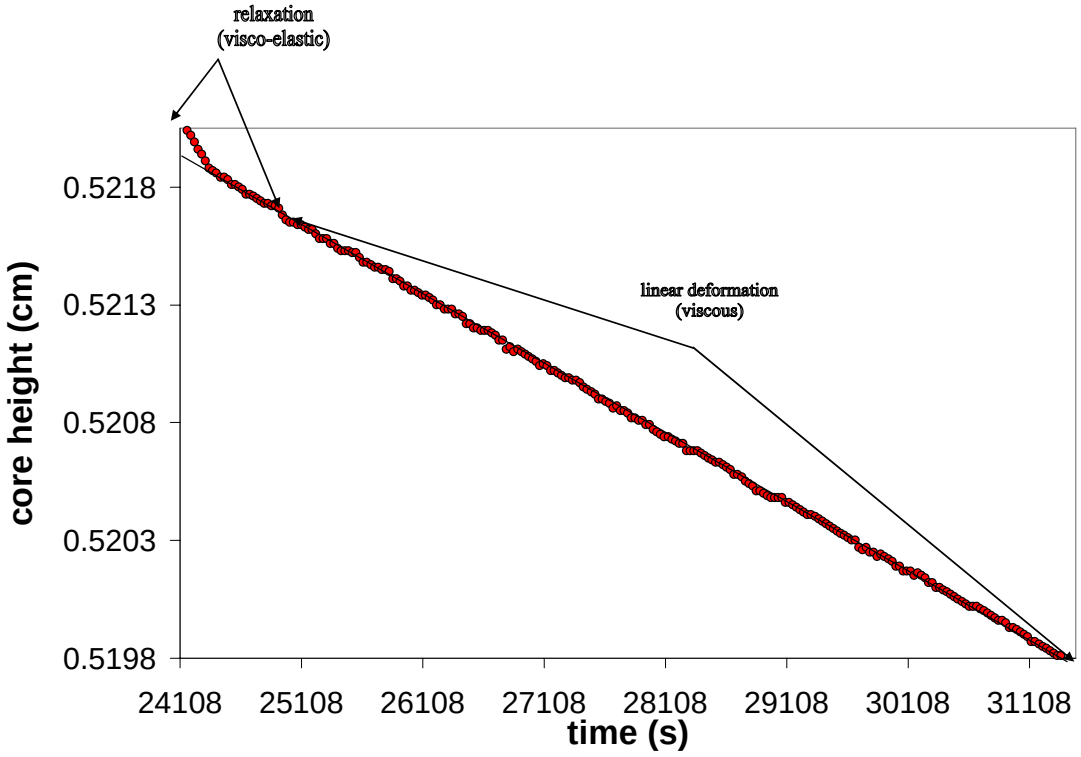


*Figure 3.2. Height-time data. After relaxation, glass behaves as a Newtonian fluid with a linear relationship between stress and strain rate. Viscosity can be calculated from the rate of viscous deformation under a known stress.*

Viscosity (in Pas) is calculated from the slope of the viscous deformation line (dh/dt) using the equation:

$$\eta = mgh^2/(3V(dh/dt)) \qquad (3.2)$$

where m is the mass in kg, g is acceleration due to gravity (9.8 m/s$^2$), h is the height of the cylinder in meters, V is the volume of the sample in m$^3$, and t is time in seconds (Dingwell, 1995). Measurements using the apparatus at MU have experimental

uncertainties less than 0.06 log units based on repeat measurements and agreement with NIST standard glasses (Whittington et al. *in press*).

### 3.4 Concentric Cylinder Viscometry

In concentric cylinder viscometry, superliquidus remelt was stirred at a measured angular velocity at a defined torque, yielding viscosity measurements between $10^4$ and $10^5$ Pas at temperatures between 1400-1500°C. To prepare a remelt for viscometry, at least 55g was crushed and placed inside a 3.3 cm diameter by 6.5 cm tall alumina crucible. It was then melted and viscosity measurements were taken.

Measurements were taken with a Theta Industries Rheotronic II 1600C Rotating Viscometer with a Brookfield HBDV-III measuring head (Figure 3.3). This instrument is based on the Searle design, in which viscous drag of the melt between the rotating spindle and the stationary crucible is measured. Viscous drag, proportional to the viscosity of the melt, is quantified by the torque on the spindle and its angular velocity as it rotates in the melt. When the geometry of the spindle/crucible setup is taken into account, stress and strain rate can be calculated to find viscosity:

$$\sigma = \tau/(2\pi R_b^2 L) \qquad (3.3)$$

$$d\gamma/dt = 2\, R_c^2 \omega/(\, R_c^2 - R_b^2) \qquad (3.4)$$

where $\tau$ is the torque on the spindle (Nm), $\omega$ is angular velocity (rad/s), and L, $R_b$, and $R_c$ are depth of the spindle in the melt, spindle radius, and crucible radius respectively (cm). Data were measured with experimental uncertainties less than 0.06 log units based on repeat measurements and agreement with NIST standard glasses (Getson and Whittington, 2007).

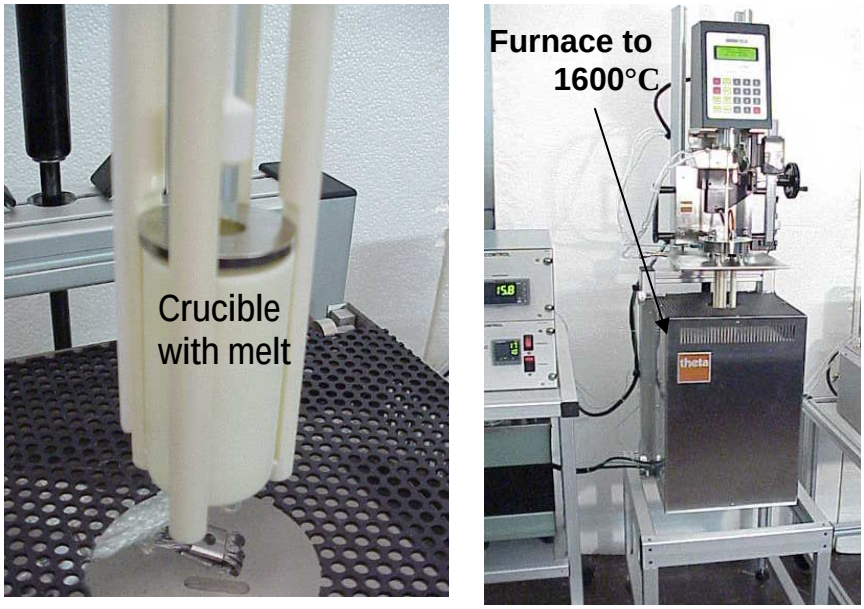


*Figure 3.3. The concentric cylinder viscometer setup. Remelted rock is put into the crucible (top left). The rock is lowered into a furnace (top right), melted and stirred. Viscosity is calculated from the torque on the spindle and its angular velocity as it rotates within the melt (bottom left). For further details, see Getson and Whittington (2007).*

## 3.5. Laser Flash Analysis (LFA)

### *3.5.1 Sample preparation*

A core was drilled from the rock or remelt using a 9/16" Starlite diamond core drill bit, producing cylinders approximately 15 mm in diameter. A diamond saw was

then used to cut a wafer off the cylinder. The wafer was ground to a thickness of ~1mm, with faces parallel. After polishing the wafer to a 10 μm fineness, it was sandblasted, and three coats of graphite spray were applied to each side in order to enhance the absorption of the laser pulse and prevent radiative transfer through the sample. Water and crystal contents for LFA samples were taken as the average of all FTIR and confocal measurements on the corresponding rock, as homogeneity of samples was assumed.

*3.5.2 Data collection*

A Netzsch LFA 427 apparatus was used in this study. A graphite holder was used to suspend the specimen within a vertical furnace, allowing analysis of a circular area of diameter 6-10mm at varying temperatures between 0 and 1000°C, as measured by W-Re thermocouples, one of which was located adjacent to the sample. At temperature intervals of 25°C, a single pulse from a Nd-GGG laser heated the sample from below. As heat diffused through the sample, a temperature-time curve (~$10^2$ – $10^4$ ms) was measured by an InSb detector mounted above it. These T-t curves were converted to thermal diffusivity values using Netzsch software and the algorithm of Mehling et al. (1998), which accounts for surface losses to the surroundings, radiative transfer between the top and bottom graphite coats, and the frequency dependence of absorbance. Thermal diffusivity values acquired in this study represent the average of multiple shots at a given temperature. These measurements have uncertainties of ~2%, calculated by repeat measurements on reference materials (graphite and Fe alloys). The main source of this uncertainty is the deviation in measured sample thickness from actual due to the fact that the sides of the wafer are not perfectly parallel. For further details, see Blumm and Lemarchand (2002), Hofmeister (2006), and Pertermann and Hofmeister (2006).

### 3.6 Summary

- Remelted rock was used to compare viscosity and thermal diffusivity measurements of hydrous, microlite-rich obsidian to its corresponding anhydrous crystal-free matrix glass.

- Parallel plate viscometry is used to measure $\eta$ near the glass transition ($10^8$-$10^{13}$ Pas). Viscosities are calculated from the sample's measured viscous deformation rate under a known stress.

- Concentric cylinder viscometery, which measures viscous drag as a spindle rotates within a melt, is used to measure $\eta$ ($\eta$=$10^4$-$10^5$ Pas) at superliquidus temperatures. Stress and strain rate are calculated from the angular velocity of a rotating spindle within the melt at a given torque.

- In LFA, thermal diffusivity is calculated from the time it takes for the energy of a laser pulse to transfer through a wafer of measured thickness. Thermal diffusivity is calculated from a measured T-t curve using the algorithm of Mehling et al. (1998), which accounts for surface losses, radiative transfer, and the frequency dependence of absorbance.

# Chapter 4—Results

## 4.1 Introduction

Data from sample characterization, viscometry, and LFA experiments are presented here. Glass major oxide compositions, including calculations of melt polymerization for each rock and remelt, come first. Crystallographic analyses follow, including results of microlite volume percent measurements and classification via x-ray diffraction (XRD). Next, results of water content determinations by FTIR are presented, followed by viscosity data from parallel plate and concentric cylinder experiments, along with the TVF equations fit to each data set. Finally, I present and fit thermal diffusivity data collected during the LFA experiments.

## 4.2 Glass Compositions

Electron microprobe analysis was used to find weight percents of the major oxides ($SiO_2$, $TiO_2$, $Al_2O_3$, FeO, MnO, MgO, CaO, $Na_2O$, and $K_2O$) in each rock and remelt used in viscometry and diffusometry experiments (Table 4.1). Oxide weight percents and NBO/T calculations for each rock and remelt are presented in Table 4.1. NBO/T is calculated as the ratio of network modifiers to network formers (Mysen and Richet, 2005):

$$2\ \text{mol\%}(K_2O + Na_2O + CaO + MgO + MnO + FeO + Al_2O_3/\text{mol\%}(SiO_2 + TiO_2 + 2Al_2O_3), \quad (4.1)$$

assuming that all $Fe^{2+}$ acts as a network modifier.

$SiO_2$ and $Al_2O_3$ are the most abundant oxides in these glasses, collectively making up around ninety percent of the entire glass composition, with lesser amounts of $Na_2O$, and $K_2O$. Further, we see a general decrease in $SiO_2$ and an increase in $Al_2O_3$ in the matrix glass when the rock is remelted, suggesting the presence of feldspar polymorphs in the rock. However, we feel that the North Coulee and Northwest Coulee remelts, remelted in alumina crucibles for a 10-day duration, show evidence of alumina contamination with silica removal. These samples show a six percent decrease in silica accompanied by a six percent increase in alumina after remelting. These data are not included in modeling.

Finally, NBO/T calculations, near zero in the rocks and negative (zero) in the remelts, suggest complete polymerization of the glass, which accounts for the high viscosities measured.

Table 4.1. Electron microprobe analyses of remelted glasses and groundmass of unmelted rock samples[a].

| | North Coulée | | | | South Coulée | | | | | Northwest Coulée | | | |
|---|---|---|---|---|---|---|---|---|---|---|---|---|---|
| SAMPLE | NCr remelt | NCA gm | NCC remelt | NCC gm | SCE remelt | SCE gm | SCA gm | NWCE remelt | NWCE gm | NWCA gm | NWCB gm | NWCC gm | NWCF gm |
| n[b] | 8 | 5 | 7 | 10 | 7 | 5 | 5 | 6 | 5 | 5 | 5 | 5 | 5 |
| $SiO_2$ | 73.58 | 78.07 | 71.34 | 77.95 | 77.24 | 78.28 | 77.33 | 72.08 | 77.94 | 77.63 | 78.02 | 77.97 | 77.40 |
| $TiO_2$ | 0.08 | 0.03 | 0.06 | 0.07 | 0.06 | 0.05 | 0.05 | 0.08 | 0.07 | 0.06 | 0.06 | 0.06 | 0.07 |
| $Al_2O_3$ | 15.67 | 12.92 | 19.22 | 12.95 | 14.68 | 12.81 | 12.65 | 18.74 | 12.74 | 12.67 | 12.77 | 12.78 | 12.61 |
| FeO | 0.71 | 0.97 | 1.05 | 1.00 | 1.03 | 0.82 | 0.97 | 1.08 | 0.92 | 0.99 | 0.97 | 0.94 | 0.99 |
| MnO | 0.00 | 0.05 | 0.06 | 0.04 | 0.03 | 0.04 | 0.04 | 0.05 | 0.03 | 0.05 | 0.05 | 0.03 | 0.04 |
| MgO | 0.14 | 0.01 | 0.02 | 0.01 | 0.02 | 0.00 | 0.01 | 0.02 | 0.01 | 0.02 | 0.00 | 0.01 | 0.02 |
| CaO | 0.48 | 0.50 | 0.73 | 0.56 | 0.53 | 0.51 | 0.55 | 0.74 | 0.50 | 0.55 | 0.50 | 0.53 | 0.54 |
| $Na_2O$ | 2.53 | 3.74 | 3.98 | 3.96 | 3.43 | 3.69 | 3.63 | 3.92 | 3.68 | 3.65 | 3.66 | 3.79 | 3.62 |
| $K_2O$ | 6.58 | 4.88 | 4.72 | 4.94 | 4.52 | 4.89 | 4.78 | 4.68 | 4.86 | 4.81 | 4.88 | 4.72 | 4.77 |
| TOTAL | 99.77 | 101.17 | 101.19 | 101.47 | 101.56 | 101.07 | 100.00 | 101.41 | 100.76 | 100.42 | 100.91 | 100.84 | 100.07 |
| NBO/T[c] | *-0.03* | 0.01 | *-0.06* | 0.02 | *-0.02* | 0.01 | 0.01 | *-0.05* | 0.01 | 0.01 | 0.01 | 0.01 | 0.01 |

[a]Compositions were measured using a JEOL JXA 8200 Superprobe at Washington University; 15keV accelerating voltage and 25nA beam current. 20µm spot size used for NCr and NCC; 10µm spot size for the rest.

[b]Number of analyses used to calculate the average

[c]NBO/T is calculated from 2mol%($K_2O$+$Na_2O$+CaO+MgO+MnO+FeO+$Al_2O_3$)/mol%($SiO_2$+$TiO_2$+2$Al_2O_3$) (Mysen and Richet 2005) assuming all iron is $Fe^{2+}$ and acts as a network modifier. NBO/T cannot be negative; italicized numbers indicate samples are theoretically fully polymerized (NBO/T = 0).

## 4.3 Crystal Volume Fractions and Microlite Compositions

### *4.3.1 Crystal volume analysis*

Small microlite volume fractions were found in the natural glasses. X-ray diffraction analyses indicated the presence of calcium-rich plagioclase and chlorite in small quantities. Presence of very sparse quantities of metal oxide crystals, including magnetite and rutile, was confirmed visually.

Confocal reflection imaging (see Appendix 1 for 3D images of each rock) shows maximum crystal volume percentages of 2%, with the average hovering around 1%. This contrasts sharply with values obtained by Photoshop and MetaMorph, which suggest values up to ten times higher. Table 4.2 shows crystal volume percentages obtained using Photoshop and Metamorph in the analysis of 2D light micrographs (Appendix 2) and Imaris in the analysis of 3D images.

Table 4.2. Image analysis data. Photoshop and Metamorph were used to estimate crystal volume percentages using light micrographs. Calculations using Imaris were based on 3D maps collected by confocal reflection imaging.

| | | **Photoshop** | | | **MetaMorph** | | | **Imaris** | | | | | |
|---|---|---|---|---|---|---|---|---|---|---|---|---|---|
| | | 3871488 pixels | | | 3871488 pixels | | | 5057551 um^3 vol. | | | | | |
| Rock | # | pixels | frac | %Range | pixels | frac | %Range | low val. | low frac | high val | high frac | ***mean(%)*** | ***unc.(%)*** |
| NCA | 1 | 31134 | 0.008042 | **0.7-1.2%** | 152290 | 0.039336 | **3-6%** | 29582 | 0.0058 | 59971 | 0.0119 | 0.89 | 0.42 |
| | 2 | 49406 | 0.012762 | | 213207 | 0.055071 | | | | | | | |
| | 3 | 31182 | 0.008054 | | 136469 | 0.03525 | | | | | | | |
| | 4 | 27451 | 0.007091 | | 136513 | 0.035261 | | | | | | | |
| NCC | 1 | 45607 | 0.01178 | **1.1-1.8%** | 162468 | 0.041965 | **3.3-4.6%** | 67663 | 0.0134 | 89031 | 0.0176 | 1.55 | 0.30 |
| | 2 | 66242 | 0.01711 | | 130381 | 0.033677 | | | | | | | |
| | 4 | 70329 | 0.018166 | | 178323 | 0.046061 | | | | | | | |
| NWCA | 1 | 11171 | 0.002885 | **0.2-1.2%** | 75944 | 0.019616 | **0.8-2.3%** | 6987 | 0.0014 | 8684 | 0.0017 | 0.15 | 0.02 |
| | 2 | 50075 | 0.012934 | | 89523 | 0.023124 | | | | | | | |
| | 3 | | | | 33046 | 0.008536 | | | | | | | |
| | 4 | 44495 | 0.011493 | | 67972 | 0.017557 | | | | | | | |
| NWCB | 1 | 725477 | 0.18739 | **5-18%** | 223824 | 0.057813 | **7-11%** | 3403 | 0.0007 | 4721 | 0.0009 | 0.08 | 0.02 |
| | 2 | 261659 | 0.067586 | | 263652 | 0.068101 | | | | | | | |
| | 3 | 238402 | 0.061579 | | 428436 | 0.110664 | | | | | | | |
| | 4 | 176678 | 0.045636 | | 324462 | 0.083808 | | | | | | | |

Table 4.2 (cont.).

| | | Photoshop | | | MetaMorph | | | Imaris | | | | | |
|---|---|---|---|---|---|---|---|---|---|---|---|---|---|
| | | 3871488 pixels | | | 3871488 pixels | | | 5057551 um^3 vol. | | | | | |
| Rock | # | pixels | frac | | pixels | frac | | low val. | low frac | high val. | high frac | **mean(%)** | **unc.(%)** |
| NWCC | 1 | 79253 | 0.020471 | **1.2-2.1%** | 239385 | 0.061833 | **2-6%** | 65089 | 0.0129 | 75120 | 0.0149 | 1.39 | 0.14 |
| | 3 | 53324 | 0.018638 | | 99198 | 0.025623 | | | | | | | |
| NWCE | 1 | 85960 | 0.022203 | **2-5%** | 358341 | 0.092559 | **9-16%** | 35688 | 0.0071 | 42771 | 0.0085 | 0.78 | 0.10 |
| | 2 | 22408 | 0.014341 | | 440277 | 0.113723 | | | | | | | |
| | 3 | 146441 | 0.037826 | | 601023 | 0.155243 | | | | | | | |
| | 4 | 198375 | 0.05124 | | 358173 | 0.092516 | | | | | | | |
| NWCF | 1 | 99851 | 0.025791 | **2-6%** | 259118 | 0.06693 | **3-14%** | 32012 | 0.0063 | 38540 | 0.0076 | 0.70 | 0.09 |
| | 2 | 232955 | 0.060172 | | 533368 | 0.137768 | | | | | | | |
| | 3 | 80508 | 0.020795 | | 174964 | 0.045193 | | | | | | | |
| | 4 | 68481 | 0.017689 | | 152702 | 0.039443 | | | | | | | |
| SCA | 1 | 393224 | 0.101569 | **5-10%** | 199148 | 0.05144 | **5-7%** | 33299 | 0.0066 | 40434 | 0.0080 | 0.73 | 0.10 |
| | 2 | 326687 | 0.084383 | | 242832 | 0.062723 | | | | | | | |
| | 3 | 76245 | 0.05354 | | 284695 | 0.073536 | | | | | | | |
| | 4 | 346529 | 0.089508 | | 214869 | 0.0555 | | | | | | | |
| SCE | 1 | 127276 | 0.032875 | **3-10%** | 336183 | 0.086836 | **8-14%** | 94193 | 0.0186 | 102472 | 0.0203 | 1.94 | 0.12 |
| | 2 | 348818 | 0.090099 | | 442924 | 0.114407 | | | | | | | |
| | 3 | 403243 | 0.104157 | | 542670 | 0.140171 | | | | | | | |
| | 4 | 193125 | 0.049884 | | 315464 | 0.081484 | | | | | | | |

The 3D images are accepted as the most accurate estimation of crystal percent. Of the two 2D analysis programs, Photoshop provides values closer to the true crystal percent than MetaMorph, although both yield high estimations due to the difficulty in selecting only crystals at the surface of the thin section while neglecting those just under the surface (Figure 4.1). In these glasses, microlites average around 1 micron in width. However, in glasses where crystal size is greater than the thin section thickness, 2D analysis would likely yield accurate crystal volume percentages.

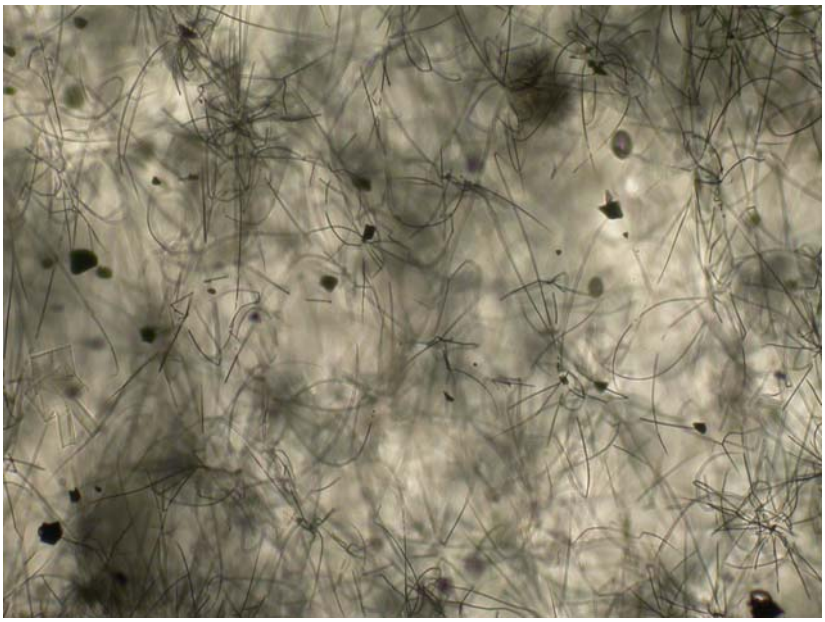

*Figure 4.1. Micrograph NCC#1 (2.5 x 2.5 mm). Microlite widths average around 1 micron, making it difficult to select only those at the surface of the section, a necessary assumption for turning a surface area percent into a volume percent. Hence, 2D analysis tends to yield higher crystal percent values than 3D analysis. For the 2D micrographs used in these analyses, see Appendix 2.*

*4.3.2 Crystal volume percent and viscosity*

We explored the use of two models in correcting the obsidian (melt + crystals) viscosities to those of matrix melt alone, the Einstein-Roscoe relationship proposed by

Marsh (1981), and a model proposed by Carrichi et al. (2007), based on data from experiments covering a high range of strain rates and crystal fractions. This multi-parameter model is designed to consider the non-Newtonian deformation of crystal-rich (50-80%) magmas at different strain rate conditions (relevant to magma in volcanic conduits). As Figure 4.2 shows, the two models are very similar at strain rates and crystal percentages relevant to our parallel plate experiments, well within the experimental error of plus or minus 0.06 log units.

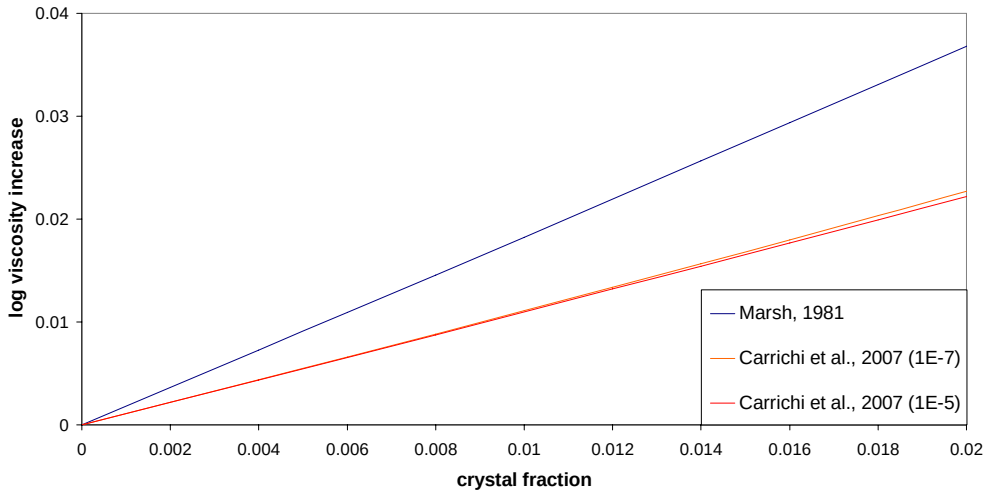


*Figure 4.2. Log viscosity increase vs. crystal fraction curves predicted by the Einstein-Roscoe relationship (Marsh, 1981) and Carrichi (2007) with upper and lower bounds of $10^{-5}$ $s^{-1}$ and $10^{-7}$ $s^{-1}$ respectively for strain rate.*

While the model of Carrichi et al. (2007) is based on more recent data than that of Marsh (1981), their similarity at volume fractions below 2% warrants use of the simpler model. The correction, in any case, is very small.

## 4.4 Water Concentrations and Speciation

The obsidians analyzed in this study exhibit water contents ranging from 0.1 to 1.1 wt.%, while remelts contain between 0.01 and 0.07 wt.%. Water content and speciation data is displayed in Table 4.3. Weight percents of total $H_2O$, water as OH-, and water as molecular $H_2O$ were found by observing the 3600, 4500, and 5200 $cm^{-1}$ absorption peaks respectively, with an experimental error of approximately 10%, of which uncertainties in section thickness measurements and flexicurve baseline fitting were the primary contributors.

Figure 4.3 outlines water speciation in each sample. Water is found exclusively as OH- up to 0.1 wt.%, after which water begins to be incorporated as molecular $H_2O$. Both species increase up to 1 wt.%, at which point OH- begins to level off; above ~2 wt.%, all additional water is incorporated as molecular $H_2O$ (e.g. Stolper, 1982).

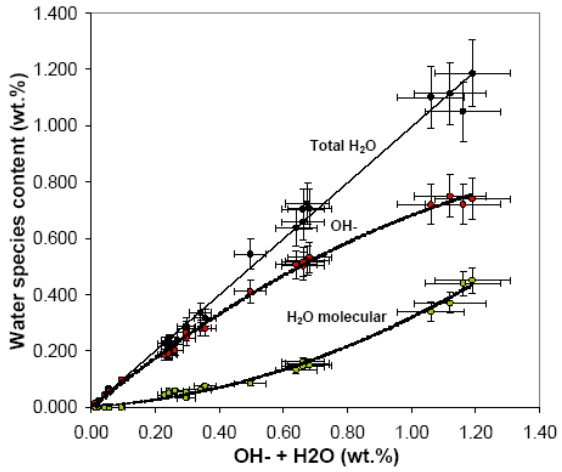


*Figure 4.3. Plot of total water (derived from the 3570 $cm^{-1}$ peak) vs. speciation as an average of before and after measurements. Water exists exclusively as OH- up to 0.1 wt.%. Above 1 wt.%, OH- begins to level off, and further water is incorporated as mostly molecular $H_2O$.*

During parallel plate viscometry on hydrous samples, the possibility of water loss by diffusion was a significant concern. In samples above 0.5 wt.%, water loss was minimized by short experimental durations at cooler temperatures, where exsolution kinetics are slow. The biggest water loss in the reported data occurred in MCNWCF2, which lost 0.1 wt.% during the experiment, dropping from 0.708 to 0.608 wt.%. Water contents used in modeling (Table 4.4) were calculated by averaging measurements before and after viscometry. Water contents before and after viscometry are shown in Figure 4.4 and Tables 4.3a and 4.3b respectively. Sample characterization data, including density, water content and speciation as the average of measurements before and after viscometry, and crystal volume percents, are summarized in Table 4.4.

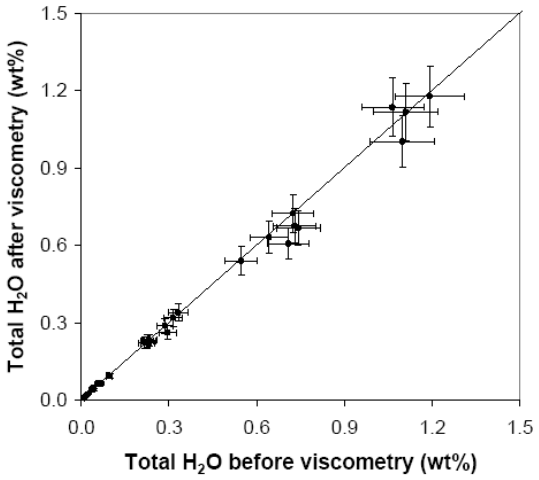


*Figure 4.4. Plot of total water contents before and after viscometry. Water exsolution by diffusion was a significant concern for hydrous samples during parallel plate experiments.*

Table 4.3a: FTIR water content and density measurements for each sample before parallel plate viscometry.

| Sample | thickness µm | density g/cm3 | 3600 cm-1 total wt.% | 4500 cm-1 OH- wt% | 5200 cm-1 H2O Molec. wt% |
|---|---|---|---|---|---|
| MCSCA11 | 239 | 2.311 | 1.193 | 0.75 | 0.46 |
| MCSCA21 | 215 | 2.321 | 1.109 | 0.733 | 0.34 |
| MCSCA22 | 214 | 2.315 | 1.065 | 0.603 | 0.30 |
| MCSCD2 | 250 | 2.317 | 1.099 | 0.77 | 0.52 |
| MCSCE1 | 212 | 2.330 | 0.097 | 0.10 | 0.00 |
| MCSCE5 | 243 | 2.324 | 0.094 | 0.09 | 0.00 |
| MCSCEr1(b) | 234 | 2.320 | 0.066 | 0.06 | 0.00 |
| MCSCEr2(b) | 353 | 2.302 | 0.068 | 0.05 | 0.00 |
| MCSCEr1 | 214 | 2.316 | 0.040 | 0.05 | 0.00 |
| MCSCEr2 | 332 | 2.322 | 0.037 | 0.04 | 0.00 |
| ASCEr | 362 | 2.338 | 0.024 | 0.02 | 0.00 |
| MCNWCA1 | 240 | 2.327 | 0.730 | 0.52 | 0.16 |
| MCNWCA2 | 274 | 2.329 | 0.724 | 0.52 | 0.15 |
| MCNWCB1 | 240 | 2.336 | 0.742 | 0.56 | 0.16 |
| MCNWCC22 | 289 | 2.330 | 0.547 | 0.40 | 0.08 |
| MCNWCE5 | 408 | 2.315 | 0.642 | 0.50 | 0.14 |
| MCNWCF2 | 235 | 2.327 | 0.708 | 0.55 | 0.17 |
| MCNWCEr1(b) | 260 | 2.283 | 0.061 | 0.06 | 0.00 |
| MCNWCEr2(b) | 358 | 2.289 | 0.057 | 0.05 | 0.00 |
| MCNWCEr1 | 432 | 2.323 | 0.037 | 0.04 | 0.00 |
| MCNWCEr2 | 516 | 2.321 | 0.042 | 0.04 | 0.00 |
| ANWCEr | 279 | 2.335 | 0.020 | 0.02 | 0.00 |
| MCNCA22 | 321 | 2.300 | 0.225 | 0.18 | 0.04 |
| MCNCA23 | 239 | 2.308 | 0.232 | 0.20 | 0.04 |
| MCNCA24 | 334 | 2.309 | 0.234 | 0.19 | 0.05 |
| MCNCA25 | 271 | 2.318 | 0.217 | 0.19 | 0.05 |
| MCNCA32 | 346 | 2.230 | 0.226 | 0.20 | 0.06 |
| MCNCC13 | 308 | 2.311 | 0.286 | 0.24 | 0.05 |
| MCNCC15 | 332 | 2.309 | 0.332 | 0.28 | 0.06 |
| MCNCC17 | 504 | 2.340 | 0.295 | 0.28 | 0.03 |
| MCNCC19 | 349 | 2.313 | 0.314 | 0.28 | 0.08 |
| ANCCr1 | 315 | 2.332 | 0.009 | 0.01 | 0.00 |
| ANCCr2 | 357 | 2.337 | 0.010 | 0.01 | 0.00 |
| ANCr | 257 | 2.346 | 0.013 | 0.01 | 0.00 |
| ANCAr1 | 225 | 2.334 | 0.023 | 0.02 | 0.00 |
| ANCAr2 | 229 | 2.332 | 0.024 | 0.02 | 0.00 |
| ANCAr1pcc | 149 | 2.331 | 0.015 | 0.02 | 0.00 |
| ANCAr2pcc | 167 | 2.331 | 0.017 | 0.02 | 0.00 |

Table 4.3b: FTIR water content and density measurements for each sample after parallel plate viscometry.

| Sample | thickness µm | density g/cm3 | 3600 cm-1 total wt.% | 4500 cm-1 OH- wt% | 5200 cm-1 H2O molec. wt% |
|---|---|---|---|---|---|
| MCSCA11 | 258 | 2.297 | 1.179 | 0.73 | 0.44 |
| MCSCA21 | 161 | 2.323 | 1.118 | 0.766 | 0.40 |
| MCSCA22 | 205 | 2.315 | 1.136 | 0.675 | 0.37 |
| MCSCD2 | 215 | 2.278 | 1.003 | 0.66 | 0.36 |
| MCSCE1 | 255 | 2.327 | 0.094 | 0.09 | 0.06 |
| MCSCE5 | 181 | 2.324 | 0.095 | 0.10 | 0.11 |
| MCSCEr1(b) | 456 | 2.320 | 0.064 | 0.05 | 0.02 |
| MCSCEr2(b) | 377 | 2.317 | 0.066 | 0.05 | 0.02 |
| MCSCEr1 | 240 | 2.322 | 0.043 | 0.04 | 0.01 |
| MCSCEr2 | 336 | 2.325 | 0.045 | 0.04 | 0.01 |
| ASCEr | 254 | 2.336 | 0.024 | 0.02 | 0.00 |
| MCNWCA1 | 227 | 2.307 | 0.677 | 0.48 | 0.16 |
| MCNWCA2 | 270 | 2.319 | 0.724 | 0.52 | 0.15 |
| MCNWCB1 | 218 | 2.231 | 0.668 | 0.50 | 0.13 |
| MCNWCC22 | 254 | 2.269 | 0.540 | 0.42 | 0.09 |
| MCNWCE5 | 323 | 2.081 | 0.631 | 0.51 | 0.12 |
| MCNWCF2 | 306 | 2.326 | 0.608 | 0.48 | 0.12 |
| MCNWCEr1(b) | 387 | 2.302 | 0.065 | 0.06 | 0.00 |
| MCNWCEr2(b) | 248 | 2.300 | 0.065 | 0.06 | 0.00 |
| MCNWCEr1 | 514 | 2.325 | 0.046 | 0.04 | 0.00 |
| MCNWCEr2 | 304 | 2.323 | 0.042 | 0.05 | 0.00 |
| ANWCEr | 304 | 2.335 | 0.020 | 0.02 | 0.00 |
| MCNCA22 | 303 | 2.271 | 0.229 | 0.19 | 0.04 |
| MCNCA23 | 234 | 2.290 | 0.231 | 0.20 | 0.05 |
| MCNCA24 | 271 | 2.287 | 0.233 | 0.19 | 0.06 |
| MCNCA25 | 321 | 2.297 | 0.223 | 0.19 | 0.05 |
| MCNCA32 | 298 | 2.251 | 0.223 | 0.20 | 0.06 |
| MCNCC13 | 368 | 2.315 | 0.289 | 0.25 | 0.05 |
| MCNCC15 | 287 | 2.310 | 0.339 | 0.28 | 0.06 |
| MCNCC17 | 494 | 2.325 | 0.262 | 0.25 | 0.03 |
| MCNCC19 | 371 | 2.232 | 0.319 | 0.28 | 0.07 |
| ANCCr1 | 294 | 2.331 | 0.009 | 0.01 | 0.00 |
| ANCCr2 | 290 | 2.334 | 0.010 | 0.01 | 0.00 |
| ANCr | 335 | 2.342 | 0.013 | 0.01 | 0.00 |
| ANCAr1 | 225 | 2.335 | 0.023 | 0.02 | 0.00 |
| ANCAr2 | 229 | 2.332 | 0.024 | 0.02 | 0.00 |
| ANCAr1pcc | 149 | 2.332 | 0.015 | 0.02 | 0.00 |
| ANCAr2pcc | 167 | 2.333 | 0.017 | 0.02 | 0.00 |

Table 4.4. Characterization data used in modeling for each viscometry sample.

| Sample | Density (g/cm3) | Total Water (3600 cm-1) | OH- (4500 cm-1) | H2O molec. (5200 cm-1) | OH- + H2O | crystal vol% |
|---|---|---|---|---|---|---|
| MCSCD2 | 2.322 | 1.051 | 0.72 | 0.44 | 1.16 | 0.7 |
| MCSCA11 | 2.304 | 1.186 | 0.74 | 0.45 | 1.19 | 0.7 |
| MCSCA21 | 2.322 | 1.114 | 0.75 | 0.37 | 1.12 | 0.7 |
| MCSCA22 | 2.315 | 1.101 | 0.72 | 0.34 | 1.06 | 0.7 |
| MCSCE | 2.327 | 0.095 | 0.10 | 0 | 0.10 | 1.9 |
| MCSCEr(b) | 2.315 | 0.066 | 0.06 | 0 | 0.06 | 0 |
| MCSCEr | 2.322 | 0.041 | 0.04 | 0 | 0.04 | 0 |
| ASCEr | 2.337 | 0.024 | 0.02 | 0 | 0.02 | 0 |
| MCNWCA1 | 2.317 | 0.704 | 0.50 | 0.16 | 0.66 | 0.15 |
| MCNWCA2 | 2.324 | 0.724 | 0.52 | 0.15 | 0.68 | 0.15 |
| MCNWCB1 | 2.284 | 0.705 | 0.53 | 0.15 | 0.68 | 0.08 |
| MCNWCC22 | 2.300 | 0.544 | 0.41 | 0.09 | 0.50 | 1.4 |
| MCNWCE5 | 2.198 | 0.637 | 0.51 | 0.13 | 0.64 | 0.8 |
| MCNWCF2 | 2.327 | 0.658 | 0.52 | 0.14 | 0.66 | 0.7 |
| MCNWCEr(b) | 2.294 | 0.062 | 0.06 | 0 | 0.06 | 0 |
| MCNWCEr | 2.323 | 0.042 | 0.04 | 0 | 0.04 | 0 |
| ANWCEr | 2.335 | 0.020 | 0.02 | 0 | 0.02 | 0 |
| MCNCA22 | 2.286 | 0.227 | 0.19 | 0.04 | 0.23 | 0.9 |
| MCNCA23 | 2.299 | 0.232 | 0.20 | 0.05 | 0.24 | 0.9 |
| MCNCA24 | 2.298 | 0.234 | 0.19 | 0.06 | 0.24 | 0.9 |
| MCNCA25 | 2.308 | 0.220 | 0.19 | 0.05 | 0.24 | 0.9 |
| MCNCA32 | 2.241 | 0.225 | 0.20 | 0.06 | 0.26 | 0.9 |
| MCNCC13 | 2.313 | 0.288 | 0.24 | 0.05 | 0.30 | 1.6 |
| MCNCC15 | 2.310 | 0.336 | 0.28 | 0.06 | 0.34 | 1.6 |
| MCNCC17 | 2.333 | 0.279 | 0.26 | 0.03 | 0.30 | 1.6 |
| MCNCC19 | 2.273 | 0.317 | 0.28 | 0.07 | 0.35 | 1.6 |
| ANCCr1 | 2.332 | 0.009 | 0.01 | 0 | 0.01 | 0 |
| ANCCr2 | 2.336 | 0.010 | 0.01 | 0 | 0.01 | 0 |
| ANCr | 2.344 | 0.013 | 0.01 | 0 | 0.01 | 0 |
| ANCAr1 | 2.335 | 0.023 | 0.02 | 0 | 0.02 | 0 |
| ANCAr2 | 2.332 | 0.024 | 0.02 | 0 | 0.02 | 0 |
| ANCAr1pcc | 2.332 | 0.015 | 0.02 | 0 | 0.02 | 0 |
| ANCAr2pcc | 2.332 | 0.017 | 0.02 | 0 | 0.02 | 0 |

### 4.5 Viscosity Data and TVF Modeling

Viscosity data, adjusted for crystallinity via the Einstein-Roscoe equation, are presented in Table 4.6, divided by experiment (parallel plate and concentric cylinder), and coulee. Concentric cylinder data cover a viscosity range of $9 \times 10^3$ to $8 \times 10^4$ Pas at superliquidus temperatures. Parallel plate data encompass viscosity measurements, near the glass transition, in the viscosity range $9 \times 10^8$ to $10^{13}$ Pas. Viscosities in the intermediate range of $10^5$ to $10^8$ Pas, are inaccessible to both concentric cylinder and parallel plate experiments. Thus, viscosities at these temperatures must be interpolated via modeling.

Table 4.5a. Corrected viscosity data for South Coulee remelts (alumina contaminated—not used in modeling).

| SCEr[d] | | SCEr(b)[c] | | ASCEr[e] | | SCEr(cc) | | ASCEr(cc) | |
|---|---|---|---|---|---|---|---|---|---|
| T (K) | log v (Pas) | T (K) | log v (Pas) | T (K) | log v (Pas) | T (K) | log v (Pas) | T (K) | log v (Pas) |
| 1010.4 | 12.80[a] | 1110.4 | 10.46[a] | 1061.0 | 12.58[b] | 1696.2 | 4.48 | 1693.1 | 4.58 |
| 1030.3 | 12.38[a] | 1130.2 | 10.17[a] | 1070.1 | 12.42[a] | 1704.4 | 4.42 | 1703.9 | 4.50 |
| 1050.2 | 11.92[a] | 1150.6 | 9.84[a] | 1080.6 | 12.09[b] | 1719.0 | 4.31 | 1708.2 | 4.47 |
| 1070.4 | 11.49[a] | 1170.7 | 9.54[a] | 1090.2 | 11.98[a] | 1734.0 | 4.20 | 1722.6 | 4.37 |
| 1090.5 | 11.11[a] | 1170.8 | 9.47[b] | 1100.7 | 11.71[b] | 1758.5 | 4.03 | 1733.3 | 4.28 |
| 1111.1 | 10.74[a] | 1190.9 | 9.20[b] | 1109.8 | 11.48[a] | 1773.5 | 3.94 | 1737.2 | 4.26 |
| 1130.2 | 10.40[a] | 1190.9 | 9.27[a] | 1120.6 | 11.33[b] | | | 1751.9 | 4.16 |
| 1149.7 | 10.21[b] | 1199.7 | 9.10[b] | 1130.7 | 11.21[a] | | | 1761.6 | 4.10 |
| 1150.7 | 10.09[a] | 1200.4 | 9.13[a] | 1140.7 | 10.96[b] | | | 1773.6 | 4.00 |
| 1170.1 | 9.92[b] | 1210.6 | 9.01[a] | 1151.1 | 10.83[a] | | | 1773.7 | 4.01 |
| 1170.8 | 9.78[a] | 1210.8 | 8.94[b] | 1160.9 | 10.61[b] | | | | |
| 1190.6 | 9.61[b] | 1220.1 | 8.84[b] | 1170.6 | 10.46[a] | | | | |
| 1191.0 | 9.49[a] | 1220.7 | 8.88[a] | 1181.1 | 10.27[b] | | | | |
| 1197.4 | 9.39[a] | | | 1190.5 | 10.12[a] | | | | |
| 1200.5 | 9.45[b] | | | 1201.0 | 9.95[b] | | | | |
| 1211.0 | 9.32[b] | | | 1211.0 | 9.81[a] | | | | |
| 1211.0 | 9.20[a] | | | 1211.4 | 9.74[b] | | | | |
| 1217.7 | 9.11[a] | | | 1220.9 | 9.62[a] | | | | |
| 1220.9 | 9.17[b] | | | 1221.1 | 9.65[b] | | | | |
| 1241.1 | 8.92[b] | | | 1231.3 | 9.48[b] | | | | |
| | | | | 1240.6 | 9.35[a] | | | | |
| | | | | 1251.1 | 9.21[b] | | | | |

[a]Core 1
[b]Core 2
[c]First (most hydrous) remelt phase on SCE.
[d]Second remelt phase on SCE.
[e]Third (most anhydrous) remelt phase on SCE.

Table 4.5b. Corrected viscosity data for South Coulee obsidian.

| SCD2 | | SCA | | SCE | |
|---|---|---|---|---|---|
| T (K) | log v (Pas) | T (K) | log v (Pas) | T (K) | log v (Pas) |
| 837.4 | 12.06 | 796.0 | 12.80[b] | 1040.2 | 11.62[e] |
| 847.5 | 11.42 | 799.9 | 12.89[c] | 1040.2 | 11.61[d] |
| | | 801.2 | 12.58[a] | 1060.2 | 11.25[e] |
| | | 805.5 | 12.70[c] | 1060.3 | 11.26[d] |
| | | 809.6 | 12.50[c] | 1080.4 | 10.88[e] |
| | | 810.7 | 12.09[a] | 1080.6 | 10.89[d] |
| | | 855.6 | 11.33[a] | 1100.6 | 10.54[d] |
| | | | | 1100.6 | 10.53[e] |
| | | | | 1112.9 | 10.33[e] |
| | | | | 1120.5 | 10.22[d] |
| | | | | 1120.7 | 10.21[e] |
| | | | | 1132.3 | 10.03[d] |
| | | | | 1132.6 | 10.03[e] |
| | | | | 1152.4 | 9.74[e] |

[a]Core 11
[b]Core 21
[c]Core 22
[d]Core 1
[e]Core 5

Table 4.5c. Corrected viscosity data for North Coulee remelt (used in modeling).

| ANCAr | | ANCArpcc[c] | | ANCAr(cc) | |
|---|---|---|---|---|---|
| T(K) | log v (Pas) | T(K) | log v (Pas) | T(K) | log v (Pas) |
| 1039.8 | 12.74[b] | 1060.4 | 12.52[a] | 1694.5 | 4.50 |
| 1050.3 | 12.54[b] | 1070.7 | 12.09[b] | 1714.6 | 4.35 |
| 1069.7 | 12.07[b] | 1130.9 | 11.06[a] | 1723.9 | 4.30 |
| 1090.64 | 11.41[a] | 1150.8 | 10.55[b] | 1746.9 | 4.13 |
| 1110.63 | 11.02[a] | 1151.0 | 10.69[a] | 1753.2 | 4.09 |
| 1130.56 | 10.66[a] | 1170.7 | 10.22[b] | 1774.4 | 3.96 |
| 1130.7 | 10.90[b] | 1170.9 | 10.36[a] | | |
| 1150.84 | 10.31[a] | 1190.9 | 9.89[b] | | |
| 1170.75 | 9.99[a] | 1191.1 | 10.02[a] | | |
| 1170.9 | 10.21[b] | 1201.5 | 9.85[a] | | |
| 1190.76 | 9.68[a] | 1204.6 | 9.79[a] | | |
| 1204.5 | 9.58[b] | 1210.9 | 9.56[b] | | |
| 1205.63 | 9.46[a] | 1225.4 | 9.33[b] | | |
| 1208.47 | 9.42[a] | 1245.9 | 9.10[b] | | |
| 1226.04 | 9.19[a] | | | | |
| 1236.22 | 9.04[a] | | | | |

[a]Core 1

[b]Core 2

[c]"pcc" indicates that cores were run post concentric cylinder viscometry.

Table 4.5d. Corrected viscosity data for North Coulee remelt (alumina contaminated—not used in modeling).

| ANCr | | ANCCr | | ANCr(cc) | | ANCCr(cc) | |
|---|---|---|---|---|---|---|---|
| T(K) | log v (Pas) | T(K) | log v (Pas) | T(K) | log v (Pas) | T(K) | log v (Pas) |
| 1070.2 | 13.00[b] | 1090.2 | 12.29[b] | 1666.6 | 4.55 | 1695.8 | 4.49 |
| 1130.3 | 11.59[b] | 1090.4 | 12.10[a] | 1674.9 | 4.49 | 1710.4 | 4.39 |
| 1130.4 | 11.67[b] | 1110.4 | 11.90[b] | 1681.5 | 4.44 | 1724.9 | 4.28 |
| 1130.6 | 11.69[a] | 1110.5 | 11.71[a] | 1696.1 | 4.32 | 1739.6 | 4.17 |
| 1150.5 | 11.18[b] | 1120.3 | 11.56[a] | 1710.8 | 4.21 | 1744.7 | 4.14 |
| 1150.8 | 11.28[a] | 1130.4 | 11.48[b] | 1725.5 | 4.09 | 1744.9 | 4.14 |
| 1170.4 | 10.81[b] | 1130.4 | 11.32[a] | 1735.3 | 4.03 | 1754.4 | 4.07 |
| 1170.8 | 10.89[a] | 1140.8 | 11.15[a] | 1740.5 | 3.99 | 1764.4 | 4.01 |
| 1170.8 | 10.85[b] | 1150.4 | 11.09[b] | 1774.5 | 3.72 | 1773.5 | 3.94 |
| 1190.7 | 10.42[b] | 1150.5 | 10.95[a] | | | 1783.5 | 3.87 |
| 1190.9 | 10.53[a] | 1160.5 | 10.79[a] | | | | |
| 1210.8 | 10.07[b] | 1170.6 | 10.60[a] | | | | |
| 1211.0 | 10.18[a] | 1170.6 | 10.71[b] | | | | |
| 1219.3 | 9.90[b] | 1180.6 | 10.45[a] | | | | |
| 1231.0 | 9.73[b] | 1190.6 | 10.26[a] | | | | |
| 1231.1 | 9.84[a] | 1190.6 | 10.37[b] | | | | |
| 1239.0 | 9.58[b] | 1200.5 | 10.11[a] | | | | |
| 1240.2 | 9.64[b] | 1210.9 | 10.02[b] | | | | |
| 1258.8 | 9.27[b] | 1211.0 | 9.92[a] | | | | |
| 1260.0 | 9.36[b] | 1220.7 | 9.79[a] | | | | |
| 1261.0 | 9.34[a] | 1240.8 | 9.46[a] | | | | |
| 1278.6 | 8.98[b] | 1240.8 | 9.55[b] | | | | |
| 1280.8 | 9.05[a] | 1251.2 | 9.34[a] | | | | |

[a]Core 1
[b]Core 2

Table 4.5e. Corrected viscosity data for North Coulee (NCC) obsidian.

| NCC13 | | NCC15 | | NCC17 | | NCC19 | |
|---|---|---|---|---|---|---|---|
| T(K) | log v (Pas) | T(K) | log v (Pas) | T(K) | log v (Pas) | T(K) | log v (Pas) |
| 969.9 | 12.26 | 970.0 | 12.35 | 970.0 | 12.27 | 1000.2 | 11.36 |
| 980.2 | 11.96 | 980.1 | 12.08 | 980.2 | 12.00 | 1020.1 | 10.94 |
| 990.1 | 11.68 | 990.2 | 11.81 | 990.1 | 11.76 | 1040.4 | 10.53 |
| 999.9 | 11.43 | 1000.3 | 11.56 | 1000.2 | 11.51 | 1060.5 | 10.17 |
| 1000.3 | 11.43 | 1010.3 | 11.30 | 1010.0 | 11.28 | 1071.8 | 10.00 |
| 1010.4 | 11.19 | 1020.4 | 11.09 | 1020.3 | 11.04 | 1080.7 | 9.83 |
| 1020.3 | 10.95 | 1030.4 | 10.84 | 1030.1 | 10.82 | 1091.5 | 9.69 |
| 1030.2 | 10.72 | 1040.5 | 10.61 | 1040.3 | 10.62 | 1100.7 | 9.51 |
| 1040.5 | 10.51 | 1050.5 | 10.40 | 1050.4 | 10.43 | 1111.3 | 9.36 |
| 1041.1 | 10.41 | 1060.5 | 10.21 | 1060.5 | 10.24 | 1121.2 | 9.20 |
| 1050.4 | 10.31 | 1080.6 | 9.87 | 1080.5 | 9.91 | | |
| 1051.0 | 10.29 | 1090.7 | 9.70 | 1090.6 | 9.73 | | |
| 1060.4 | 10.12 | 1100.6 | 9.53 | 1100.5 | 9.58 | | |
| 1060.9 | 10.15 | 1110.6 | 9.37 | 1110.6 | 9.43 | | |
| 1070.8 | 10.00 | 1120.4 | 9.22 | 1112.9 | 9.41 | | |
| 1080.7 | 9.83 | 1132.9 | 9.07 | 1122.9 | 9.25 | | |
| 1090.6 | 9.67 | 1133.0 | 9.06 | 1132.8 | 9.13 | | |
| 1090.7 | 9.62 | | | 1132.8 | 9.13 | | |
| 1100.4 | 9.52 | | | | | | |
| 1100.9 | 9.46 | | | | | | |
| 1110.3 | 9.35 | | | | | | |
| 1110.5 | 9.32 | | | | | | |
| 1120.3 | 9.18 | | | | | | |
| 1120.4 | 9.18 | | | | | | |

Table 4.5f. Corrected viscosity data for North Coulee (NCA) obsidian.

| NCA22 | | NCA23 | | NCA24 | | NCA25 | | NCA32 | |
|---|---|---|---|---|---|---|---|---|---|
| T(K) | log v (Pas) | T(K) | log v (Pas) | T(K) | log v (Pas) | T(K) | log v (Pas) | T(K) | log v (Pas) |
| 999.6 | 11.64 | 1020.3 | 11.13 | 1000.0 | 11.49 | 1000.0 | 11.63 | 980.2 | 12.32 |
| 1019.8 | 11.21 | 1030.0 | 10.90 | 1019.9 | 11.07 | 1020.1 | 11.19 | 990.2 | 12.03 |
| 1039.9 | 10.80 | 1050.3 | 10.53 | 1040.4 | 10.62 | 1040.4 | 10.78 | 1000.3 | 11.74 |
| 1060.2 | 10.42 | 1070.3 | 10.18 | 1060.4 | 10.28 | 1060.6 | 10.41 | 1010.1 | 11.47 |
| 1073.1 | 10.18 | 1071.0 | 10.16 | 1071.9 | 10.10 | 1072.3 | 10.23 | 1020.1 | 11.25 |
| 1080.1 | 10.08 | 1090.6 | 9.85 | 1080.5 | 9.95 | 1080.6 | 10.08 | 1030.3 | 11.01 |
| 1092.9 | 9.89 | 1090.7 | 9.87 | 1091.7 | 9.79 | 1092.1 | 9.94 | 1040.3 | 10.82 |
| 1100.5 | 9.75 | 1110.5 | 9.56 | 1100.5 | 9.64 | 1101.0 | 9.75 | 1050.4 | 10.62 |
| 1112.7 | 9.57 | 1110.5 | 9.55 | 1111.4 | 9.50 | 1111.8 | 9.63 | 1060.3 | 10.44 |
| 1122.7 | 9.43 | | | 1121.2 | 9.34 | 1121.8 | 9.46 | 1072.7 | 10.24 |
| | | | | | | | | 1080.7 | 10.11 |
| | | | | | | | | 1082.6 | 10.09 |
| | | | | | | | | 1090.5 | 9.95 |
| | | | | | | | | 1092.5 | 9.94 |
| | | | | | | | | 1100.6 | 9.78 |
| | | | | | | | | 1102.4 | 9.78 |
| | | | | | | | | 1110.4 | 9.63 |
| | | | | | | | | 1112.2 | 9.63 |
| | | | | | | | | 1120.6 | 9.48 |
| | | | | | | | | 1122.1 | 9.48 |
| | | | | | | | | 1132.1 | 9.32 |
| | | | | | | | | 1132.1 | 9.32 |

Table 4.5g. Corrected viscosity data for Northwest Coulee remelt (alumina contaminated—not used in modeling).

| NWCEr[d] | | NWCEr(b)[c] | | ANWCr[e] | | NWCEr(cc) | | ANWCEr(cc) | |
|---|---|---|---|---|---|---|---|---|---|
| T(K) | log v (Pas) | T(K) | log v (Pas) | T(K) | log v (Pas) | T(K) | log v (Pas) | T(K) | log v (Pas) |
| 1030.0 | 12.39[b] | 1050.4 | 11.55[a] | 1060.4 | 12.47[a] | 1680.9 | 4.57 | 1675.4 | 4.54 |
| 1050.3 | 12.00[b] | 1050.5 | 11.49[b] | 1080.6 | 12.07[a] | 1695.5 | 4.45 | 1678.8 | 4.51 |
| 1070.3 | 11.58[b] | 1061.6 | 11.34[a] | 1100.5 | 11.68[a] | 1710.2 | 4.36 | 1693.5 | 4.40 |
| 1090.4 | 11.20[b] | 1062.6 | 11.24[b] | 1110.4 | 11.55[b] | 1724.6 | 4.27 | 1704.4 | 4.32 |
| 1110.4 | 10.83[b] | 1070.4 | 11.07[b] | 1120.8 | 11.29[a] | 1739.3 | 4.17 | 1707.9 | 4.29 |
| 1130.5 | 10.48[b] | 1070.5 | 11.15[a] | 1130.2 | 11.15[b] | 1754.0 | 4.07 | 1722.3 | 4.18 |
| 1150.6 | 10.16[b] | 1081.3 | 10.97[a] | 1141.1 | 10.91[a] | 1763.6 | 4.02 | 1734.5 | 4.10 |
| 1170.5 | 9.85[b] | 1082.2 | 10.88[b] | 1150.5 | 10.80[b] | 1774.1 | 3.94 | 1737.2 | 4.08 |
| 1190.6 | 9.55[a] | 1090.5 | 10.70[b] | 1160.9 | 10.55[a] | | | 1751.5 | 3.97 |
| 1190.8 | 9.55[b] | 1090.5 | 10.76[a] | 1170.6 | 10.45[b] | | | 1761.7 | 3.90 |
| 1203.0 | 9.38[a] | 1110.4 | 10.38[b] | 1180.8 | 10.22[a] | | | 1773.5 | 3.81 |
| 1203.2 | 9.37[b] | 1110.6 | 10.41[a] | 1190.5 | 10.13[b] | | | | |
| 1210.7 | 9.27[b] | 1130.4 | 10.09[a] | 1200.9 | 9.90[a] | | | | |
| 1210.7 | 9.27[a] | 1130.4 | 10.04[b] | 1210.9 | 9.69[a] | | | | |
| 1223.0 | 9.10[a] | 1150.7 | 9.78[a] | 1211.2 | 9.81[b] | | | | |
| 1223.5 | 9.10[b] | 1150.9 | 9.73[b] | 1221.2 | 9.60[a] | | | | |
| 1230.9 | 9.00[a] | 1170.7 | 9.44[b] | 1222.1 | 9.62[b] | | | | |
| 1243.1 | 8.84[a] | 1170.9 | 9.48[a] | 1230.9 | 9.43[a] | | | | |
| 1263.0 | 8.61[a] | 1190.8 | 9.17[b] | 1241.9 | 9.35[b] | | | | |
| | | 1190.9 | 9.21[a] | 1250.6 | 9.18[a] | | | | |
| | | 1198.4 | 9.11[a] | | | | | | |
| | | 1200.6 | 9.05[b] | | | | | | |

[a]Core 1
[b]Core 2
[c]First (most hydrous) remelt phase on NWCE.
[d]Second remelt phase on NWCE.
[e]Third (most anhydrous) remelt phase on NWCE.

Table 4.5h. Corrected viscosity data for Northwest Coulee obsidian.

| NWCA | | NWCB1 | | NWCC22 | | NWCE5 | | NWCF2 | |
|---|---|---|---|---|---|---|---|---|---|
| T(K) | log v (Pas) | T(K) | log v (Pas) | T(K) | log v (Pas) | T(K) | log v (Pas) | T(K) | log v (Pas) |
| 919.5 | 11.93[a] | 960.0 | 11.47 | 939.6 | 12.33 | 929.7 | 12.13 | 889.4 | 12.11 |
| 939.8 | 11.13[b] | 972.6 | 11.25 | 959.6 | 11.93 | 943.0 | 11.89 | 909.9 | 11.58 |
| 940.1 | 11.48[a] | 980.1 | 11.06 | 980.0 | 11.45 | 949.7 | 11.72 | 930.5 | 11.01 |
| 949.9 | 11.19[a] | | | | | 962.5 | 11.51 | | |
| 949.9 | 10.88[b] | | | | | 969.9 | 11.32 | | |
| 959.8 | 10.65[b] | | | | | 982.1 | 11.09 | | |
| 975.3 | 10.29[b] | | | | | | | | |

[a]Core 1
[b]Core 2

Data in Tables 4.5 is plotted on an Arrhenian diagram (Figure 4.5); log viscosity (Pas) vs. inverse temperature ($K^{-1}$).

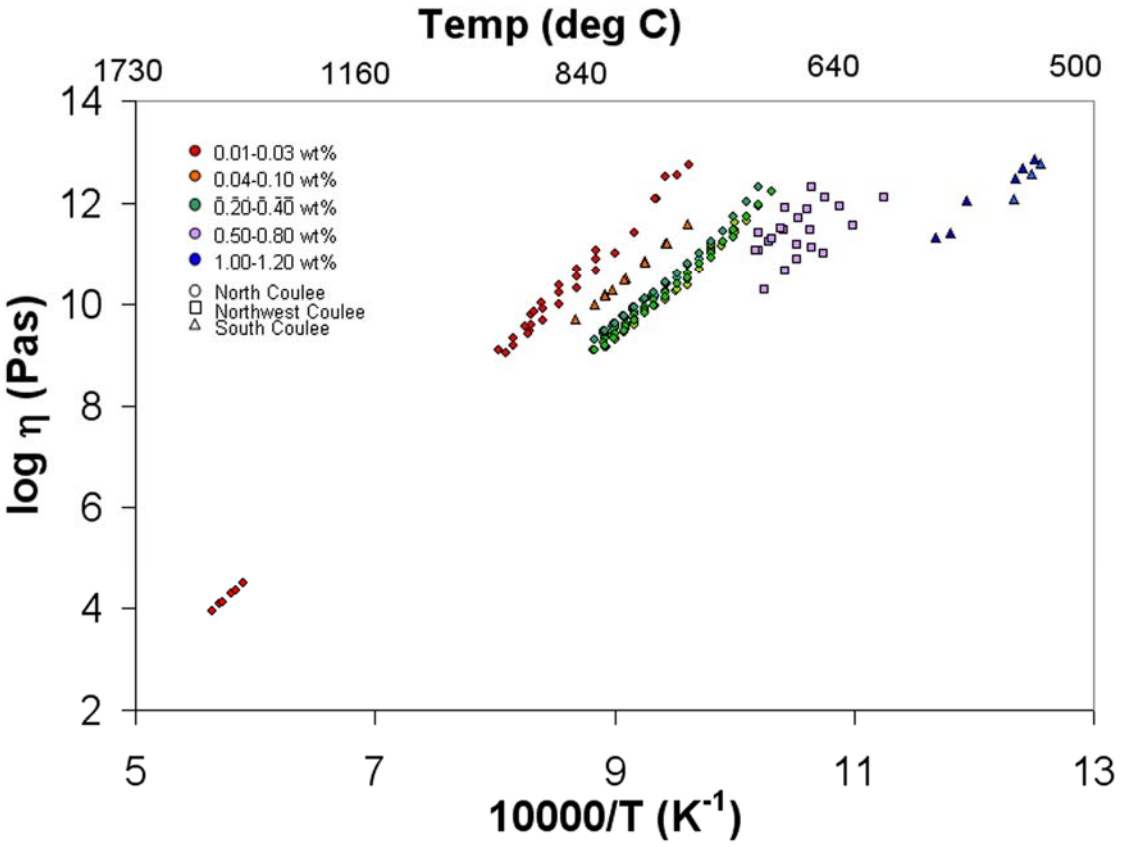


*Figure 4.5. Arrhenian plot of data used in TVF and Adam-Gibbs modeling.*

The remelted glass has a water content around 0.01 wt.%. The obsidians sampled from the field exhibit water contents ranging from 0.1 to 1.1 wt.%. The samples from South Coulee fill the ends of the spectrum, at 0.1 and 1.1 wt.%. The rocks from North Coulee have water contents between 0.2 and 0.35 wt.%. And the rocks from Northwest Coulee have water contents clustered between 0.6 and 0.8 wt.%. As only two rocks from North and South Coulees, and five from Northwest Coulee, were tested, we cannot conclude that there are actual water content differences at these vents.

The data show a trend of decreasing viscosity with water content as expected. The remelt data show an essentially Arrhenian relationship at viscosities between $10^4$ and $10^{13}$ Pas. As water content increases, the slope of the data lessens and appears to become less Arrhenian. The $10^{12}$ glass transition temperatures range from 840 to 550°C within our water content range (Figure 4.6).

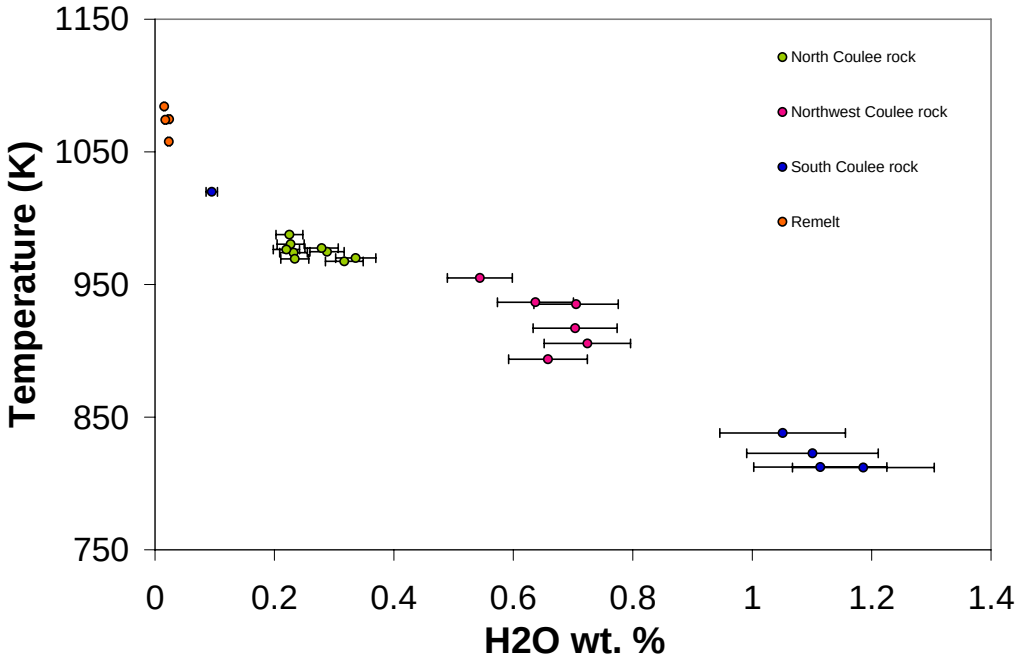


*Figure 4.6. Plot of temperature vs. water content at the $10^{12}$ isokom for each sample.*

## 4.6 LFA Data and Thermal Diffusivity-Temperature Correlations

Thermal diffusivity data (Tables 4.6) were collected on obsidian samples in a temperature range from 20 to 1000°C. Crystal fractions in the samples ranged from 0 to 1.9 vol.%; water contents from and 0.01wt.% 1.1 wt.%.

Table 4.6a. Thermal diffusivity data for the North Coulee obsidian samples.

| **MCNCA** 0.25wt% water | | **MCNCC** 0.28wt% water | |
|---|---|---|---|
| Temp (K) | 0.9% crystals Diffusivity (mm^2/s) | Temp (K) | 1.6% crystals Diffusivity (mm^2/s) |
| 293.8 | 0.641 | 291.6 | 0.625 |
| 327.6 | 0.619 | 292.7 | 0.650 |
| 349.3 | 0.606 | 326.9 | 0.618 |
| 375.5 | 0.595 | 352.7 | 0.605 |
| 408.6 | 0.586 | 378.0 | 0.592 |
| 442.6 | 0.575 | 408.6 | 0.588 |
| 476.1 | 0.565 | 443.1 | 0.582 |
| 526.2 | 0.558 | 477.1 | 0.571 |
| 575.4 | 0.552 | 525.6 | 0.563 |
| 625.3 | 0.551 | 571.6 | 0.549 |
| 674.9 | 0.545 | 576.1 | 0.559 |
| 775.2 | 0.545 | 625.2 | 0.554 |
| 873.0 | 0.546 | 674.8 | 0.551 |
| 974.6 | 0.546 | 724.7 | 0.553 |
| 1077.5 | 0.546 | 774.3 | 0.552 |
| 1115.1 | 0.546 | 823.9 | 0.551 |
| | | 871.1 | 0.546 |
| | | 873.4 | 0.551 |
| | | 921.0 | 0.553 |
| | | 972.1 | 0.557 |
| | | 1022.2 | 0.554 |
| | | 1074.4 | 0.558 |
| | | 1122.3 | 0.562 |
| | | 1152.7 | 0.560 |
| | | 1172.1 | 0.553 |
| | | 1201.6 | 0.548 |
| | | 1230.8 | 0.537 |
| | | 1268.1 | 0.525 |

Table 4.6b. Thermal diffusivity data for the South Coulee obsidian samples.

| **MCSCE** | | **MCSCA** | |
|---|---|---|---|
| 0.1wt% water | 1.9% crystals | 1.1wt% water | 0.73% crystals |
| Temp (K) | Diffusivity (mm^2/s) | Temp (K) | Diffusivity (mm^2/s) |
| 292.9 | 0.678 | 292.6 | 0.684 |
| 326.0 | 0.648 | 292.9 | 0.660 |
| 349.8 | 0.636 | 325.3 | 0.620 |
| 376.6 | 0.625 | 350.9 | 0.607 |
| 425.8 | 0.603 | 375.7 | 0.591 |
| 476.0 | 0.589 | 407.4 | 0.576 |
| 526.1 | 0.581 | 422.0 | 0.584 |
| 575.3 | 0.576 | 441.6 | 0.566 |
| 676.4 | 0.574 | 474.6 | 0.552 |
| 774.4 | 0.568 | 522.7 | 0.546 |
| 873.5 | 0.572 | 575.2 | 0.543 |
| 976.1 | 0.580 | 623.1 | 0.554 |
| 1077.0 | 0.578 | 625.2 | 0.539 |
| 1173.9 | 0.589 | 674.8 | 0.540 |
| 1244.9 | 0.573 | 722.0 | 0.534 |
| 1267.4 | 0.565 | 774.2 | 0.534 |
| 1291.2 | 0.554 | 821.9 | 0.544 |
| 1316.3 | 0.555 | 847.5 | 0.541 |
| 1340.6 | 0.544 | 871.8 | 0.537 |
| 1365.4 | 0.538 | 898.7 | 0.536 |
| 1390.1 | 0.541 | 925.0 | 0.537 |
| 1414.2 | 0.536 | 978.4 | 0.522 |
| 1463.8 | 0.531 | | |

Table 4.6c. Thermal diffusivity data for the remelt and Northwest Coulee sample.

| **ANCr** | | **MCNWCC** | |
|---|---|---|---|
| 0.01wt% water | 0% crystals | 0.55wt% water | 1.4% crystals |
| Temp (K) | Diffusivity (mm^2/s) | Temp (K) | Diffusivity (mm^2/s) |
| 293.2 | 0.626 | 293.4 | 0.665 |
| 337.0 | 0.600 | 325.4 | 0.647 |
| 375.2 | 0.588 | 349.2 | 0.638 |
| 426.9 | 0.563 | 376.5 | 0.625 |
| 476.4 | 0.557 | 425.8 | 0.605 |
| 522.5 | 0.547 | 475.9 | 0.590 |
| 575.4 | 0.546 | 526.1 | 0.583 |
| 676.0 | 0.538 | 575.2 | 0.579 |
| 774.6 | 0.535 | 676.2 | 0.574 |
| 870.8 | 0.534 | 772.2 | 0.572 |
| 976.5 | 0.536 | 873.7 | 0.574 |
| 1078.7 | 0.546 | 977.3 | 0.574 |
| 1176.1 | 0.544 | 1028.4 | 0.575 |
| 1269.1 | 0.546 | 1052.9 | 0.569 |
| 1363.2 | 0.509 | 1077.4 | 0.552 |
| 1370.4 | 0.510 | 1101.8 | 0.500 |
| 1438.1 | 0.522 | | |
| 1462.7 | 0.524 | | |
| 1488.7 | 0.527 | | |
| 1513.1 | 0.534 | | |
| 1538.5 | 0.525 | | |
| 1563.2 | 0.536 | | |

Within Figure 4.7, we can see four segments. Up to ~500°C, D drops with T as the sample becomes phonon saturated. Between ~500°C and ~800°C, the sample, unable to accept further phonon vibrations, has a constant D. At ~800°C, the sample begins to cross the glass transition, which is shown by a drop in D. At ~1100°C, the sample has transitioned to a relaxed melt, at which D is again constant. Our data suggest a slight increase in D above 1100°C. While this may be real, it is more likely due to the sample flowing and thinning.

At temperatures greater than around 500°C, many samples show irregular variations in D, which are ascribed to water loss, foaming, and warping. Samples MCSCA and MCNWCC were visibly altered after LFA, showing foaming resulting from water exsolution from the sample at high temperatures.

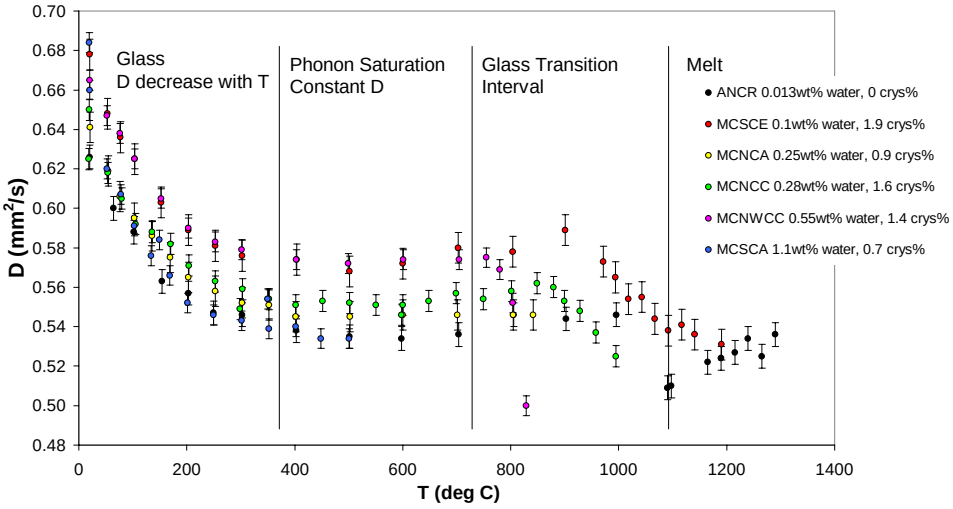


*Figure 4.7. Thermal diffusivity values plotted against temperature. Thermal diffusivity data begin to rise in most samples above 500°C due to warping of the sample, which tends to thin the center of the sample. The glass transition temperature on the time scale of the experiment (T at $\eta \sim 10^8$ Pas) is identified by the sharp drop in thermal diffusivity at temperatures between 800 and 900 °C.*

For discussion and modeling purposes, data collected at or above 780 K are not used. Three general trends can be seen in this data set (Fig. 4.8). First, a general decrease in thermal diffusivity with temperature is observed, with the most rapid decrease taking place between room temperature and 200°C, above which temperature values begin to level off. Second, thermal diffusivity is lower for samples with higher water contents and higher for more crystalline samples. The top three curves belong to samples containing 1.9, 1.4, and 1.6 vol.% crystals respectively, while the bottom two curves contain 0 vol.% crystals and 1.1 wt.% water respectively. The curve for MCNCA is representative of a sample with intermediate crystal and water contents, at 0.9 vol.% and 0.25 wt.% respectively.

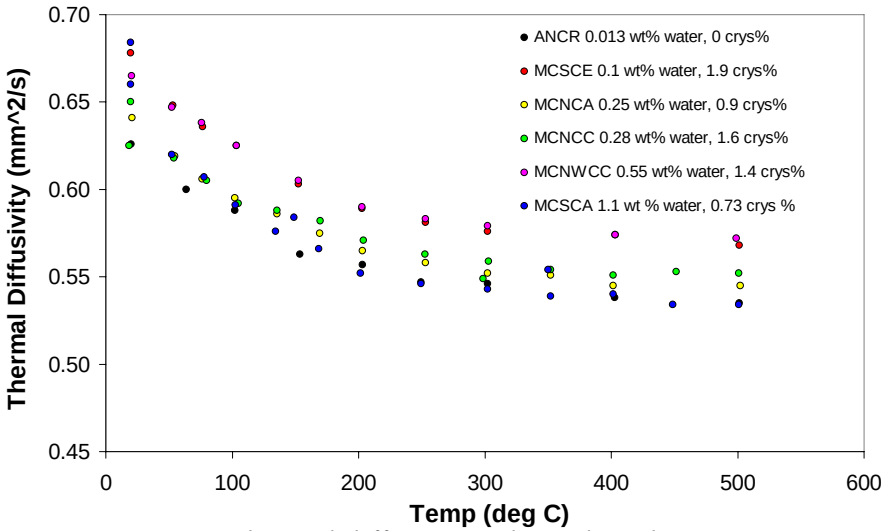


*Figure 4.8. Thermal diffusivity values plotted against temperature. Lower values are displayed by the crystal-free and/or water rich samples, while crystal-rich samples display higher values.*

## 4.7 Summary

- Samples are rhyolitic and thus fully polymerized. Due to alumina contamination, only the ANCA remelt samples were used in modeling.

- Crystals account for less than two percent volume in the glasses used in this study. Water contents lie between 0.1 and 1.2 wt.% in the natural samples and between 0.01 and 0.07 wt.% for remelted samples. Below 0.1 wt.%, water exists exclusively as OH-; above 1 wt.%, additional water exists primarily as molecular $H_2O$.
- Viscosity data show a general decrease in viscosity with temperature and water content.
- Thermal diffusivity data show a rapid decrease in thermal diffusivity with increasing temperature up to 200°C, above which D asymptotically approaches a constant value. Above Tg, D decreases until reaching a constant value for a relaxed melt.

# Chapter 5: Discussion

## 5.1 Introduction

First, viscosity data are compared with data from other studies and other viscosity models, in particular those of Zhang et al. (2003) and Hess and Dingwell (1996), which are specifically for granitic/rhyolitic melts, as well as the global viscosity models of Hui and Zhang (2007) and Giordano et al. (2008). Next, eruption viscosity predictions for Mono Craters and their relation to the observed eruptive styles are discussed. Third, the data are modeled using the empirical TVF equation and the configurational entropy theory-based Adam-Gibbs equation. Finally, we address modeling, and petrological implications of temperature-dependent thermal diffusivity.

## 5.2 Present Viscosity Data

Viscosity data for silicate melts encompassing a range of water contents and temperatures exist in the literature (Figure 5.1). Haplogranite data come from Hess et al. (1995), Schulze et al. (1996), Dingwell et al. (1996), and Dorfman et al. (1996). In addition to nominally anhydrous samples, hydrous samples span water contents between 0.5 and 8.5 wt.%. Temperatures range from 775 to 1916 K. Viscosity data for natural granites and rhyolites come from Shaw (1963), Persikov et al. (1990), Stephenson et al. (1995), Scaillet et al. (1996), Zhang et al. (2003), and Whittington et al. (2004). In addition to nominally anhydrous samples, hydrous samples span water contents between 0.02 and 12.3 wt.%. Temperatures range from 573 to 1473 K. Our data, added with those of Stephenson et al. (1995) and Whittington et al. (2004), fill an important gap in

the existing literature data, spanning a water content range from 0.1 to 1.1 wt.% and temperatures between 800 and 1784 K. This temperature and water content range is important to shallow volcanic processes, and will be beneficial in evaluating the accuracy of present viscosity models under eruption conditions.

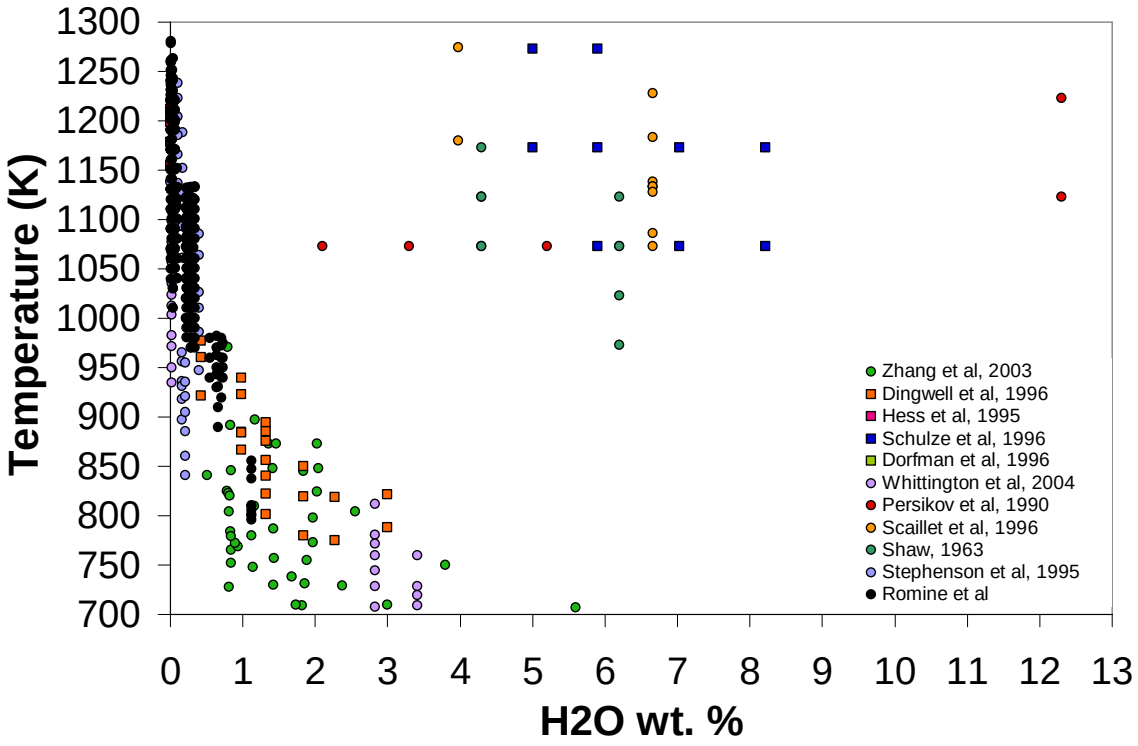


*Figure 5.1. Summary of viscosity data for rhyolitic melts that exist in the literature, as well as data from this study. Data from both natural (circles) and synthetic haplogranite samples (squares), spanning water contents from anhydrous to 12.3 wt.%, are presented. Spanning a range from 0.01 to 1.1 wt.%, an important gap in existing data is filled by this study.*

### 5.3 Models for Rhyolitic Melt Viscosity

We seek to assess how the models of Hess and Dingwell (1996) and Zhang et al. (2003), as well as the global models of Hui and Zhang (2007) and Giordano et al. (2008), fit our data. Few viscosity measurements have been made on granitic melts with water

contents between 0.1 and 1.0 wt. % water prior to this study. Viscosity models largely rely on interpolation between data for anhydrous samples and those containing more than 1 wt.% water, making it necessary to evaluate how these models work at low water contents.

Hess and Dingwell (1996) fits our data to a root mean square deviation (rmsd) of 0.92 log units. This model predicts viscosities that are too high at water contents less than 0.1 wt.%, and too low for water contents above 0.1 wt.% (Figure 5.2a).

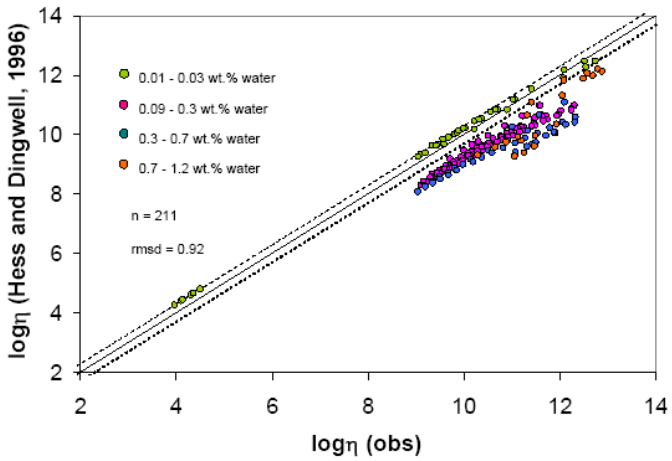


*Figure 5.2a. Measured viscosities plotted against those predicted by Hess and Dingwell (1996). Lines are 1:1 (solid) and +/- 0.3 log units (dashed).*

The model of Zhang et al. (2003) (Figure 5.2b), fitted to viscosity data collected by geospeedometry on Mono Craters obsidians (Zhang et al.1997, 2000), fits our data to an rmsd of 0.79 log units. This model predicts our viscosity data to within plus or minus 0.3

log units at water contents below 0.1 wt.%. It diverges, however, as water contents begin to exceed this value.

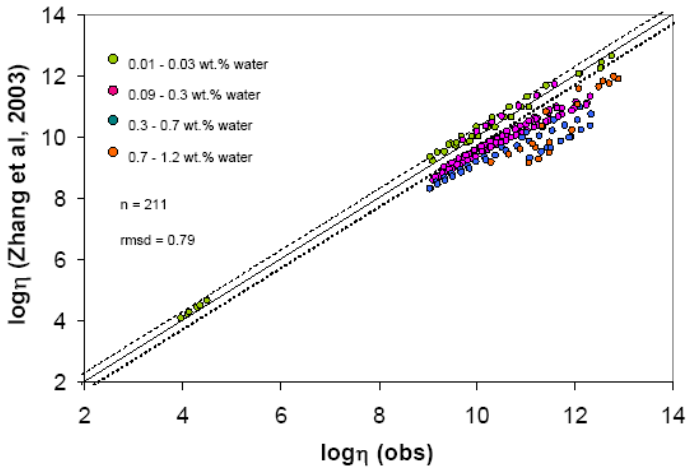


*Figure 5.2b. Measured viscosities plotted against those predicted by Zhang et al. (2003). Lines are 1:1 (solid) and +/- 0.3 log units (dashed).*

The model of Hui and Zhang (2007) (Figure 5.2c) fits our data to an rmsd of 0.46 log units. This model fits our data well for all water contents at viscosities between $10^4$ and $10^{10}$ Pas, but begins to diverge low as viscosities approach the glass transition. This divergence is minimal for near-anhydrous samples, but increases at water contents higher than 0.3 wt.%.

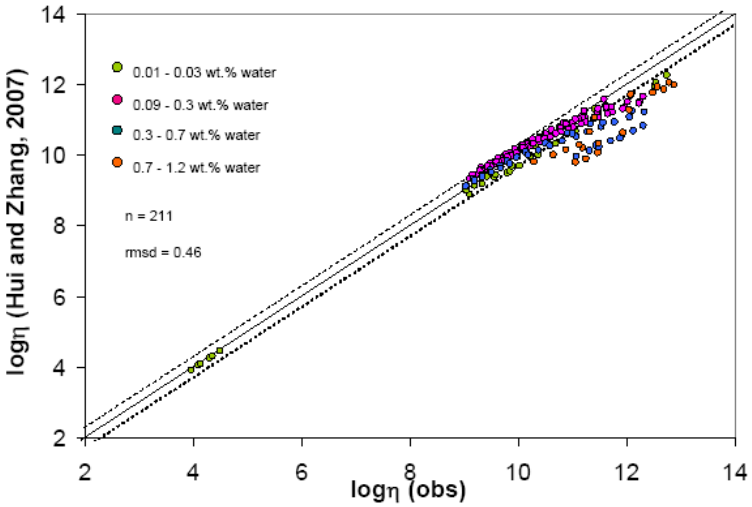


*Figure 5.2c. Measured viscosities plotted against those predicted by Hui and Zhang (2007). Lines are 1:1 (solid) and +/- 0.3 log units (dashed).*

The model of Giordano et al. (2008) (Figure 5.2d) fits our data to an rmsd of 0.72 log units. This model overestimates viscosity by greater than 0.3 log units at high water contents contents.

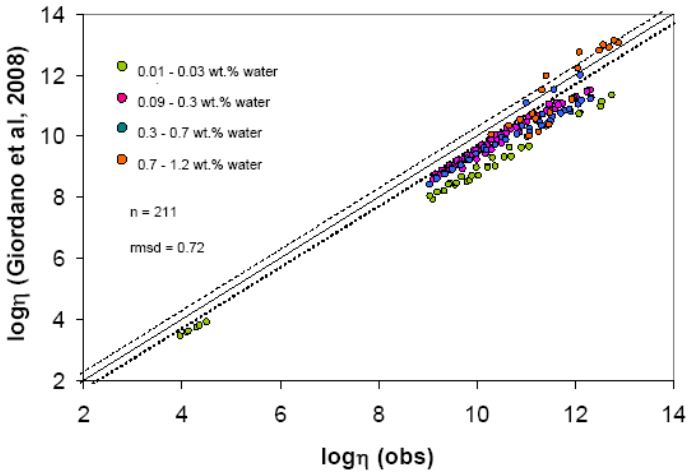


*Figure 5.2d. Measured viscosities plotted against those predicted by Giordano et al. (2008). Lines are 1:1 (solid) and +/- 0.3 log units (dashed).*

Upon evaluating these four models, we can see that Hui and Zhang (2007) gives the most accurate predictions, with an rmsd of 0.46 log units. However, these predictions are still off by a factor of 2.5. In an effort to improve this, we developed our own models based on empirical equations and thermodynamic theory.

## 5.4 TVF and Configurational Entropy Viscosity Models for Mono Craters Rhyolites

We propose two viscosity models for Mono Craters rhyolites, first using the empirical TVF equation, and second using configurational entropy theory. Both models were fitted first to our data alone (n = 211), and second and to our data combined with that used in Zhang et al. (2003) (n = 52). The TVF equation takes the form:

$$\log\eta = A + B/(T-C) \qquad (5.1)$$

where A, B, and C are adjustable parameters dependent on water content and T is temperature in Kelvin.

Our modified TVF model is similar to that of Hess and Dingwell (1996), with an added constant that prevents the model from approaching infinity as the water content approaches zero. It takes the form:

$$\log_{10} \eta = A + (b_1 - b_2 \log_{10} [w + x]) / (T - \{c_1 - c_2 \log_{10} [w + x]\}) \quad (5.2)$$

where T is temperature (K), w is water content (wt.%), and A, $b_1$, $b_2$, $c_1$, $c_2$, and x are adjustable constants.

After adjusting these constants to achieve the smallest rmsd relative to our data, we arrived at the equation:

$$\log_{10} \eta = -4.09 + (14032.6 - 3229.39 \log_{10} [w + 0.11]) / (T - \{0 - 429.9 \log_{10} [w + 0.11]\}) \quad (5.3)$$

which fits our data to an rmsd of 0.24 log units (Figure 5.3).

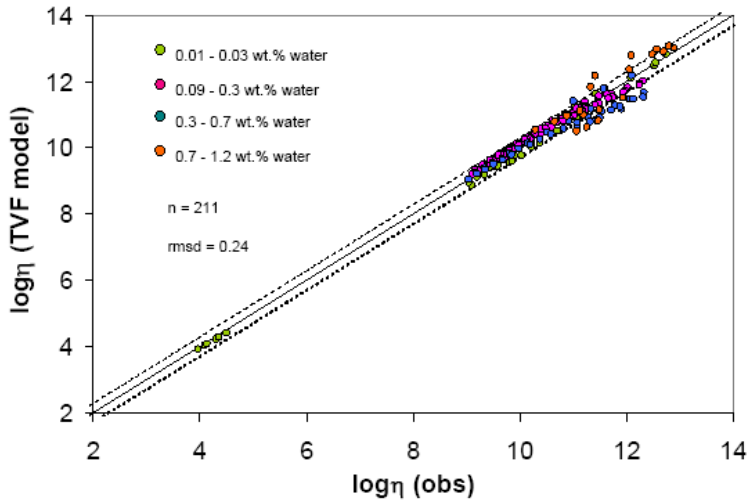


*Figure 5.3. Measured viscosities plotted against those predicted by our TVF model (equation 5.3). Lines are 1:1 (solid) and +/- 0.3 log units (dashed). The samples with between 0.6 and 1 wt.% water have the tendency to fall outside the +/- 0.3 log unit error bars.*

When constants are adjusted to fit the combined data set including the 52 data points from Zhang et al. (2003), we arrive at the equation:

$$\log_{10} \eta = -6.30 + (15702.2 - 2601.39 \log_{10} [w + 0.22]) / (T - \{6.8 - 190.7 \log_{10} [w + 0.22]\}) \quad (5.4)$$

which fits the combined data set to an rmsd of 0.39. This equation fits our data alone with an rmsd of 0.31 log units, and that of Zhang et al. (2003) with an rmsd of 0.61 log units.

While the TVF equation is empirical, the Adam-Gibbs equation is based in configurational entropy theory. The Adam-Gibbs equation takes the form:

$$\log\eta = A + B/(S^{conf}T) \qquad (5.5)$$

where A is an adjustable constant, B is a constant representing the Gibbs free energy (J/mol) preventing structural rearrangement in a melt (Neuville and Richet, 1984), and $S^{conf}$ (T) is configurational entropy (J/molK), which is defined by the following equation:

$$S^{conf}(T) = S^{conf}(T_g) + \int_{Tg}^{T} C_P^{conf}/T \, dT \qquad (5.6)$$

where $S^{conf}(T_g)$ is the configurational entropy at the glass transition, $C_p^{conf}$ is the configurational heat capacity of the melt, and T is in K. $C_p^{conf}$ is defined as the difference between the heat capacity of the liquid ($C_{P,liquid}$) and glass ($C_{P,glass}$) at $T_g$ (Richet et al. 1986):

$$C_P^{conf} = C_{P,liquid} - C_{P,glass}(T_g) \qquad (5.7)$$

During Adam-Gibbs modeling, heat capacities for both the obsidian matrix and water within needed to be taken into account. The heat capacity of the rhyolitic matrix was calculated using an equation given by Neuville et al. (1993) for a very similar obsidian from Little Glass Butte, Oregon:

$$\text{Glass: } Cp = 140.30 - 14.22 \times 10^{-3}T + 6.37 \times 10^{5}/T^{2} - 1594.1/T^{1/2} \qquad (5.8a)$$

$$\text{Liquid: } Cp = 67.51 + 12.24 \times 10^{-3}T \qquad (5.8b)$$

where Cp is in J/gfwK and T is in Kelvin. The effect of water on the heat capacity of the glass and melt was calculated using partial molar heat capacities for $H_2O$ proposed by Bouhifd et al. (2006):

Glass: $C_{p,H2O} = -122.319 + 341.631 \times 10^{-3}T + 63.4426 \times 10^{5}/T^{2}$ (5.9a)

Liquid: $C_{p,H2O} = 85$ (5.9b)

where Cp is in J/molK and T is in Kelvin.

The data from this study, along with those of Zhang et al. (2003) are theoretically modeled using the Adam-Gibbs formulation. The best-fit parameters A, B, and $S^{conf}(T_g)$ were found using the multi-parameter form:

$$A = a_1 + a_2X(H_2O) \quad (5.10a)$$

$$B = b_1 + b_2X(H_2O) + b_3X(H_2O)(1-X(H_2O)) \quad (5.10b)$$

$$S^{conf}(T_g) = c_1 - c_2X(H_2O) - c_3R\{X(H_2O)\ln(X(H_2O)) + (1-X(H_2O))\ln((1-X(H_2O)))\} \quad (5.10c)$$

where a1, a2, b1, b2, b3, c1, c2, and c3 are adjustable parameters, R is the gas constant and $X(H_2O)$ is the mole fraction of water. We explored the possibility of using a constant value for A. However, this lead to a significant increase in total rmsd.

$S^{conf}$ was calculated from $S^{conf}(T_g)$ using equation 5.3. The $C_p^{conf}$ term was calculated from equation 5.4. The $C_{P,liquid}$ term in equation 5.4 was calculated based on equations 5.8 and 5.9 and the mole fractions of water and silicate within the sample:

$$C_{P,liquid} = (67.51 + 12.24 \times 10^{-3}T)(1-X(H_2O)) + 85X(H_2O) \quad (5.11)$$

The $C_{P,glass}(T_g)$ term was also calculated based on equations 5.8 and 5.9

$$C_{P,glass}(T_g) = (140.30 - 14.22 \times 10^{-3}T_g + 6.37 \times 10^{5}/T_g^{2} - 1594.1/T_g^{1/2})X(SiO_2) + (-122.319 + 341.631 \times 10^{-3}T_g + 63.4426 \times 10^{5}/T_g^{2})X(H_2O) \quad (5.12)$$

For these models, the glass transition temperature ($T_g$) was assumed to be $T_{13}$. This was calculated from the individual TVF fits to each experimental sample (Appendix 2).

Our data are and those of Zhang et al. (2003) are best fit with a linear A value. Ideal mixing between the silicate and $H_2O$ is assumed when finding B and $S^{conf}(T_g)$ values. A symmetrical enthalpy value was allowed to be non-ideal via the Margules mixing parameter ($b_2$) for the silicate and $H_2O$. This was used to calculate B. $S^{conf}(T_g)$ was calculated as the entropy formulation for ideal mixing of the silicate and $H_2O$. Treating A as a constant and B and $S^{conf}(T_g)$ as linear, one at a time and altogether, was tried, but resulted in a significant rise in rmsd. Our data were fit to an rmsd of 0.18 log units, lower than the rmsd of 0.24 log units given by our TVF model, using the following formulation for the Adam-Gibbs equation:

$$A = -1.66 - 86.32X(H_2O) \quad (5.13a)$$

$$B = 29.09 - 18.57X(H_2O) - 4.36X(H_2O)(1-X(H_2O)) \quad (5.13b)$$

$$S^{conf}(T_g) = 2.56 - 34.04X(H_2O) - 0.88R\{X(H_2O)\ln(X(H_2O)) + (1-X(H_2O))\ln((1-X(H_2O)))\} \quad (5.13c)$$

where R is the ideal gas constant and $X(H_2O)$ is mole fraction of water. This fit is shown in Figure 5.4.

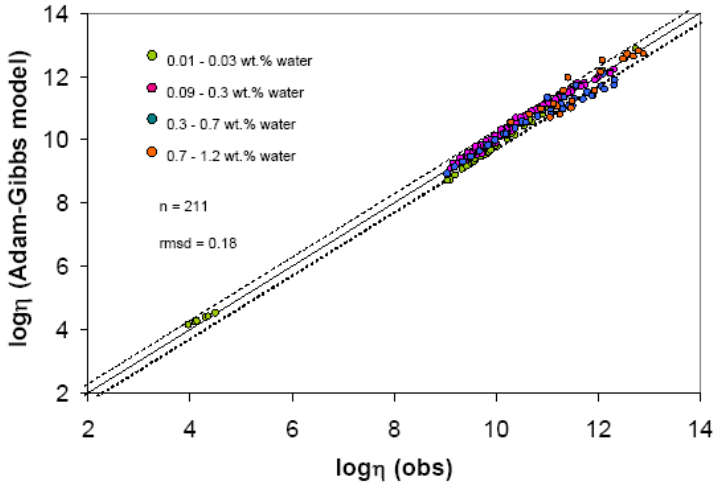


*Figure 5.4. Measured viscosities plotted against those predicted by our Adam-Gibbs model. Lines are 1:1 (solid) and +/- 0.3 log units (dashed). The samples with between 0.6 and 1 wt.% water have the tendency to fall outside the +/- 0.3 log unit error bars.*

With the addition of the data of Zhang et al. (2003), we arrived at the following set of equations:

$$A = -4.61 - 12.05X(H_2O) \quad (5.14a)$$

$$B = 307.12 - 886.43X(H_2O) - 871.68X(H_2O)\,(1-X(H_2O)) \quad (5.14b)$$

$$S^{conf}(T_g) = 17.04 - 262.40X(H_2O) - 8.21R\{X(H_2O)\ln(X(H_2O)) + (1-X(H_2O))\ln((1-X(H_2O)))\} \quad (5.14c)$$

This model for Mono Craters melts fits the collective data set to an rmsd of 0.34 log units. It fits our data set alone to an rmsd of 0.27 log units, and that of Zhang et al. (2003) to an rmsd of 0.53 log units.

The difference in quality of fit between our data set and that of Zhang et al. (2003) is indicative of an inconsistency between data sets. In general, both the TVF and configurational entropy models tend to calculate viscosity values higher than those measured by Zhang et al. (2003), which suggests that, compared to our data, those measurements give values consistently low for a given water content. However, we also

notice that our more hydrous data tend to lie outside of the –0.3 log unit error bar. This suggests that our TVF and configurational entropy models diverge at high water contents. Additional data points above 0.6 wt.% would alleviate this problem. The combined data set of this study and Zhang et al. (2003) is plotted in Figure 5.5.

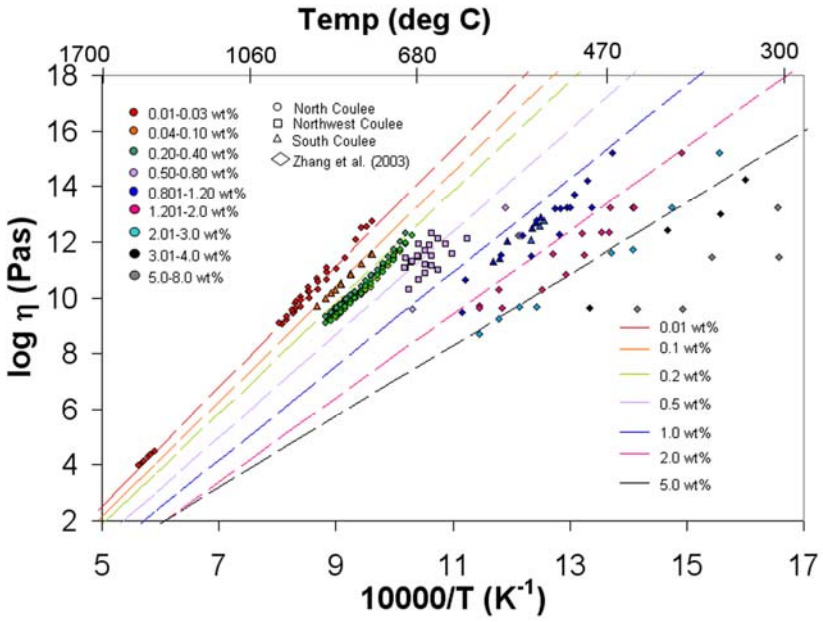


*Figure 5.5. An Arrhenian plot of our data and those of Zhang et al. (2003) overlain with our configurational entropy model.*

## 5.5 Eruption Viscosity and Implications for the Eruptive Behavior in the Mono-Inyo System

Whether a volcano erupts explosively or effusively is governed by a variety of factors, including magma ascent rate, crystallization and water exsolution from the melt due to the rapid decrease in pressure during ascent. Viscosity is a major determinant of magma ascent and volatile exsolution rates, with higher viscosity decreasing both. Viscosity is also the major control on whether rock within the conduit will deform ductily (leading to an effusive eruption) or brittly (leading to an explosive eruption) when

subjected to the stresses associated with magma ascent and volatile exsolution (e.g. Tuffen et al. 2003).

The Mono-Inyo volcanic system is characterized by slow magma ascent rates (~2 cm/s), and is comparable to the average effusion rate (~1.6 cm/s) of the dome lavas (Castro et al. 2002), contradicting the view that those explosive eruptions within the Mono-Inyo system result from high magma ascent rates (Woods and Koyaguchi, 1994). Instead, the explosive eruption dynamics of the Mono-Inyo system are likely due to rapid exsolution of volatiles within the magma body near the surface. The phreatic eruptions within the Inyo system and at Panum Crater, within the Mono Craters system, are a prime example of this. Rhyolite melt will fragment if subjected to rapid decompressions as small as 5 MPa if it exceeds porosities of 60%, which are well within the range of those expected for water-saturated magma residing in the upper 1 km of the conduit (Castro and Gardner, 2008). The explosive nature of the phreatic eruptions within the Mono-Inyo system is largely controlled by stresses associated with rapid volatile exsolution and fragmentation of bubbly obsidian in the near-surface conduit.

While some of the eruptions within the Mono Craters system are rapid and explosive, others are effusive due to the very slow magma ascent and water exsolution rates. The dome formations within the flows exemplify this. Instead of fragmenting, the lava deforms ductily during dome growth.

With an understanding of the source of stress driving the eruptions in the Mono-Inyo system, it is important to evaluate the material properties, viscosity in particular, of the magma within the system. We will look at viscosity values and relaxation times predicted for samples at eruption temperatures.

Using our TVF equations for individual samples, we interpolated viscosities at eruption temperature of 850°C (Gibson and Naney, 1992) within the experimental water content range of 0.01 to 1.1 wt.% (Figure 5.6).

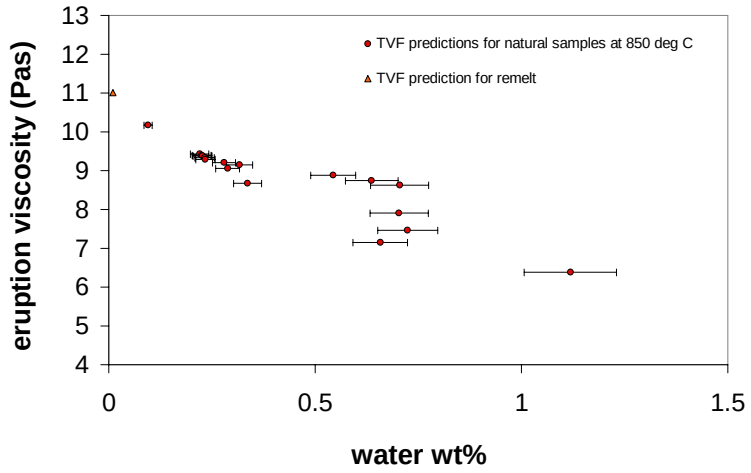


*Figure 5.6. Plot of viscosity as a function of water content as interpolated from TVF equations (Appendix 2).*

It can be seen that eruption viscosity increases dramatically as water content drops below one weight percent and approaches anhydrous conditions, increasing over four orders of magnitude, from ~3 x $10^6$ to ~$10^{10}$ Pas for water contents between 0.1 to 1.1 wt.%. Melts with water contents of ~0.01 wt.% would have eruption viscosities above $10^{11}$ Pas, although such dry melts are not known to exist in the Mono Craters system, and probably do not occur in nature.

Relaxation times can be calculated from the Maxwell relationship:

$$\tau = \eta / G\infty \qquad (5.15)$$

where $\tau$ is relaxation time in seconds, $\eta$ is viscosity, and $G_\infty$, the shear modulus at infinite vibrational frequency, is $10^{10+/-0.5}$ GPa for silicate liquids (e.g. Dingwell and Webb, 1990). Relaxation times associated with the wide range of viscosities in our data set help us understand why the Mono-Inyo steam-driven eruptions tend to be explosive while the

dome lavas tend to be effusive. Just as viscosity rises by four orders of magnitude as a sample drops from 1 wt.% water to anhydrous conditions, relaxation time does the same.

Degassing is thought to be one of the key processes governing explosive versus effusive behavior (e.g. Gonnermann and Manga, 2003). As water exsolves, bubbles form, thus weakening the rock. Strain rates within vesiculating, dehydrating obsidian may exceed rates of structural relaxation, pushing the glass into brittle failure, resulting in an explosion. If water exsolves very slowly, the melt tends to be more fluid and will ascend faster. Bubbles will be able to escape from the melt more easily. The open system degassing within a fluid, easily relaxable melt leads to an effusive eruption and formation of a lava dome structure. Table 5.1 gives the water content measured for each sample, as well as corresponding eruption viscosities and relaxation times interpolated from the data.

Table 5.1. Water content, viscosity and relaxation time of each sample at eruption temperature of 850°C.

| | wt%H2O | log visc at 850C | relax. time (s) |
|---|---|---|---|
| MCSCE | 0.095 | 10.18 | 1.500 |
| MCNCA25 | 0.220 | 9.43 | 0.268 |
| MCNCA32 | 0.225 | 9.40 | 0.250 |
| MCNCA22 | 0.227 | 9.38 | 0.242 |
| MCNCA23 | 0.232 | 9.34 | 0.219 |
| MCNCA24 | 0.234 | 9.29 | 0.197 |
| MCNCC17 | 0.279 | 9.21 | 0.162 |
| MCNCC13 | 0.288 | 9.06 | 0.116 |
| MCNCC19 | 0.317 | 9.16 | 0.144 |
| MCNCC15 | 0.336 | 8.68 | 0.048 |
| MCNWCC22 | 0.544 | 8.88 | 0.076 |
| MCNWCE5 | 0.637 | 8.75 | 0.056 |
| MCNWCF2 | 0.658 | 7.15 | 0.001 |
| MCNWCA1 | 0.704 | 7.91 | 0.008 |
| MCNWCB1 | 0.705 | 8.63 | 0.042 |
| MCNWCA2 | 0.724 | 7.46 | 0.003 |
| MCSCA,D | 1.119 | 6.38 | 0.0002 |

The nature of degassing has a profound effect on the nature of the eruption. During closed-system degassing, all volatiles that exsolve from the melt remain as vapor within the bubbles (Gonnermann and Manga, 2003). Pressure is much more likely to build up within a closed system than an open system. When a closed-system eruption does take place, all of the volatiles will be released at once, resulting in an explosive eruption. Eruptions powered by open-system eruptions tend to be more effusive due to the fact that pressure is released more gradually from a lava that tends to be relatively fluid.

Crystallization also has a profound effect on whether lava will fragment or flow (e.g. Dingwell, 1995). The Einstein-Roscoe relationship (Marsh, 1981) predicts that the addition of 10% crystals to a melt results in a 1.5-fold viscosity increase, a 3-fold increase for 20% crystals, a 6-fold increase for 30%, and a 16-fold increase for 40% crystals. With the addition of 50% crystals, the viscosity increases to 88 times that of a crystal-free melt. The effect of moderate crystal fractions is comparable to that of significant water loss on the viscosity of a melt. The combination of water exsolution and crystallization has the potential to result in fragmentation of the melt. In this light, it is interesting to note that our samples from the effusive flows at Northwest, North, and South coulees contain crystal fractions under 2%. These low crystal fractions may serve to explain why these flows are effusive.

As previously discussed, rapid water exsolution provides the energy necessary for an explosive eruption while weakening the rock via vesiculation, making it more prone to fragmentation. Yet another aspect to this story is revealed in Table 5.1. In addition to pressurizing the conduit, water exsolution also serves to make the melt more brittle. For

example, if stress associated with volatile exsolution is applied within a time on the order of one second, rock above 0.15 wt.% water will behave as a melt, deforming ductily, while obsidian with water contents below that value will behave as a glass, subject to fragmentation due to brittle failure. In a very energetic eruption involving rapid exsolution of large amounts of water, pressure could build very quickly, causing glasses with intermediate water contents and high crystal fractions to fracture explosively. The Bishop Tuff eruption at Long Valley is a prime example of this. Effusive eruptions involve more hydrous, crystal-free, fluid glasses, which allow bubbles to escape as they form, curtailing pressure buildup. The dome formations within the Mono-Inyo system exemplify this.

The steam-driven Mono-Inyo eruptions have, throughout their relatively short history, been energetic and explosive, characterized by ejection of ash, tuff, and crystal-rich obsidian. Effusive eruptions are seen within the coulees, where the lava is able to deform ductily and pile, forming dome structures.

## 5.6 Parameterizing Thermal Diffusivity: A Model and Petrological Implications

### *5.6.1 Modeling thermal diffusivity*

Thermal diffusivity data are modeled by fitting with an inverse temperature function of the form:

$$D = a + b/T + c/T^2 + d\phi \qquad (5.16)$$

Where D is thermal diffusivity in $mm^2/s$, $\phi$ is crystal fraction, T is temperature in Kelvin, and a, b, and c, and d are adjustable constants. With a, b, c, and d adjusted to minimize the rmsd, we attain the following empirical equation:

$$D = 0.454134 + 49.9110/T + 0.2431/T^2 + 1.741\phi \qquad (5.17)$$

This model fits all of our data below T = 780K with an average rmsd of 0.013 $mm^2/s$. When extrapolated to 100% crystallinity at room temperature, we attain a D of 2.34 $mm^2/s$, which is comparable to values for crystal-rich granites and rhyolites (i.e. Whittington et al, 2009).

At the low water contents of glasses in this experiment, water had a negligible effect such that including a parameter for water content produces no significant improvement in the quality of the fit. We recommend using equation 5.8 for crystal free to feldspar-rich rhyolitic glasses with water contents at or below 1 wt.%. Overall, increasing water contents is expected to reduce thermal diffusivity (Hofmeister et al. 2006), making a term describing the effect of water necessary. A series of laser flash experiments on hydrous glasses will be critical before making a quantitative conjecture on how water affects thermal diffusivity in rhyolites.

*5.6.2 Effect on conductivity*

Thermal conductivity is calculated as the product of density, heat capacity, and thermal diffusivity:

$$k = \rho C_p D \qquad (5.18)$$

where k is in kg/mKs, ρ is in kg/m$^3$, $C_p$ is in J/molK, and D is in m$^2$/s. As temperature rises, heat capacity increases and thermal diffusivity decreases. Density decreases only slightly (Fig. 5.7). The result of this is that conductivity changes less than $C_p$ or D, increasing around 30% between the lower and upper temperature ranges of these experiments.

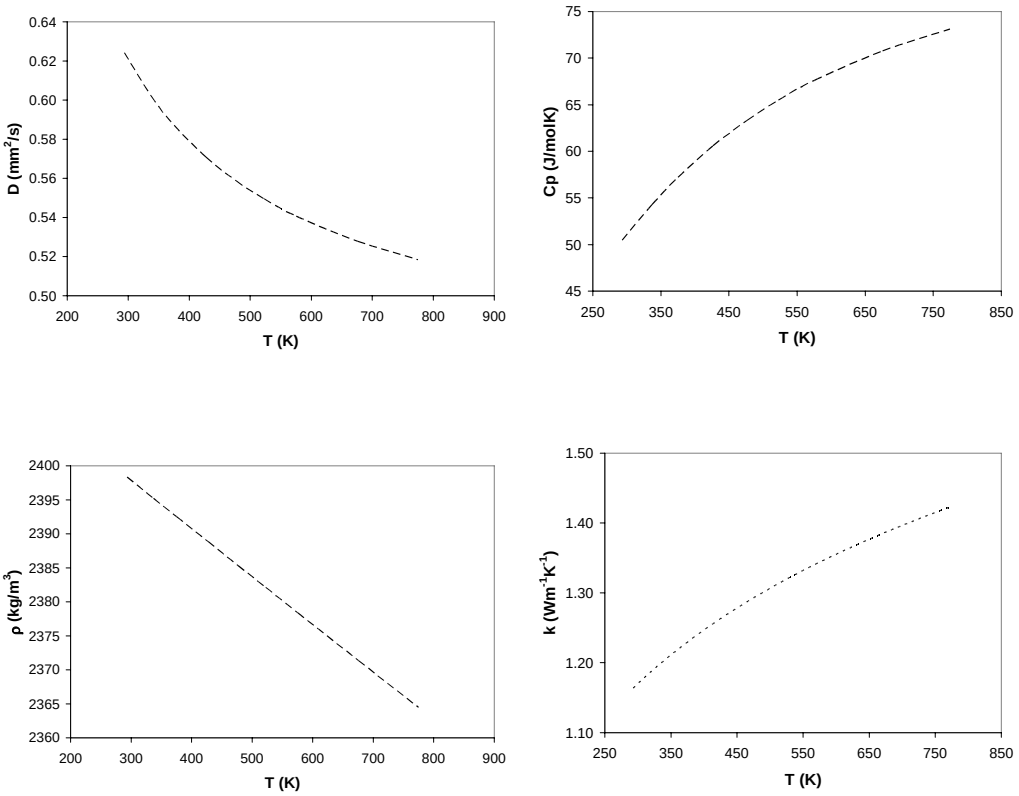


*Figure 5.7. Thermal diffusivity (top left), heat capacity (top right), and density (bottom left) plotted against temperature. These counteract each other to yield conductivities (bottom right) between 0.07 and 0.10 $Wm^{-1}K^{-1}$, rising with temperature. Cp calculated from Neuville et al. (1993). Density calculated from expansivity values in Carmichael and Lange (1990).*

*5.6.3 Thermal diffusivity bounds and the problem of a cooling dike*

Thermal diffusivity values for Mono Craters glasses drop from around 0.65 $mm^2/s$ at room temperature to 0.55 $mm^2/s$ as the sample approaches the glass transition. Petrological implications of variable thermal diffusivity can be explored by considering the one-dimensional problem of a cooling dike, a problem relevant to relatively small magma intrusions or a short-lived volcanic neck. We consider a 2 meter wide dike at a temperature of 1100 K instantaneously emplaced into 300 K country rock. We assume the dike quenches to a glass (i.e. no crystallization occurs) and that the dike and country rock have similar thermal properties. We use the analytical solution from Jaeger, 1965:

$$(T-T_s)/(T_o-T_s) = \tfrac{1}{2}(\mathrm{erf}((h-x)/(2\sqrt{(Dt)})) + \mathrm{erf}((h+x)/(2\sqrt{(Dt)}))) \qquad (5.19)$$

where $T_o$ is the dike's emplacement temperature in K, $T_s$ is the country rock temperature in K, h is the half width of the dike (m), x is distance from the center of the dike (m), t is time in seconds, and D is thermal diffusivity ($m^2/s$). We consider two thermal diffusivity values, 1 $mm^2/s$, commonly used in the literature, and 0.5 $mm^2/s$, the lower bound of our thermal diffusivity data. Heat flow calculations for 1 hr, 10 hr, 100 hr, 1000 hr, and 10000 hr after emplacement are presented in Figure 5.8.

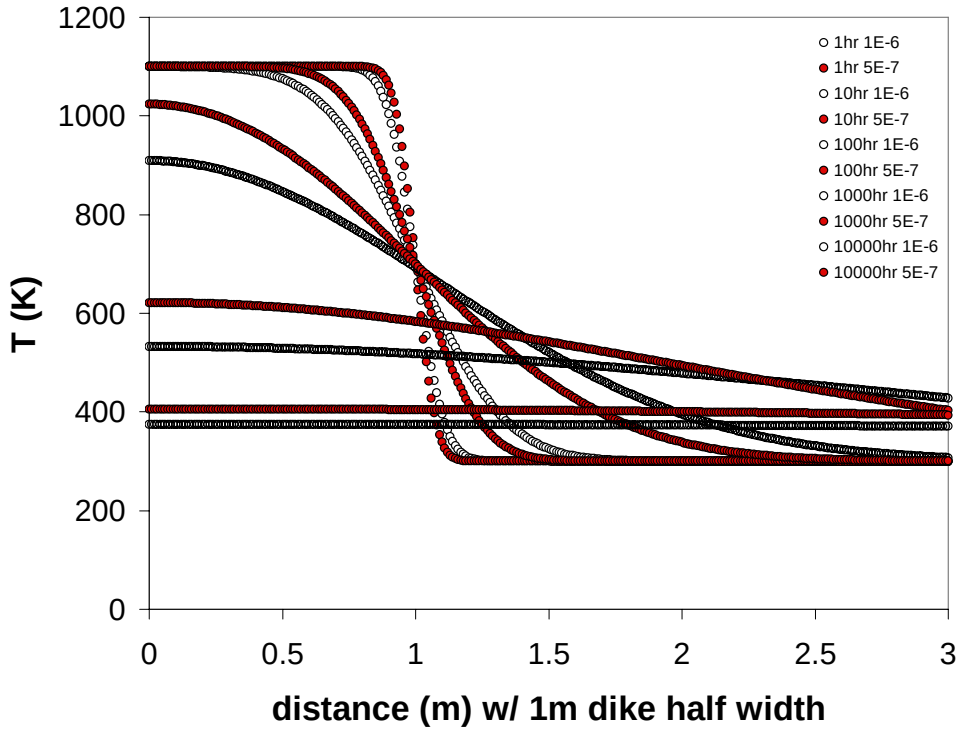


*Figure 5.8. Heat flow calculations for a 1 m wide dike instantaneously emplaced into homogeneous country rock with similar properties, and quenched to a glass.*

A few relatively intuitive, but important, observations can be made from Figure 5.8. First, a higher thermal diffusivity allows heat to leave the dike and flow into the country rock more quickly. In this case, doubling thermal diffusivity halves the time it takes for heat to transfer into the country rock. This has important implications for contact metamorphism around the dike, for lower thermal diffusivity allows rocks to be exposed to a heat pulse for a longer time, twice as long in this case. A thermal diffusivity of 1 $mm^2/s$ results in a 300 hr thermal decay time, while a thermal diffusivity of 0.5 $mm^2/s$ would increase this time to 600 hr, after which the dike and country rock would cool at equal rates. Our data suggest that a 1 m wide dike at Mono Craters would take around 500 hr to reach within 700 K of the original country rock temperature. At this

point, the country rock far away from the dike has reached its maximum temperature and also begins to decay with time.

Our data suggest a very low D at high T. It drops by about 20% as temperatures climb from room temperature to 600K. This suggests that, as rocks heat up, they will tend to hold their heat longer. In the case of the dike, it will cool more quickly as time passes and its temperature drops, while the country rock will accept heat less readily as its temperature rises. With variable thermal diffusivity used to describe this system, the country rock will remain at higher temperatures longer, yielding more efficient recrystallization than if the room temperature constant of 1 $mm^2/s$ is used.

In the case of glass, the change in thermal diffusivity with temperature is relatively small, and the drop with temperature is negligible when considering the other uncertainties inherent in thermal modeling. However, the drop is more apparent when considering crystal-rich magmas which have higher, and more temperature-dependent D.

When a dike does not quench to a glass, but instead crystallizes as it cools, thermal diffusivity increases by 3 or 4 times (Figure 5.9). Thermal diffusivity varying by this amount allows the dike to cool more quickly at lower temperatures. Crystalline country rock, on the other hand, will hold onto heat over twice as long as it approaches temperatures around 400K, and four times as long when reaching temperatures above 700K, allowing much more time for crystallization to occur in the rock surrounding the dike. Additionally, due to the fact that most magma intrusions are emplaced at depth, the country rock around the dike is normally well above that of the surface, further enhancing the heat flow retardant effect of lower thermal diffusivity. The importance of these factors increases as intrusion width, and thus cooling time, increases.

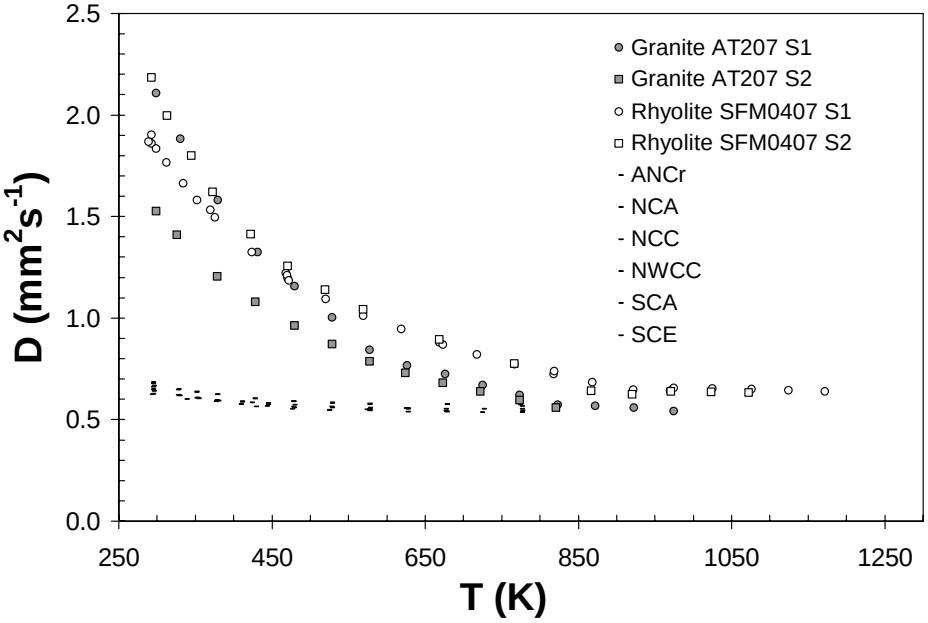


*Figure 5.9. Thermal diffusivity data from this study compared with data from Whittington et al. (2009) for crystalline granite and rhyolite.*

## 5.7 Conclusions

We have used the parallel plate and concentric cylinder methods to measure viscosity between $5 \times 10^3$ to $8 \times 10^{12}$ Pas from superliquidus temperatures to the glass transition and the laser flash (LFA) method to measure thermal diffusivity between 0.5 and 0.7 $mm^2/s$ from the subliquidus to room temperatures. Of the four viscosity models relevant to rhyolites existing in the literature, the global model of Hui and Zhang (2007) provides the best fit to our data. The TVF and configurational entropy models developed in this study fit our data 2.5 times better than this, suggesting there is still work to be done in the modeling of silicate melt viscosity. Our models begin to diverge at water contents above 0.7 wt.%. This makes sense, as a majority of the viscosity data collected

in this study are at water contents below 0.4 wt.%. More data on melts with higher water contents would improve this.

There are presently no models for the thermal diffusivity of rhyolitic glasses and melts. The model formulated in this study can be used to predict the thermal diffusivity of an obsidian having water contents at or below 1 wt.% at temperatures below the glass transition. While crystal contents of the obsidians do not exceed 2 vol. %, extrapolation of the model to 100 vol.% gives a value similar to that of plagioclase, suggesting that the model can be extrapolated to any crystal fraction.

This model can be improved two ways. First, data at higher water contents would allow the inclusion of a constant describing the effect of water on thermal diffusivity. Additional data on obsidians with water contents between 1 and 10 wt.% would be extremely useful for this endeavor. Second, collecting data at higher temperatures would allow for modeling of thermal diffusivity as the sample goes through the glass transition and becomes a melt. While our data show the general drop in thermal diffusivity as the sample goes through the glass transition and the leveling off of D as it becomes a melt, the data cannot be used for modeling due to the fact that the samples deformed at high temperatures. A different container will need to be used in order to prevent the sample from deforming during data collection.

The nature of volcanic processes, including rate of magma ascent, exsolution of volatiles, eruption style, and flow distance, is highly dependent on the viscosity of the associated magma and its ability to transfer heat. The data and modeling presented in this study is a step in the direction of gaining a better understanding of the eruption dynamics

of Mono Craters and other rhyolitic flows. Data on more hydrous obsidians will make for more complete modeling, which we will leave to future studies.

### 5.7 Summary

* Our data, covering water contents between 0.01 and 1.1 wt.%, allow us to test literature models of rhyolitic melt viscosity at low $H_2O$ contents which are crucial for understanding conduit processes. Four recent models reproduce our data with rmsd's between 0.95 and 0.46 log units.

* Our data are modeled via the Adam-Gibbs theory of relaxation in melts. Ideal mixing is assumed between $H_2O$ and melt. The Adam-Gibbs model fits our data alone to 0.26 log units, and the combined data set including data from Zhang et al. (2003) to an rmsd value of around 0.3 log units. These are comparable to the quality of fit obtained using the empirical TVF equation.

* Water exsolution and crystallization at shallow depths drives the explosive eruptions at Mono Craters. While dissolved water tends to lower the viscosity of glass, making an eruption more effusive, it also can rapidly exsolve as the magma crystallizes, imparting energy to the eruption and making it more explosive.

* An inverse T relation, with an added factor for crystallinity, is used to model our thermal diffusivity data, fitting it to an average rmsd value of 0.013 $mm^2/s$.

* Thermal conductivity increases only slightly with temperature due to the fact that, while thermal diffusivity goes down with temperature, heat capacity and density go up.

* The difference between selecting a constant thermal diffusivity and using our model for variable thermal diffusivity is negligible when considering thermo-rheological problems

on glasses. However, thermal diffusivity varies much more in crystalline samples. Thus, temperature-dependent thermal diffusivity needs to be considered in scenarios involving heat transfer within crystal-rich magmatic systems.

## References


Blumm, J. and Lemarchand, S., (2002). Influence of test conditions on the accuracy of laser flash measurements. *High Temp High Pres* 34:523-528.

Bottinga, Y. and Weill, D.F., (1972). The viscosity of magmatic silicate liquids: a model for calculation. *American Journal of Science*. Vol. 272, pp. 438-475.

Bouhifd, A., Whittington, A., Roux, J., and Richet, P., 2006. Effect of water on the heat capacity of polymerized aluminosilicate glasses and melts. *Geochimica et Cosmochimica Acta*, v. 70, p.711-722.

Branlund, J.M. and Hofmeister, A.M., (2007). Thermal diffusivity of quartz to 1000 °C: effects of impurities and the α–β quartz transition. *Phys Chem Minerals* 34:581-595.

Lange, R. and Carmichael, I., 1992. Thermodynamic properties of silicate liquids with emphasis on density, thermal expansion and compressibility. *Reviews in Mineralogy and Geochemistry*; January 1990; v. 24;1; p. 25-64.

Carrichi, L., Burlini, L., Ulmer, P., Gerya, T., Vassalli, M., and Papale, P., (2007). Non-Newtonian rheology of crystal-bearing magmas and implications for magma ascent dynamics. *Earth and Planetary Science Letters* 264:402-419.

Jaeger, J.C., 1965. Terrestrial Heat Flow. *American Geophysical Union of the National Academy of Sciences.*

Castro, J.M. and Gardner, J.E., (2008). Did magma ascent rate control the explosive-effusive transition at the Inyo volcanic chain, California? *Geology*, vol.36; no.4; pp. 279-282.

Castro, J.M., Manga, M., and Cashman, K.V., (2002). Dynamics of obsidian flows inferred from microstructures: Insights from microlite-preferred orientations. *Earth and Planetary Science Letters* 99:211-226.

Degiovanni, A., Andre, S. and Maillet, D., (1994). Phonic conductivity measurement of a semi-transparent material. In: Tong TW (ed). Thermal conductivity, vol.22. Technomic, Lancaster, pp. 623-633.

Dingwell, D.B., (1995). Viscosity and anelasticity of melts. Mineral Physics and Crystallography: A Handbook of Physical Constants. American Geophysical Union.

Dingwell, D.B., Romano, C., and Hess, K.-U., 1996. The effect of water on the viscosity of a haplogranitic melt under *P-T-X* conditions relevant to silicic volcanism. *Contributions to Mineralogy and Petrology*, v. 124, p. 19-28.

Dingwell, D.B., and Webb, S.L., (1990). Relaxation in silicate melts. *European Journal of Mineralogy*, v. 2, p. 427-449.

Dingwell, D.B. and Webb S.L., (1989). Structural relaxation in silicate melts and non-Newtonian melt rheology in geologic processes. *Physics and Chemistry of Minerals,* vol. 16, pp. 508-516.

Dorfman, A., Hess, K-U., and Dingwell, D.B., 1996. Centrifuge-assisted falling sphere viscometry. *European Journal of Mineralogy*, v.8, p. 507-514.

Einstein, A., (1906). Eine neue Bestimmung der Molekuldimensionen, *Ann. Phys.*, 19, 289– 306.

Friedman, I., Long, W., and Smith, R.L., 1963. Viscosity and water content of rhyolite glass. *Journal of Geophysical Research*, v. 68, p. 6523-6535.

Getson, J. M., and A. G. Whittington, (2007). Liquid and magma viscosity in the anorthite-forsterite-diopside-quartz system and implications for the viscosity-temperature paths of cooling magmas, *J. Geophys. Res.*, 112, doi:10.1029/2006JB004812

Gibson, R. G., and M. T. Naney, (1992). Textural development of mixed, finely porphyrititc silicic volcanic rocks, Inyo Domes, eastern California, *J. Geophys. Res.*, 97, 4541– 4559.

Giordano, D., Mangiacapra, A., Potuzak, M., Russell, J., Romano, C., Dingwell, D., and Di Muro, A., (2006). An expanded non-Arrhenian model for silicate melt viscosity: a treatment for metaluminous, peraluminous, and peralkaline liquids. *Chemical Geology* 229: 42-56.

Giordano, D., Russell, J.K., and Dingwell, D.B., 2008. Viscosity of magmatic liquids: A model. *Earth and Planetary Science Letters,* Vol. 271, 1-4: 123-134.

Gonnermann, H. and Manga, M. (2005). Nonequilibrium magma degassing: Results from the modeling of the ca. 1340 A.D. eruption of Mono Craters, California. *Earth and Planetary Science Letters.* 238: 1-16.

Hess, K.-U., Dingwell, D.B., and Webb, S.L., 1995. The influence of excess alkalis on the viscosity of a haplogranitic melt. *American Mineralogist*, v. 80, p. 297-304.

Hess, K.-U., Dingwell, D.B., (1996). Viscosities of hydrous leucogranitic melts: a non-Arrhenian model. *Am. Mineral*. 81, 1297–1300.

Hofer, M. and Schilling, F. R., (2002). Heat transfer in quartz, orthoclase, and sanidine at elevated temperature. *Phys. Chem. Miner*. 29:571-584.

Hofmeister, A. M., M. Pertermann, J. M. Branlund, and A. G. Whittington, (2006). Geophysical implications of reduction in thermal conductivity due to hydration, Geophys. Res. Lett., 33, L11310, doi:10.1029/ 2006GL026036.

Hui, H. and Y. Zhang., (2007). Toward a general viscosity equation for natural anhydrous and hydrous silicate melts. *Geochimica et Cosmochimica Acta* 71: 403–416.

Ihinger P. D., Hervig R. L., and McMillan P. F., ( 1994). Analytical methods for volatiles in glasses. *Rev. Mineral*. 30, 67- 121.

Izett, G.A., Obradovich, J.D. and Mehnert, H.H., (1988). The Bishop ash bed (middle Pleistocene) and some older (Pliocene and Pleistocene) chemically and mineralogically similar ash beds in California, Nevada, and Utah. *U.S. Geological Survey Bulletin*, 1675 37 pp.

Lee, D.W. and Kingerly, W.D., (1960). Radiation energy transfer and thermal conductivity of ceramic oxides. J. Am. Cer. Soc. 43:594-607.

Lejeune, A.M., Bottinga, Y., Trull, T.W., and Richet, P., (1999). Rheology of bubble-bearing magmas. *Earth and Planetary Science Letters,* Vol. 166, 1-2:71-84.

Manga, M., Castro, J., Cashman, K.V., and Loewenberg, M., Rheology of bubble-bearing magmas. *J. of Volc. and Geo. Res.*, Vol. 87, 1-4:15-28.

Manga, M. and Loewenberg, M., (2001). Viscosity of magmas containing highly deformable bubbles. *J. of Volc. and Geo. Res.*, 105:19-24.

Marsh, B., (1981). On the crystallinity, probability of occurrence, and rheology of lava and magma, *Contrib. Mineral. Petrol*., 78, 85– 98.

Mehling, H., Hautzinger, G., Nilsson, O., Fricke, J. Hoffmann, R., and Hahn, O., (1998). Thermal diffusivity of semi-transparent materials determined by the laser-flash method applying a new mathematical model. *Int. J. Technophys*. 19:941-949.

Mysen, B.O. and Richet, P. (2005). Silicate glasses and melts: properties and structure. 1st ed. Amsterdam; Boston: Elsevier.

Neuville, D., Courtial, P., Dingwell, D. and Richet, P. 1993. Thermodynamic and rheological properties of rhyolite and andesite melts. Contrib. Mineral. Petrol. 113: 572-581.

Newman, S., Stolper, E.M., and Epstein, S., (1986). Measurment of water in rhyolitic glasses: calibration of an infrared spectroscopic technique. *Am. Mineral.,* Vol. 71, pp. 1527-1541.

Osako, M., Ito, E., and Yoneda, A., (2004). Simultaneous measurements of thermal conductivity and thermal diffusivity for garnet and olivine under high pressure. *Phys. Earth Planet Inter.* 143,144:311-320.

Persikov, E.S., Zharikhov, V.A., Bukhtiyarov, P.G., and Pol'skoy, S.F., 1990. The effect of volatiles on the properties of magmatic melts. *European Journal of Mineralogy*, v.2., p. 621-701.

Pertermann, M. and Hofmeister, A.M., (2006). Thermal diffusivity of olivine group minerals. *Am. Mineral.* 91:1747-1760.

Pertermann, M., Whittington, A.G., Hofmeister, A.M., Spera, F.J., and Zayak, J., (2008). Thermal diffusivity of orthoclase glasses and single-crystals at high temperature. *Contributions to Mineralogy and Petrology*, v. 155, p. 689-702.

Pertermann, M., Branlund, J., Whittington, A., and Hofmeister, A., (2007). Thermal diffusivity of pyroxene, feldspar, and silica melts, glasses, and single crystals at high temperature. AGU Fall Meeting Abstracts.

Richet, P., 1984. Viscosity and configurational entropy of silicate melts. *Geochimica et Cosmochimica Acta,* vol. 48, Issue 3, pp.471-483

Richet, P., Robie R.A., and Hemingway, B.S., 1986. Low-temperature heat capacity of diopside glass ($CaMgSi_2O_6$): a calorimateric test of the configurational entropy theory applied to the viscosity of liquid silicates. *Geochimica et Cosmochimica Acta*, v. 50, p. 1521-1533.

Richet, P and Bottinga, Y., (1995). Rheology and configuration entropy of silicate melts. In: Stebbins, J., McMillan, P.F., Dingwell, D.B. (Eds.), Structure, Dynamics and Properties of Silicate Melts. *Reviews in Mineralogy*, vol. 32. pp.21-66.

Roscoe, R., (1952). The viscosity of suspensions of rigid spheres, *Br. J. Appl. Phys*., 3, 267–269.

Rust, A.C. and Manga, M., (2002). Effects of bubble deformation on the viscosity of dilute suspensions. *J. Non-Newtonian Fluid Mech*. 104:53-63.

Scaillet, B., Holtz, F., Pichavant, M., and Schmidt, M., 1996. Viscosity of Himalayan leucogranites: implications for mechanisms of granitic magma ascent. *Journal of Geophysical Research*, v. 101, p. 27691-27699.

Scherer, G.W., (1984). Use of the Adam-Gibbs equation in the analysis of structural relaxation. *J. Am. Cer. Society*., 67: 504-511.

Shaw H.R., 1963. Obsidian-$H_2O$ viscosities at 1000 and 2000 bars in the temperature range 700˚C to 900˚C. *Journal of Geophysical Research*, v. 68, p. 6337-6343.

Shaw, H.R., (1965). Comments on viscosity, crystal settling, and convection in granitic magmas. *American Journal of Science.* Vol. 263, pp.120-152.

Shaw, H.R., (1972). Viscosities of magmatic silicate liquids: an empirical method of prediction. *American Journal of Science*. 272, 870–893.

Stein, D.J and Spera, F.J., (2002). Shear viscosity of rhyolite-vapor emulsions at magmatic temperatures by concentric cylinder rheometry. *J. of Volc. and Geo. Res*. 113:243-258.

Stephenson, R.J., Dingwell, D.B, Webb, S.L., and Sharp, T.G., (1996). Viscosity of microlite-bearing rhyolitic obsidians: an experimental study. *Bull. Volcanol*., 58:298-309.

Stolper, E., 1982. The speciation of water in silicate melts. *Geochimica et Cosmochimica Acta*, v. 46, p. 2609-2620.

Taylor, G.I., (1932). The viscosity of a fluid containing small drops of another fluid. *Proc. R. Soc. London*, Ser. A 138:41-48.

Tuffen, H., Dingwell, D.B., and Pinkerton, H., (2003). Repeated fracture and healing of silicic magma generate flow banding and earthquakes? *Geology*; December 2003; v. 31; no. 12; p. 1089-1092.

Vand, V., (1948). Viscosities of solutions and suspension. *I. Theory: Jour. Phys. Coll. Chem.*, vol. 52, p. 277-299.

Whittington, A., Richet, P., Behrens, H., Holtz, F., and Scaillet, B., 2004. Experimental temperature-X($H_2O$)-viscosity relationship for leucogranites, and comparison with synthetic silicic liquids. *Transactions of the Royal Society of Edinburgh: Earth Sciences*, v. 95, p. 59-72.

Whittington, A.G., Hellwig, B.M., Behrens, H., Joachim, B., Stechern, A., and Vetere, F. The viscosity of hydrous dacitic liquids: Implications for the rheology of evolving silicic magmas. Bull. Volc., in press.

Whittington, A., Hofmeister, A., Nabelek, P., (2009). Temperature-dependent thermal diffusivity of Earth's crust: Implications for crustal anatexis. In prep.

Woods, A. and Koyaguchi, T., (1994). Transitions between explosive and effusive eruptions of silicic magmas. *Nature*, 370:641-644.

Zhang, Y., Jenkins, J., and Xu, Z. (1997b). Kinetics of the reaction H2O + O = 2OH

in rhyolitic glasses upon cooling: geospeedometry and comparison with glass transition. Geochimica et Cosmochimica Acta, 61, 2167–2173.

Zhang, Y., Xu, Z., and Behrens, H. (2000) Hydrous species geospeedometer in rhyolite: improved calibration and application. Geochimica et Cosmochimica Acta, 64, 3347–3355.

Zhang, Y., Xu, Z., Liu, Y., (2003). Viscosity of hydrous rhyolitic melts inferred from kinetic experiments, and a new viscosity model. *Am. Mineral*. 88, 1741–1752.

## Appendix A—Micrographs of Obsidian Samples

Figure A1-1. NCA confocal 3D rendering ***(224 x 224 x 100 μm)***

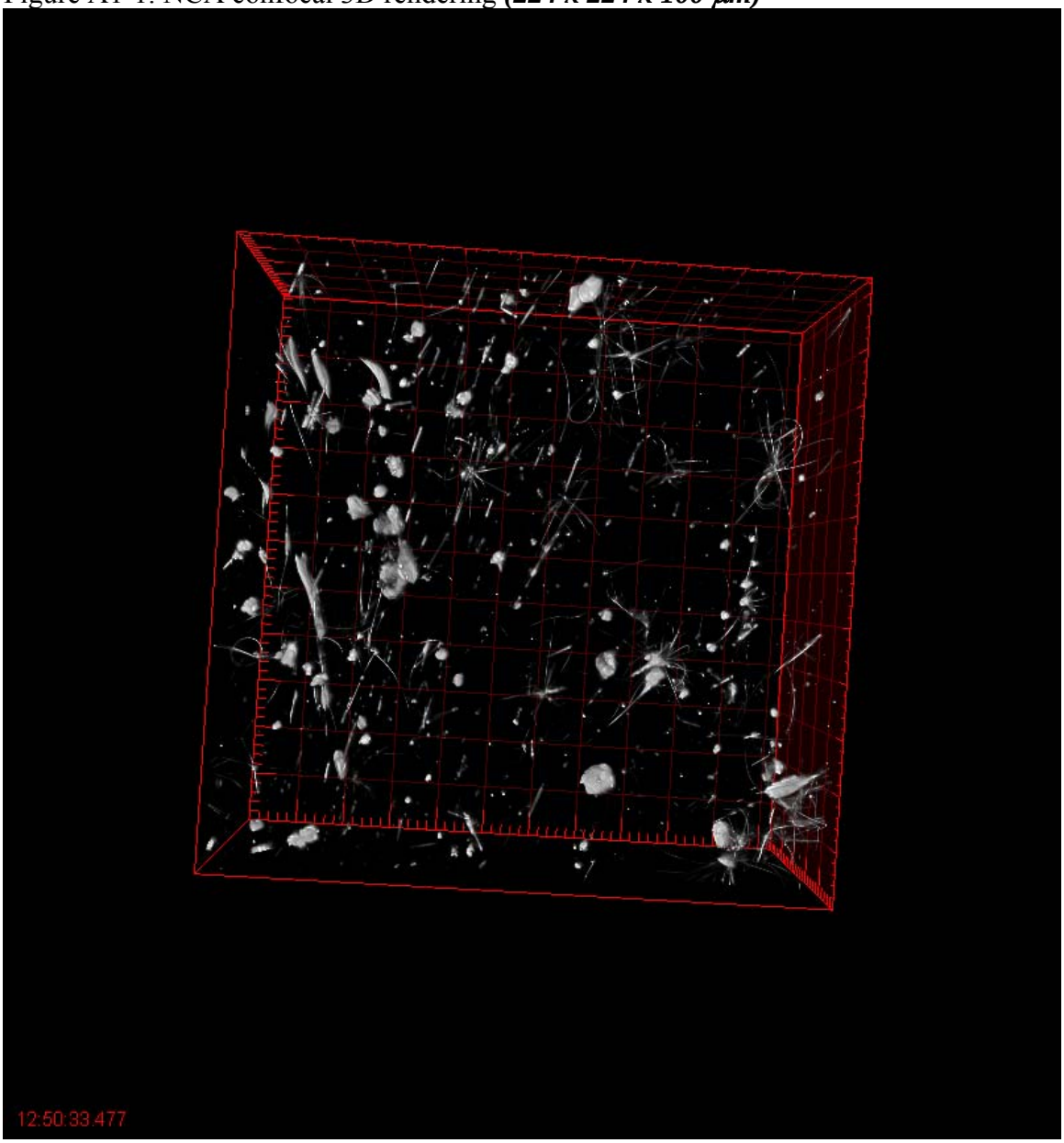

Figure A1-2. NCA#1 light micrograph ***(2.5 x 2.5 mm)***

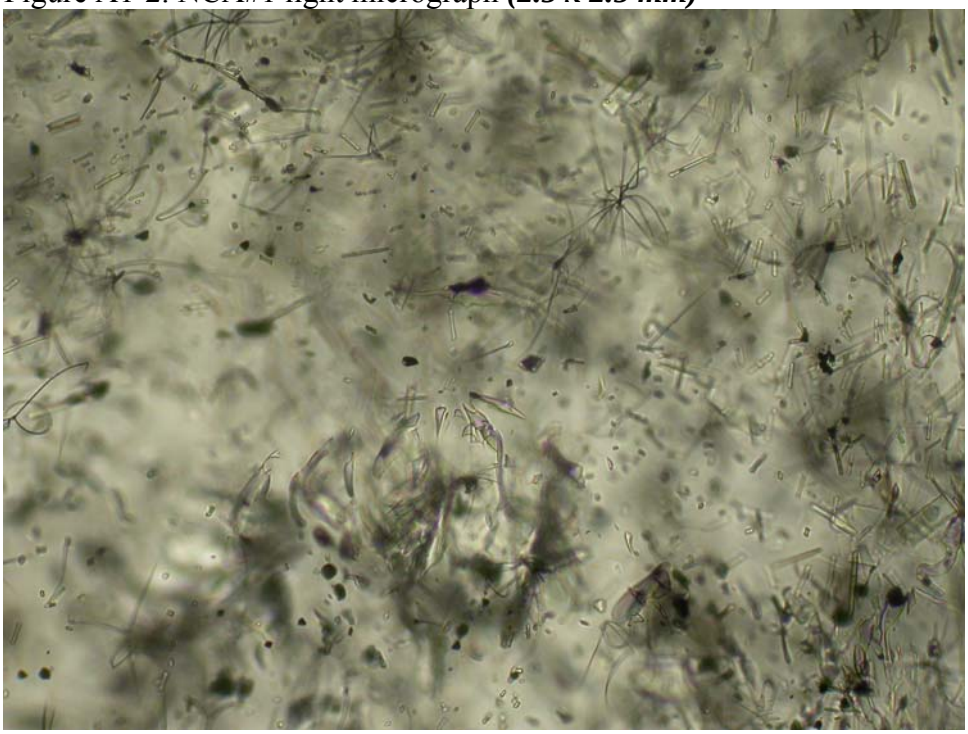

Figure A1-3. NCA#2 light micrograph ***(2.5 x 2.5 mm)***

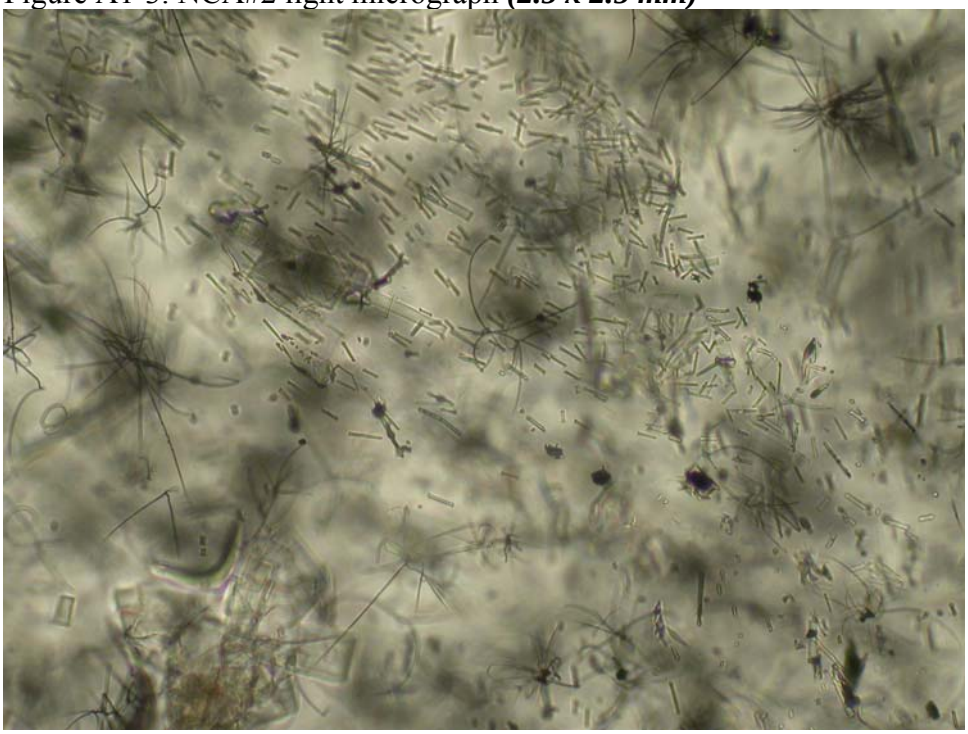

Figure A1-5. NCA#3 light micrograph ***(2.5 x 2.5 mm)***

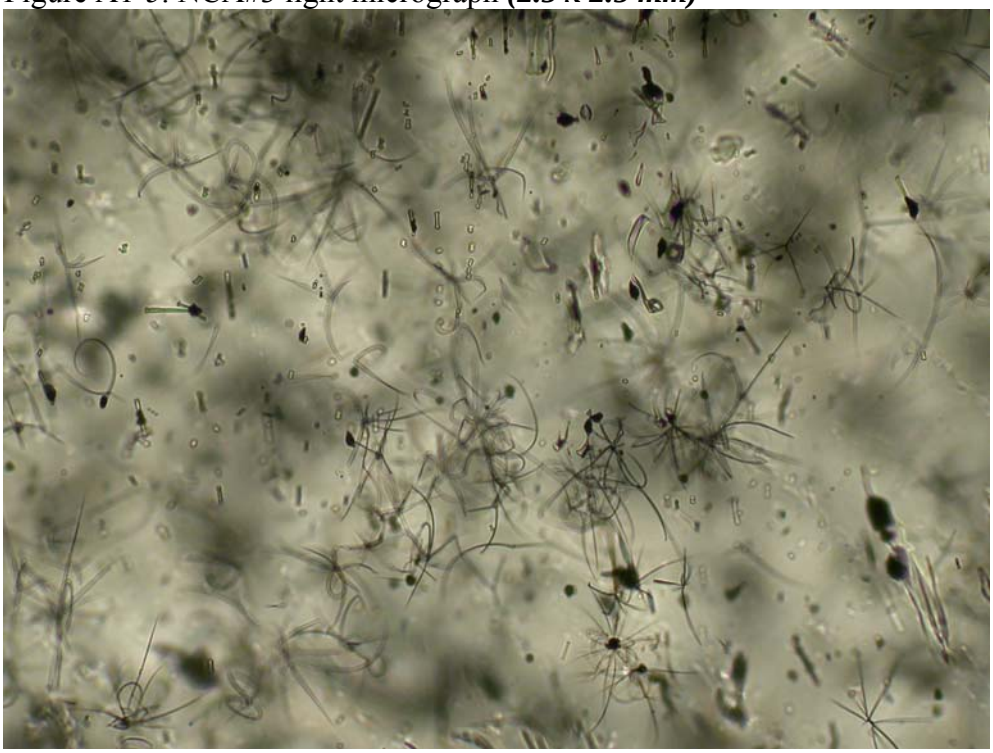

Figure A1-6. NCA#4 light micrograph ***(2.5 x 2.5 mm)***

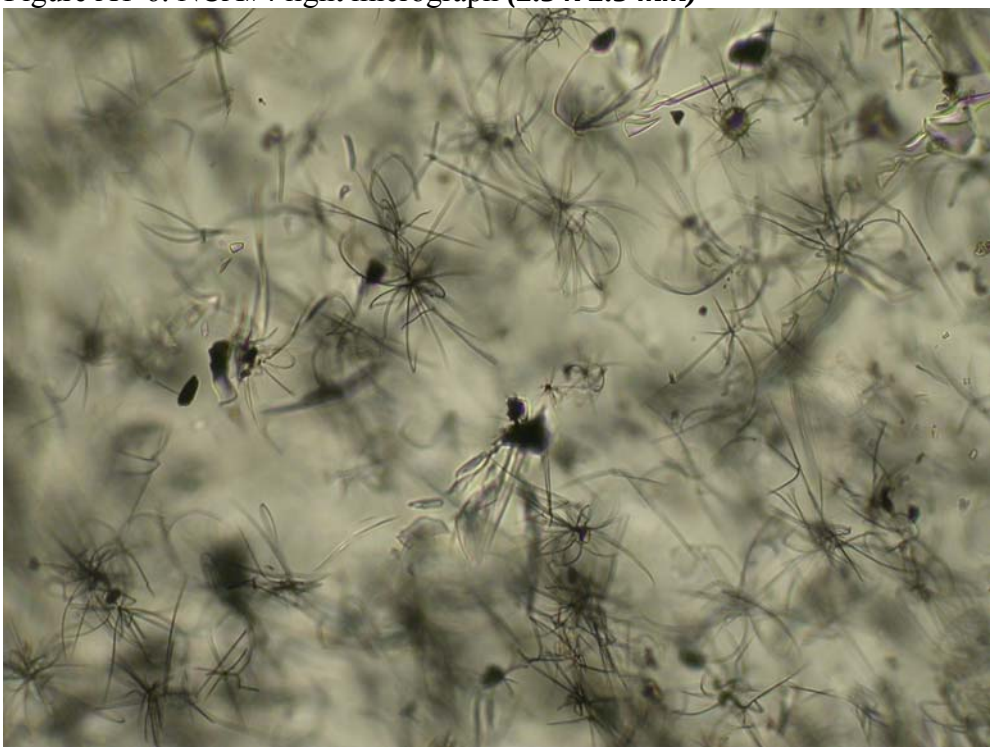

Figure A1-7. NCC confocal 3D rendering ***(224 x 224 x 100 μm)***

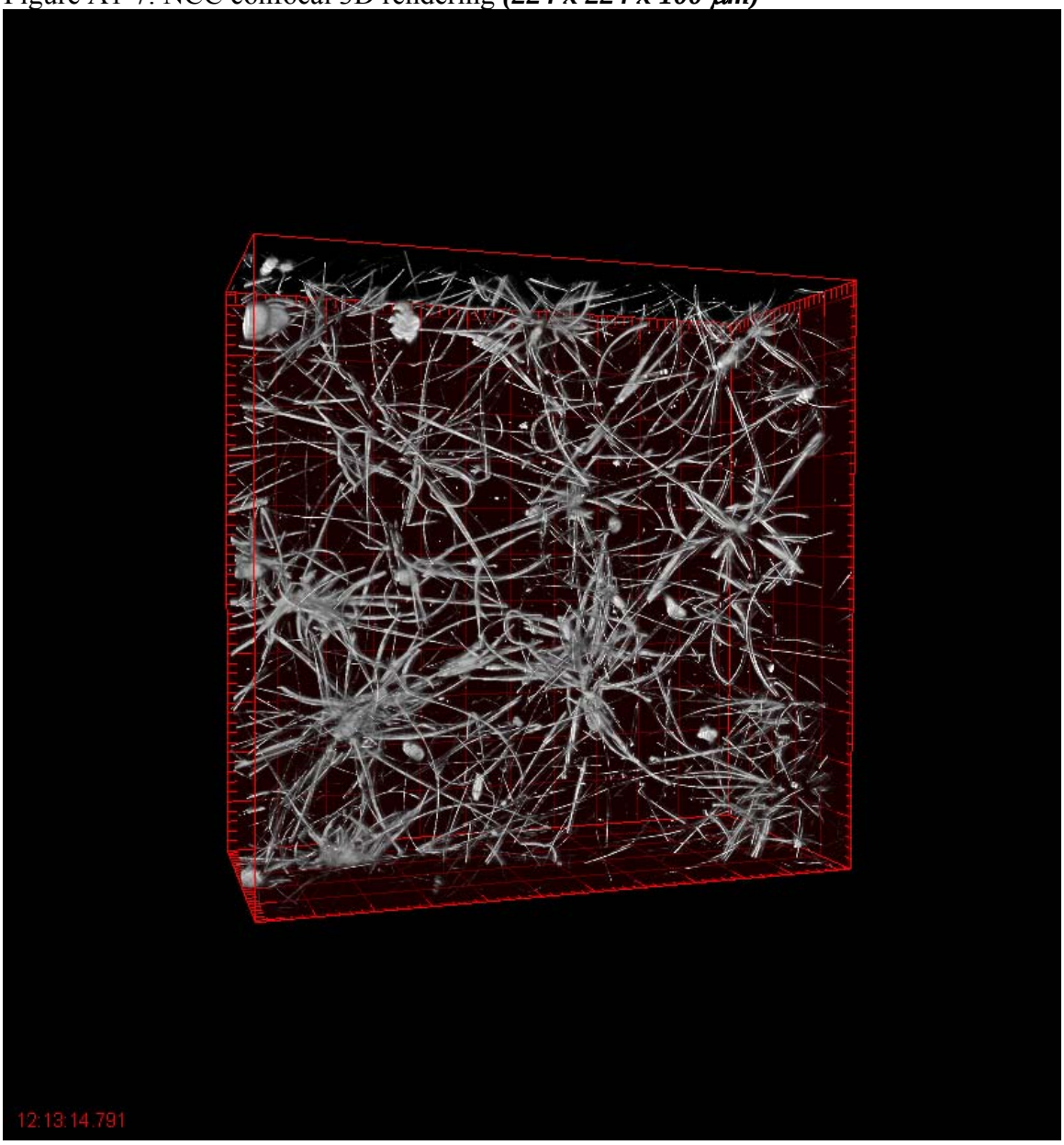

Figure A1-8. NCC#1 light micrograph ***(2.5 x 2.5 mm)***

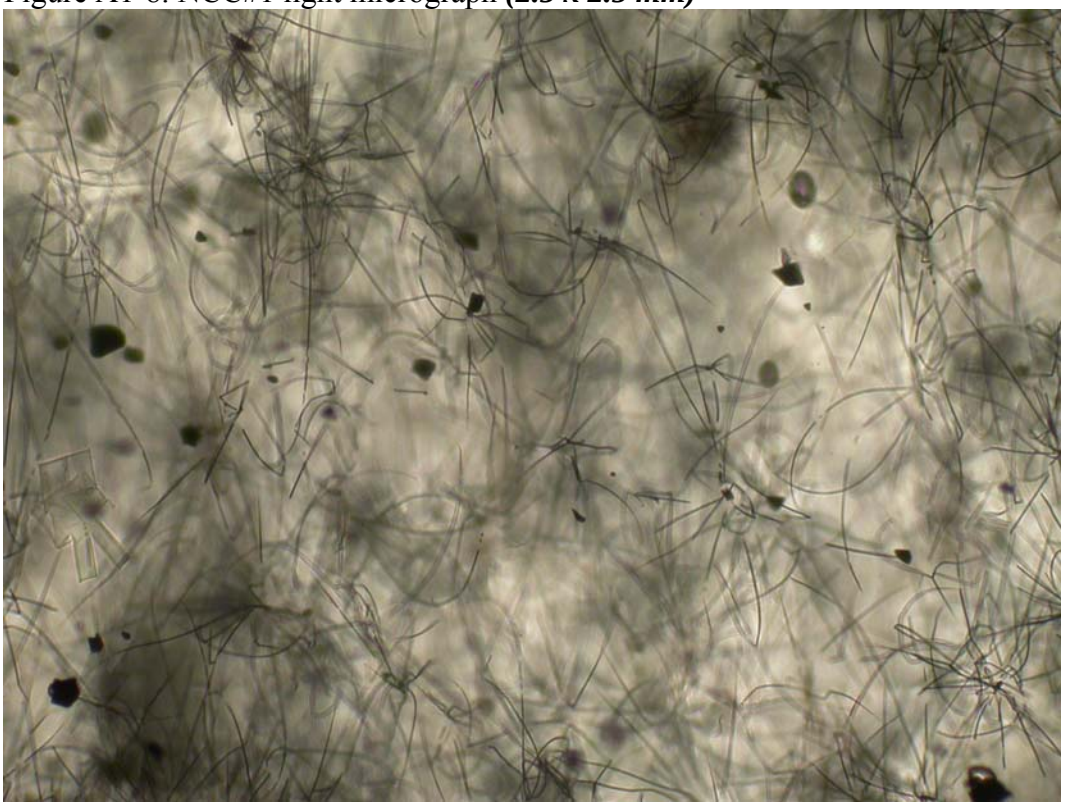

Figure A1-9. NCC#2 light micrograph ***(2.5 x 2.5 mm)***

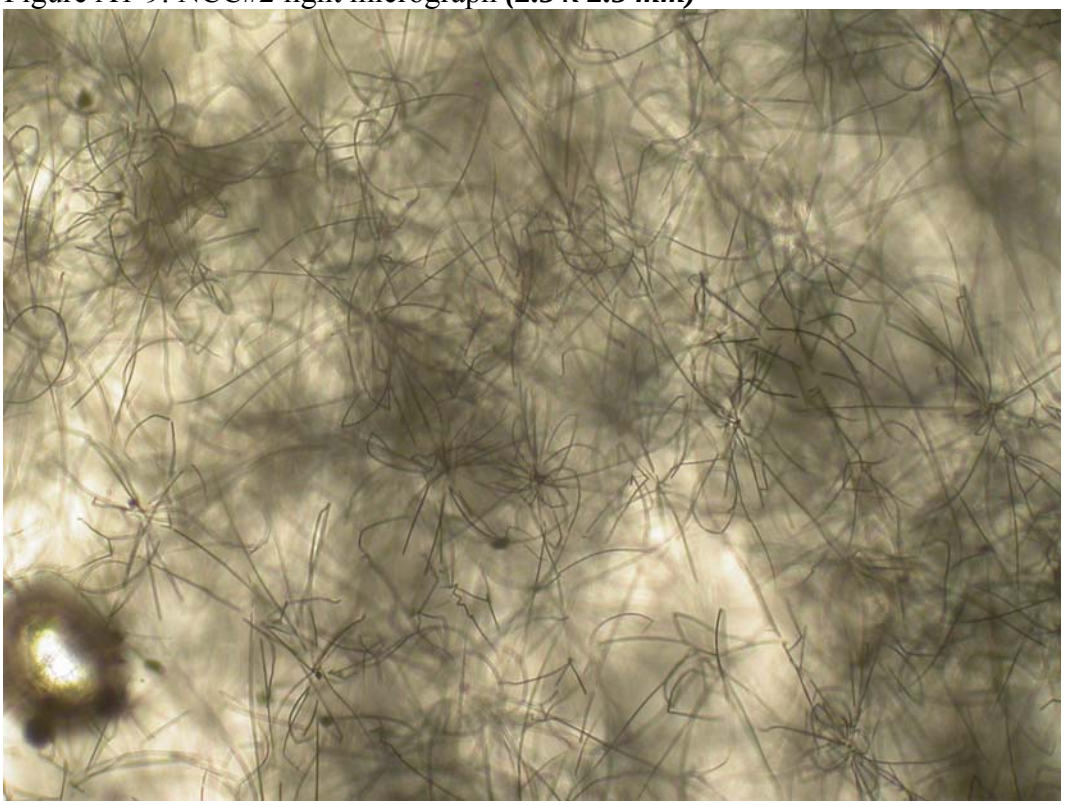

Figure A1-10. NCC#3 light micrograph ***(2.5 x 2.5 mm)***

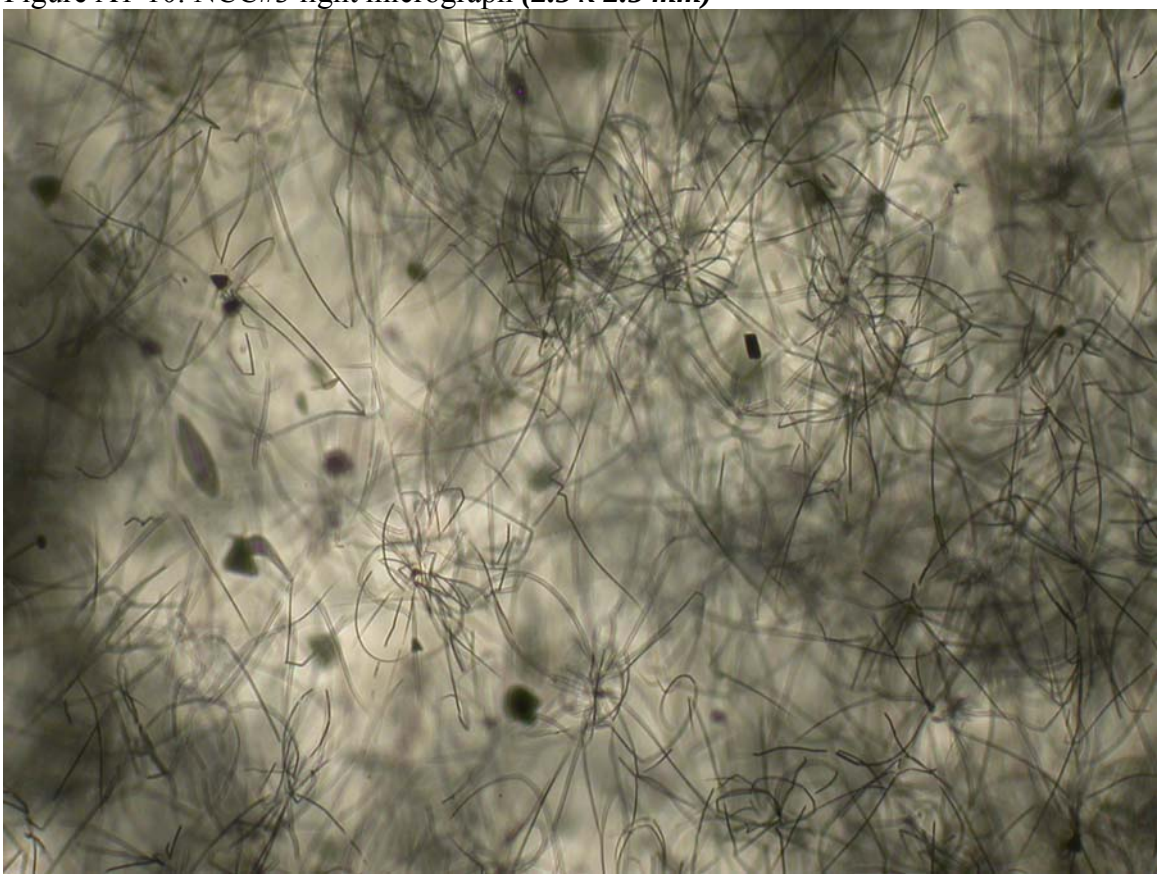

Figure A1-11. NWCA confocal 3D rendering ***(224 x 224 x 100 μm)***

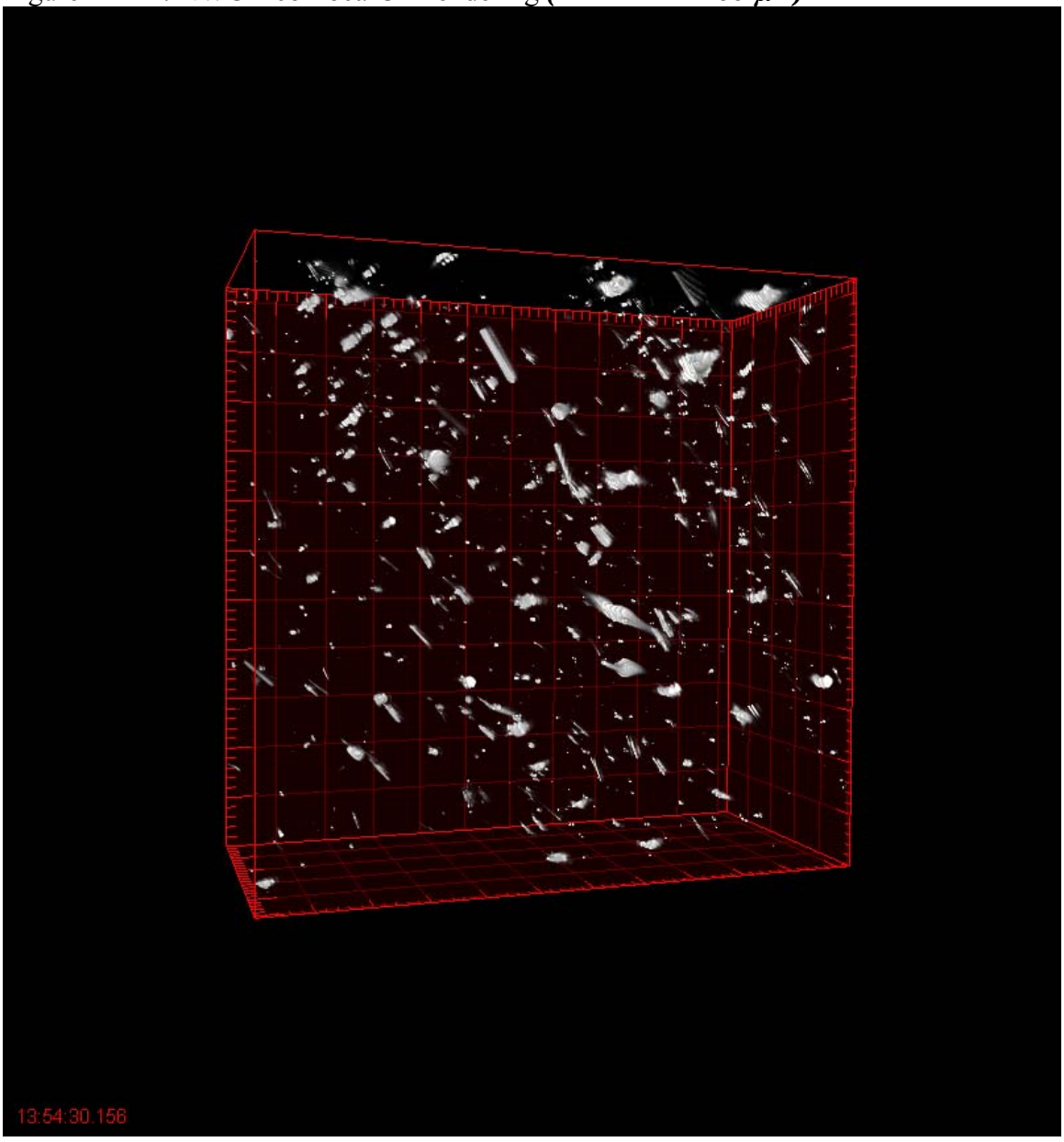

Figure A1-12. NWCA#1 light micrograph ***(2.5 x 2.5 mm)***

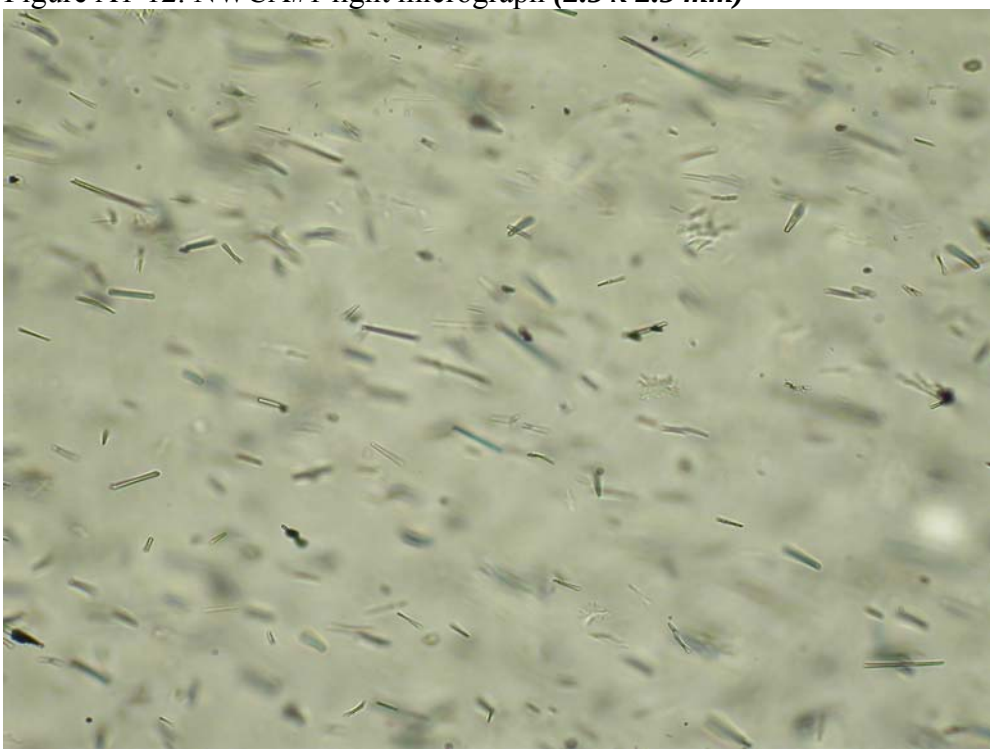

Figure A1-13. NWCA#2 light micrograph ***(2.5 x 2.5 mm)***

Figure A1-14. NWCA#3 light micrograph ***(2.5 x 2.5 mm)***

Figure A1-15. NWCA#4 light micrograph ***(2.5 x 2.5 mm)***

Figure A1-16. NWCB confocal 3D rendering ***(224 x 224 x 100 μm)***

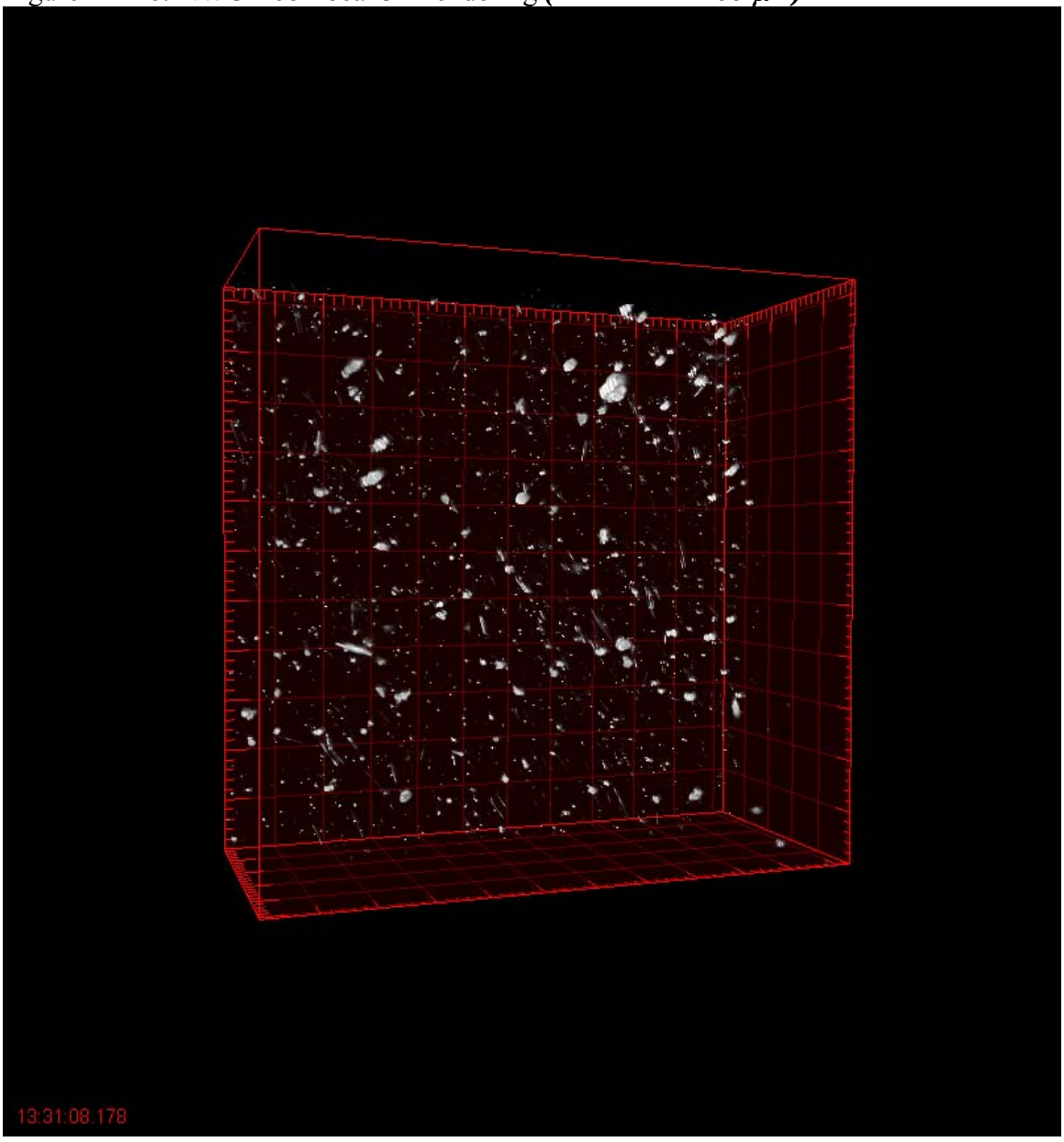

Figure A1-17. NWCB#1 light micrograph ***(2.5 x 2.5 mm)***

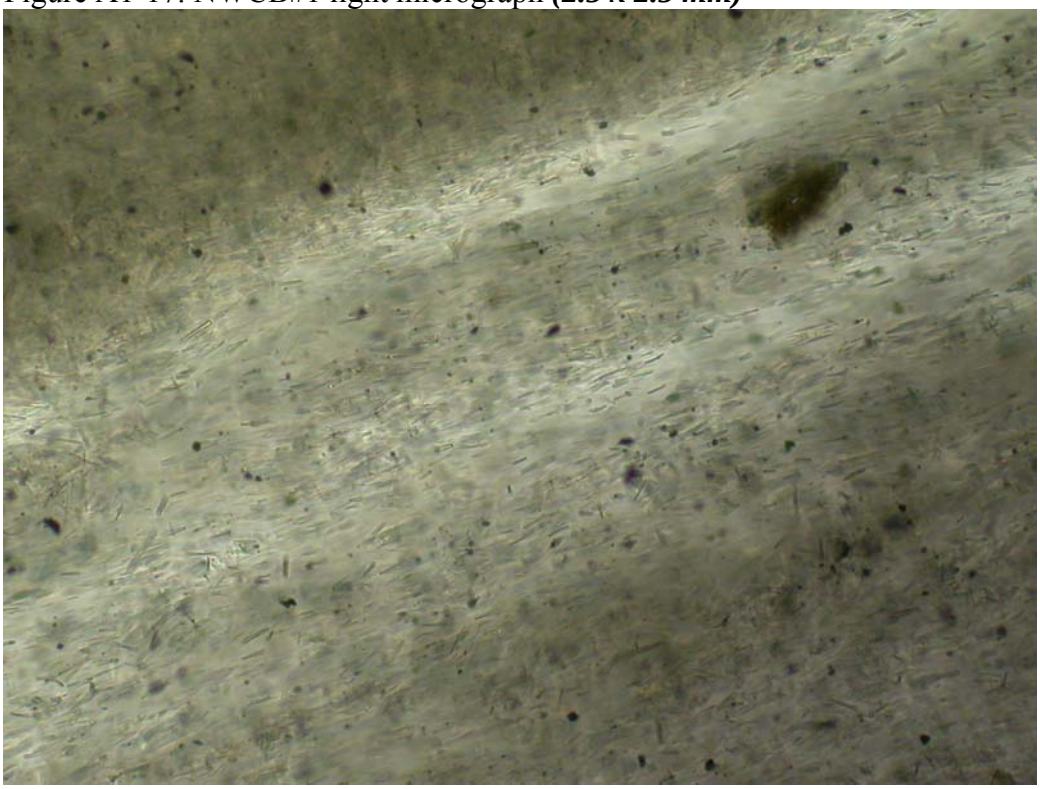

Figure A1-18. NWCB#2 light micrograph ***(2.5 x 2.5 mm)***

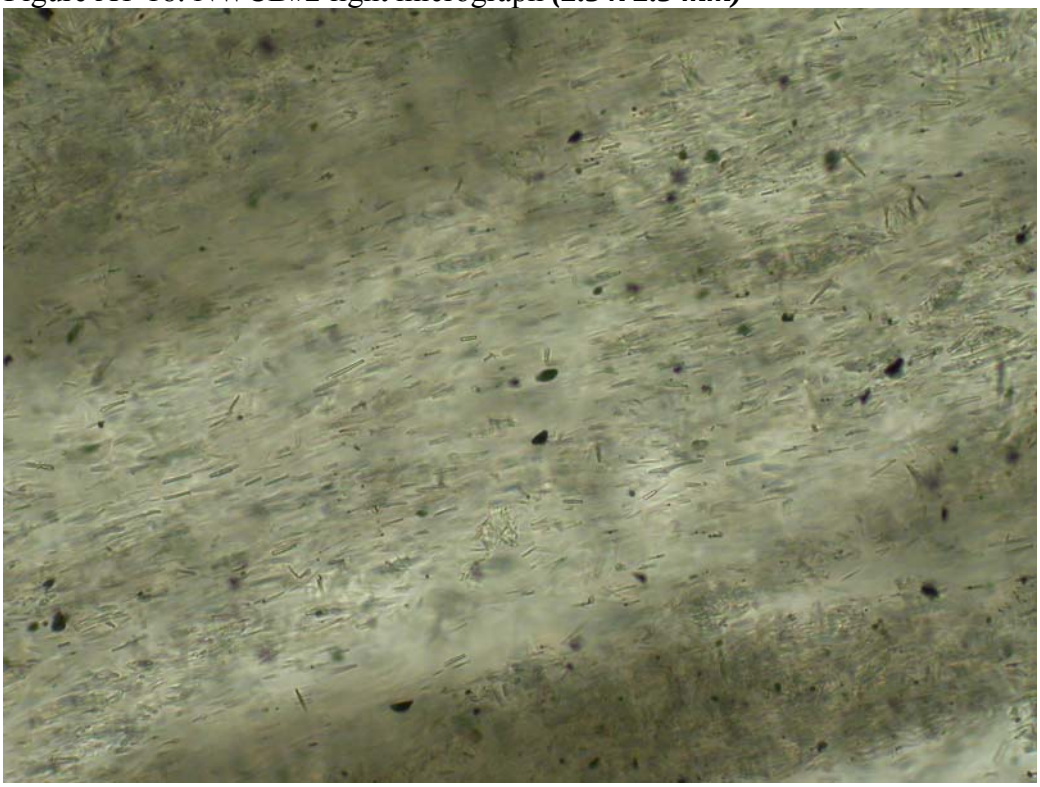

Figure A1-19. NWCB#3 light micrograph ***(2.5 x 2.5 mm)***

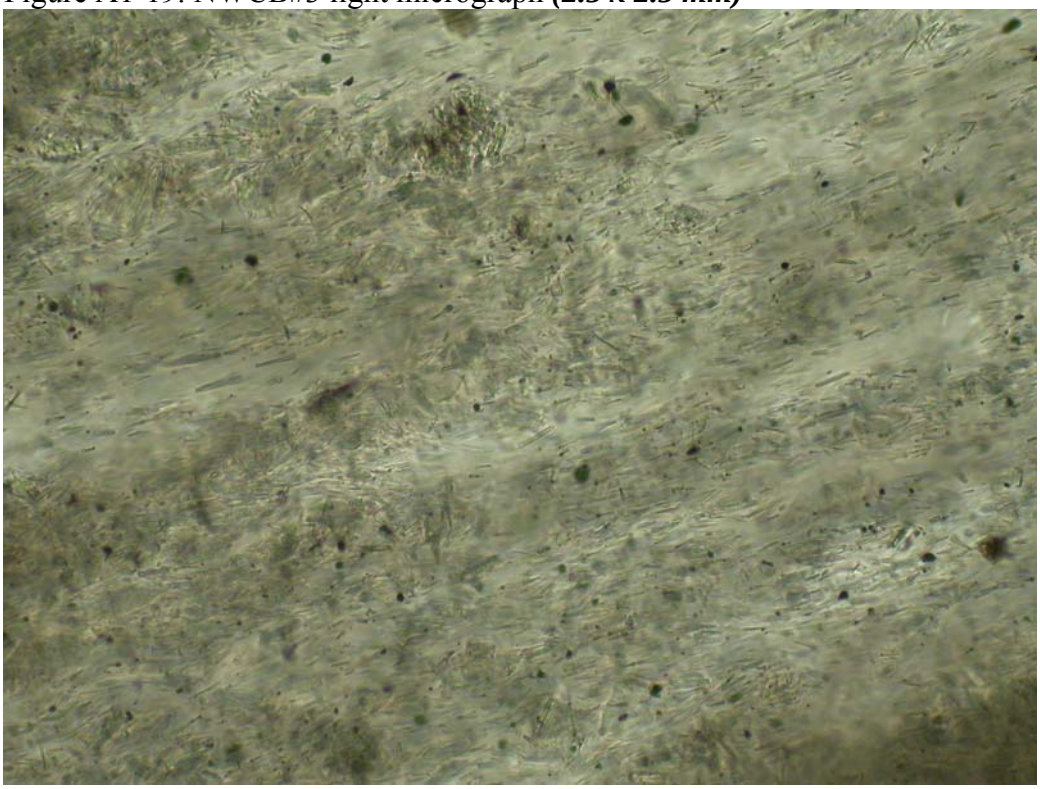

Figure A1-20. NWCB#4 light micrograph ***(2.5 x 2.5 mm)***

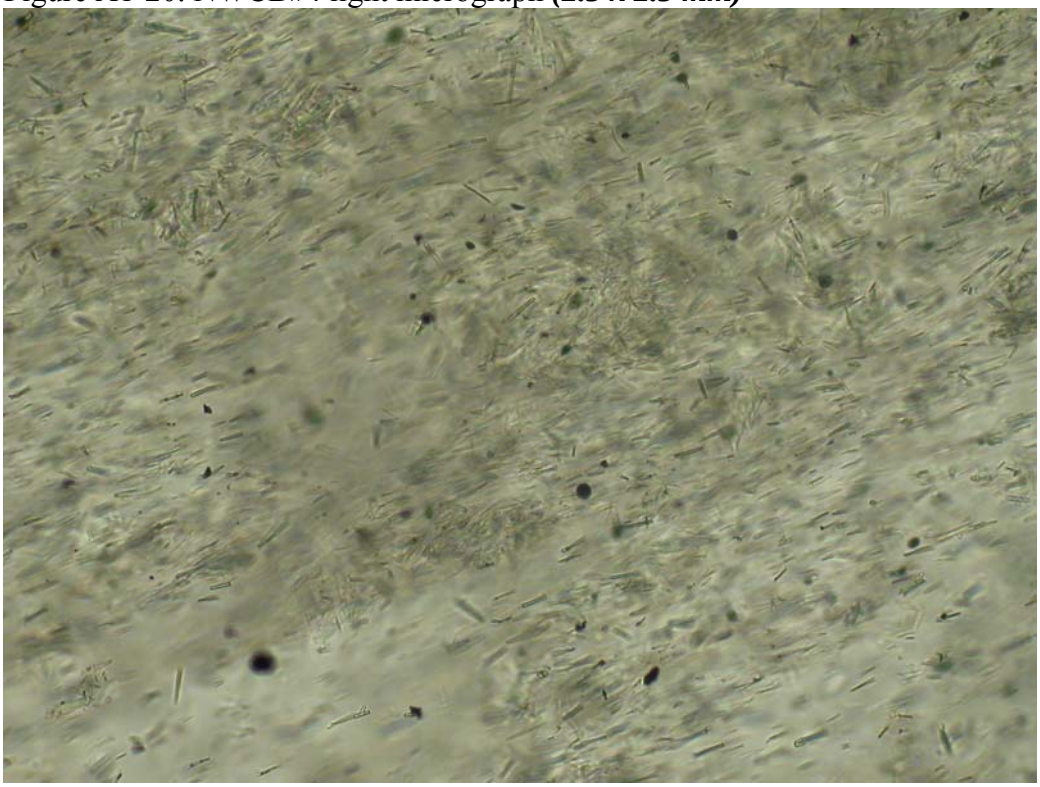

Figure A1-21. NWCC confocal3D rendering ***(224 x 224 x 100 μm)***

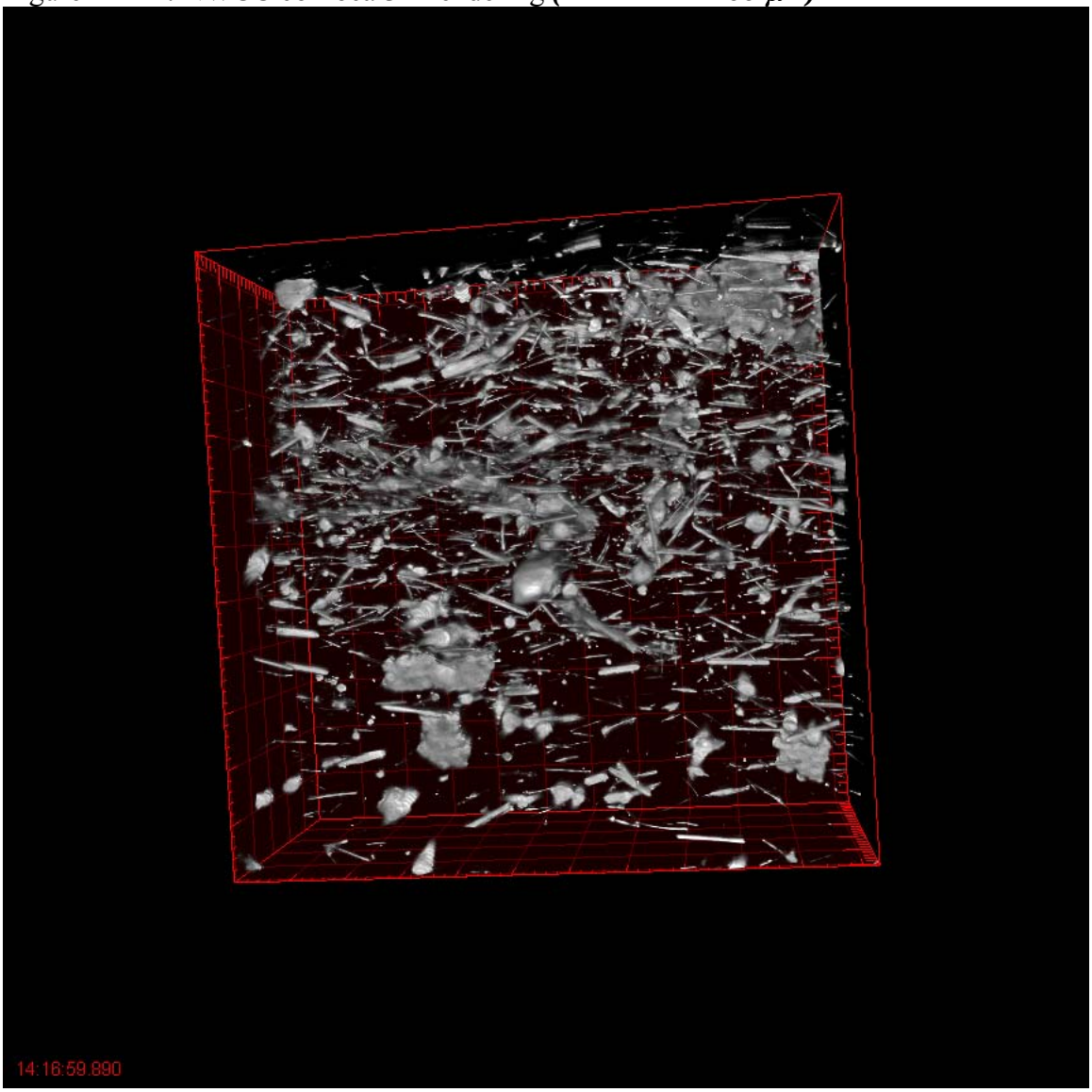

Figure A1-22. NWCC#1 light micrograph ***(2.5 x 2.5 mm)***

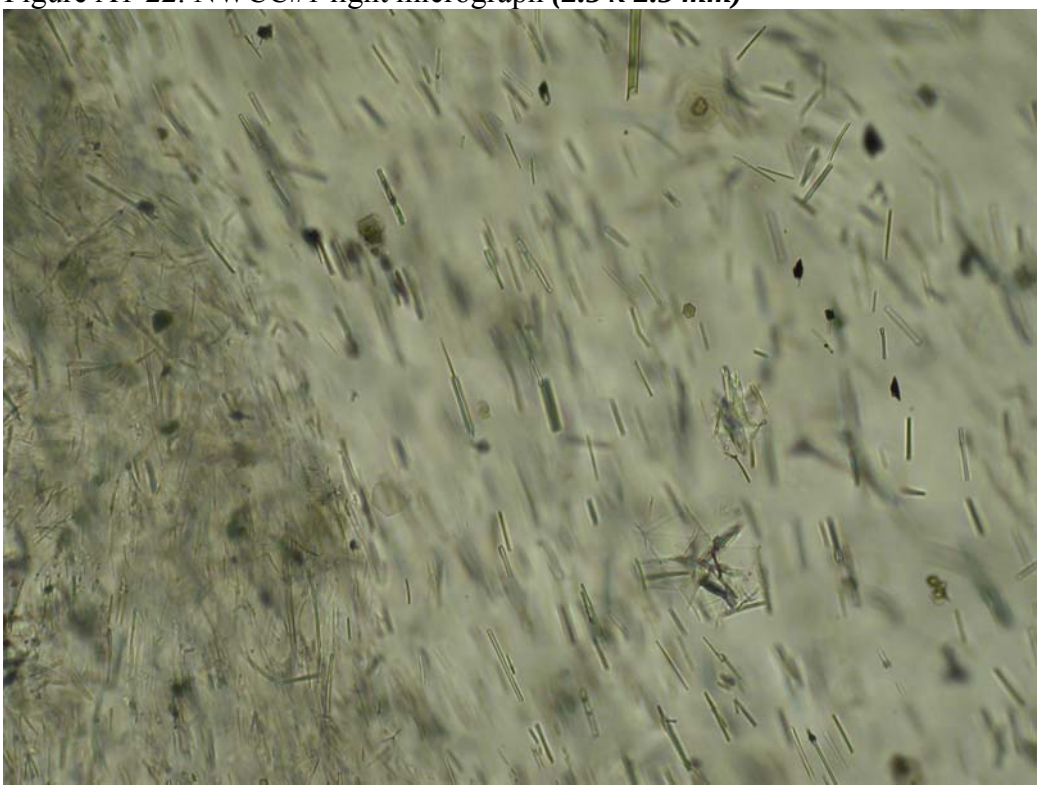

Figure A1-23. NWCC#2 light micrograph ***(2.5 x 2.5 mm)***

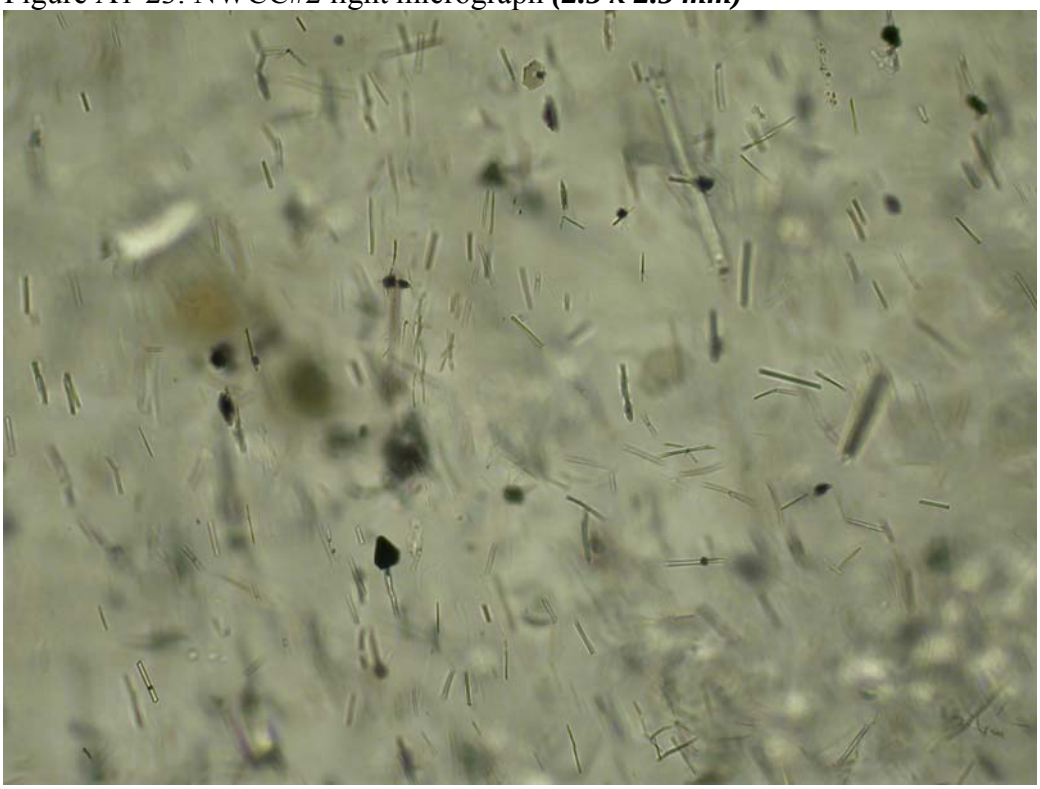

Figure A1-24. NWCC#3 light micrograph ***(2.5 x 2.5 mm)***

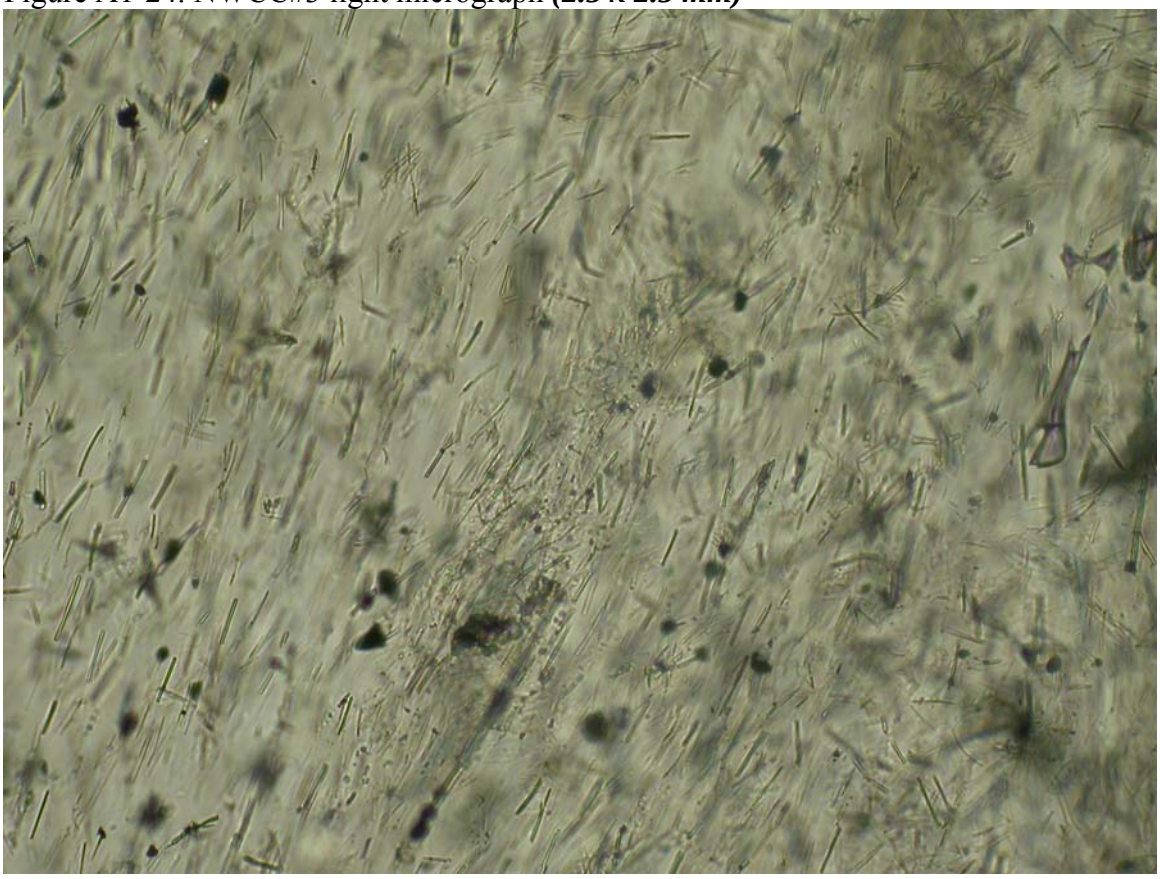

Figure A1-25. NWCE confocal 3D rendering ***(224 x 224 x 100 μm)***

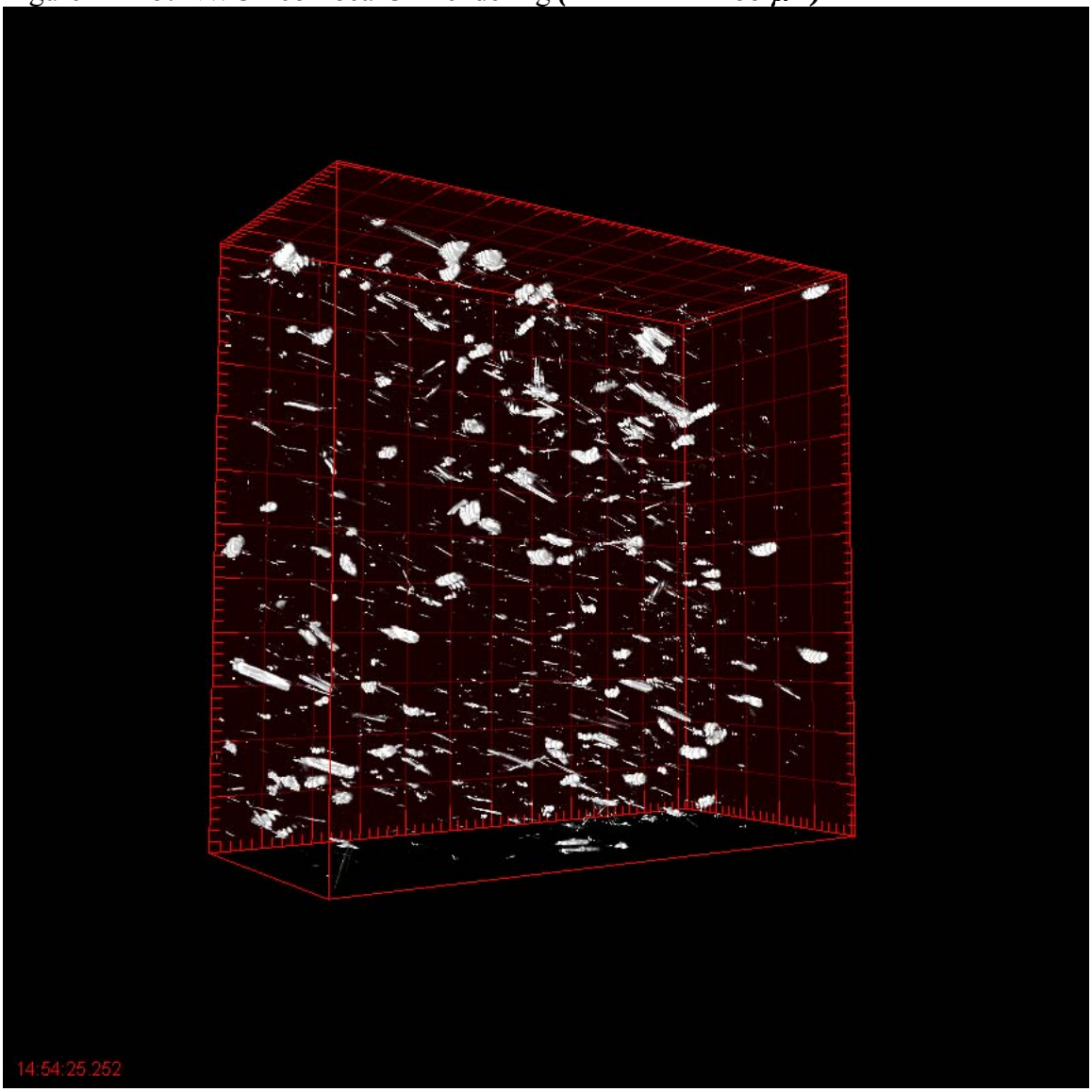

Figure A1-26. NWCE#1 light micrograph ***(2.5 x 2.5 mm)***

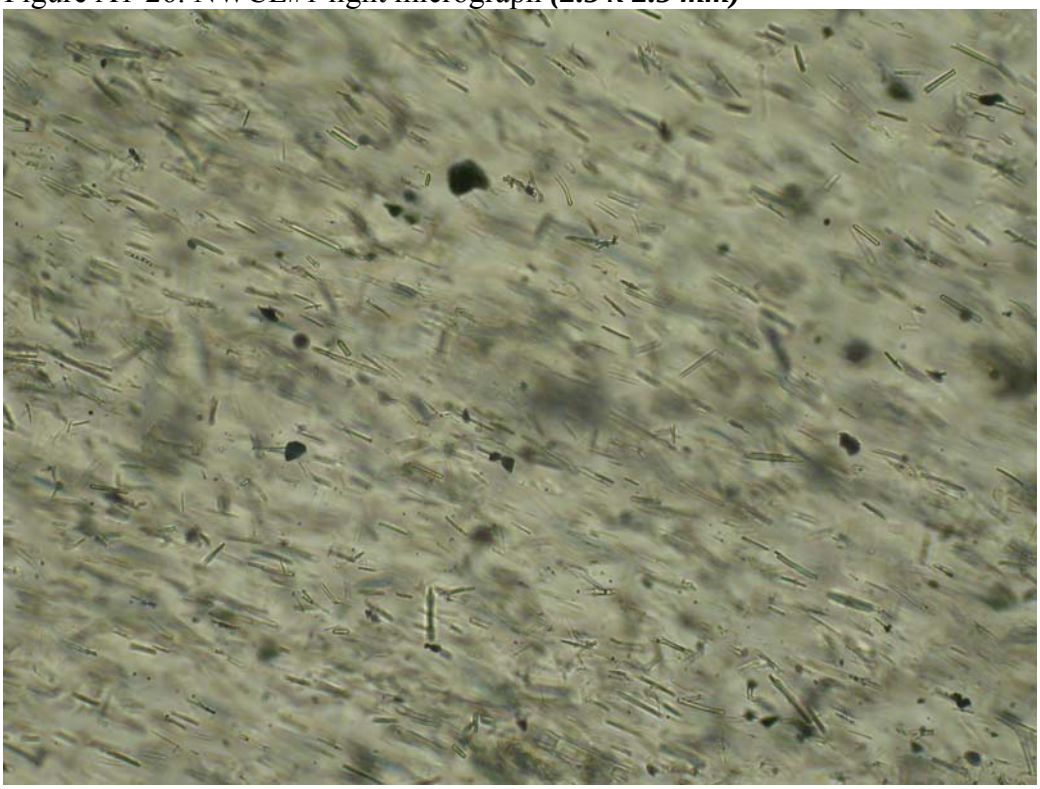

Figure A1-27. NWCE#2 light micrograph ***(2.5 x 2.5 mm)***

Figure A1-28. NWCE#3 light micrograph ***(2.5 x 2.5 mm)***

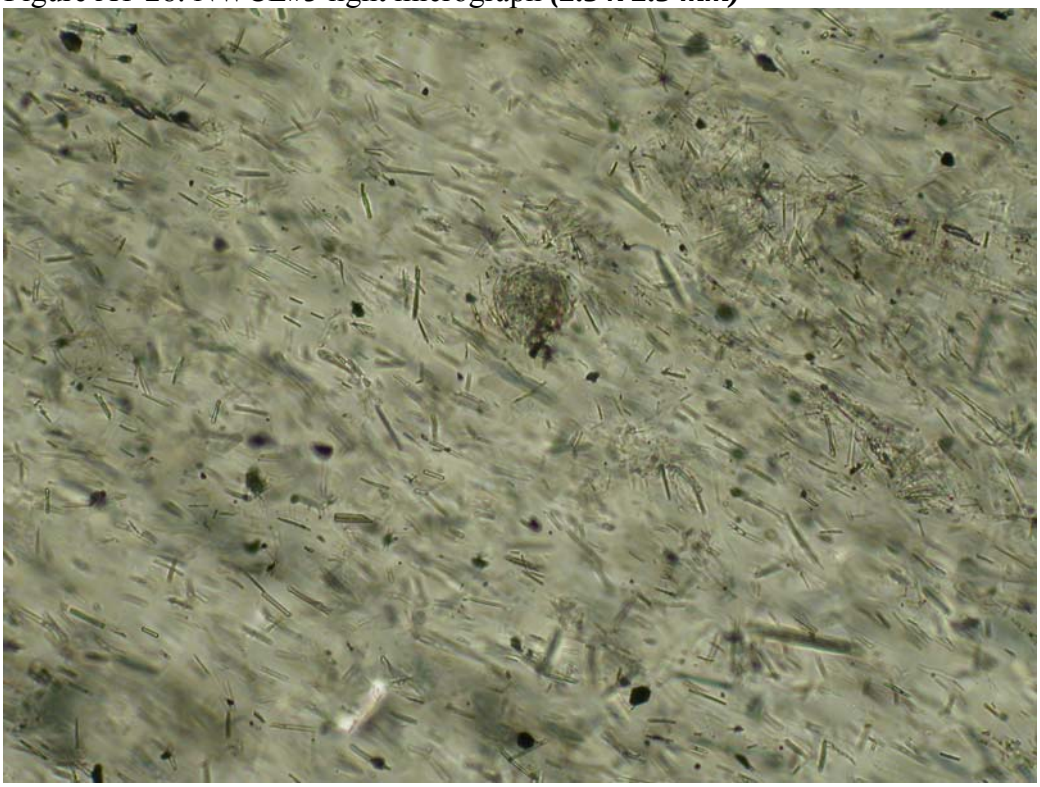

Figure A1-29. NWCE#4 light micrograph ***(2.5 x 2.5 mm)***

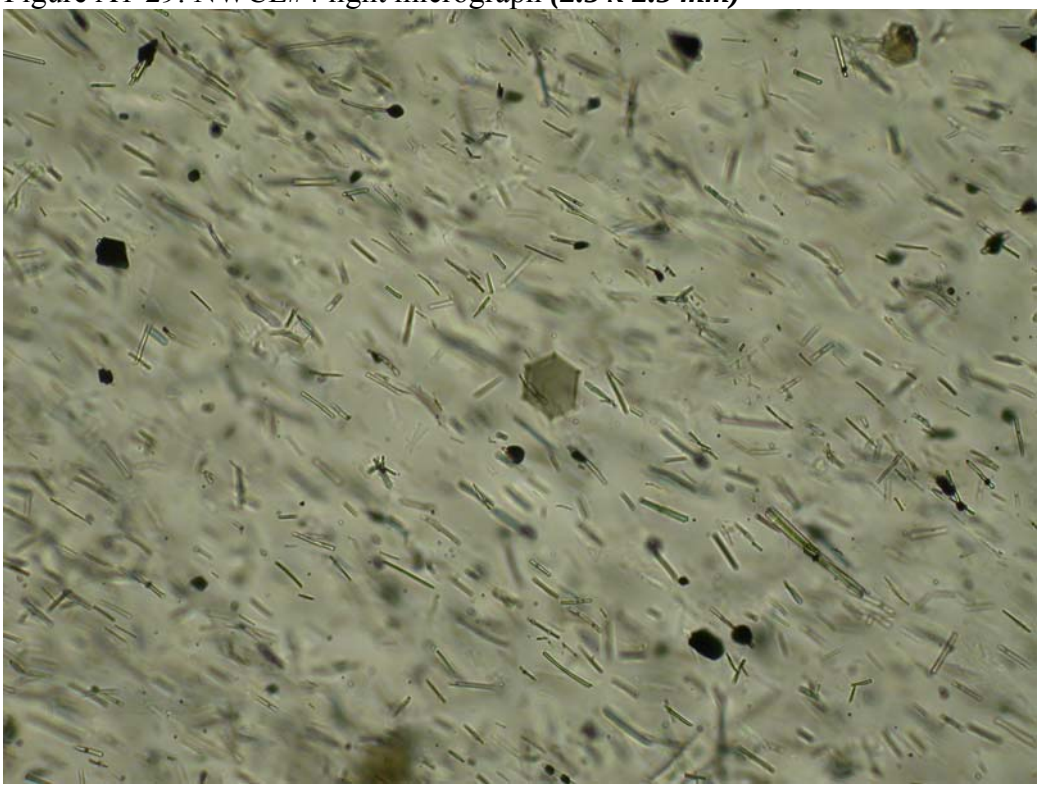

Figure A1-30. NWCF confocal 3D rendering ***(224 x 224 x 100 μm)***

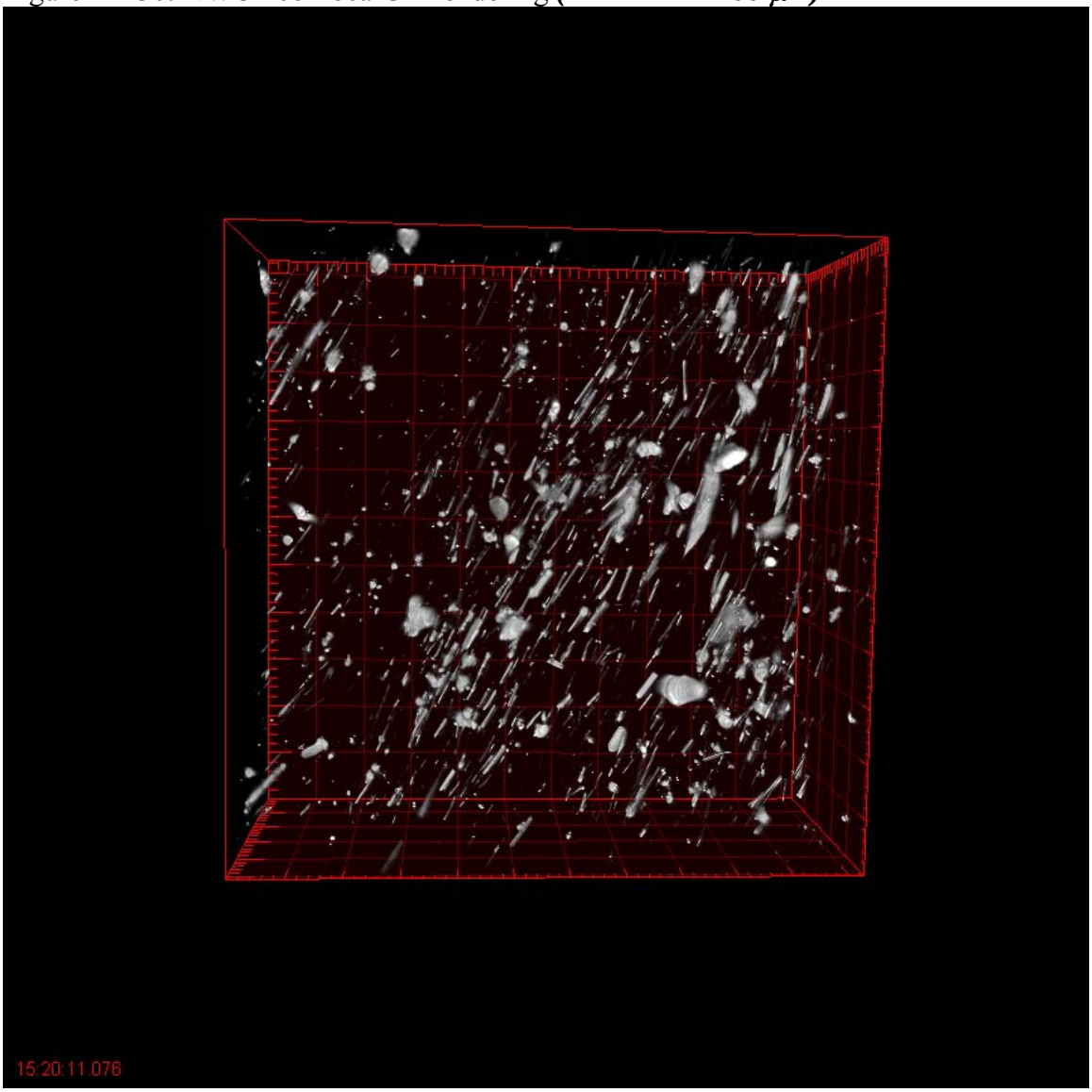

Figure A1-31. NWCF#1 light micrograph ***(2.5 x 2.5 mm)***

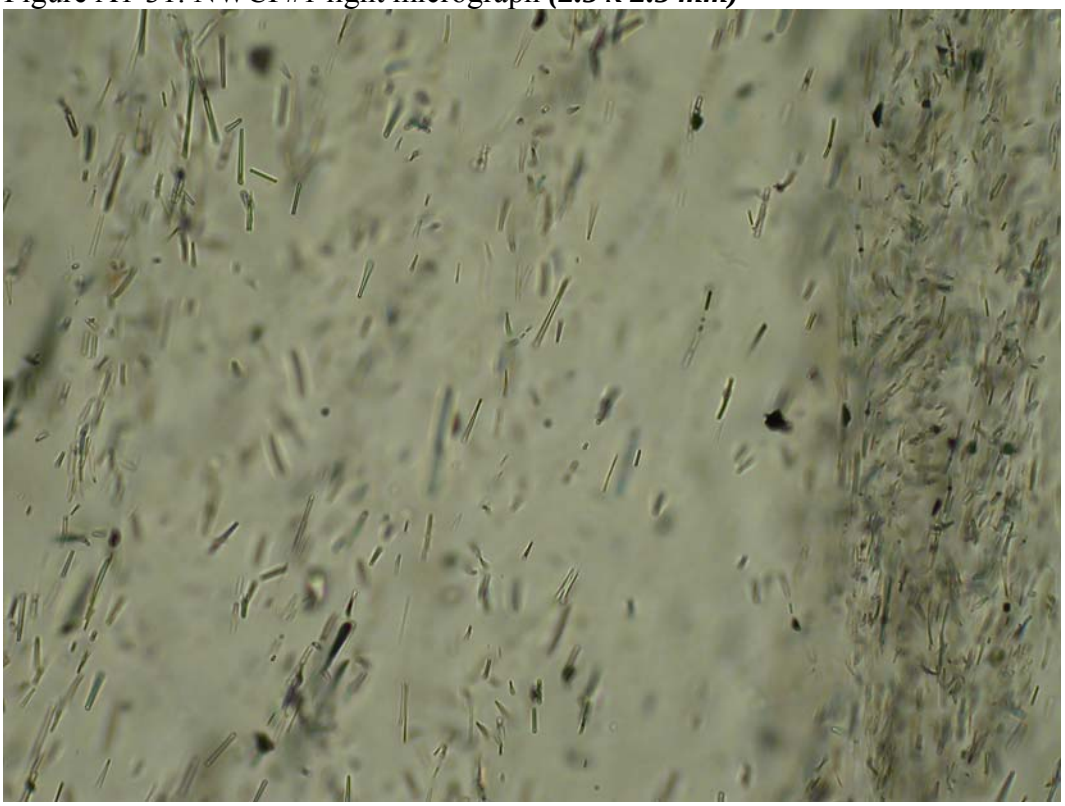

Figure A1-32. NWCF#2 light micrograph ***(2.5 x 2.5 mm)***

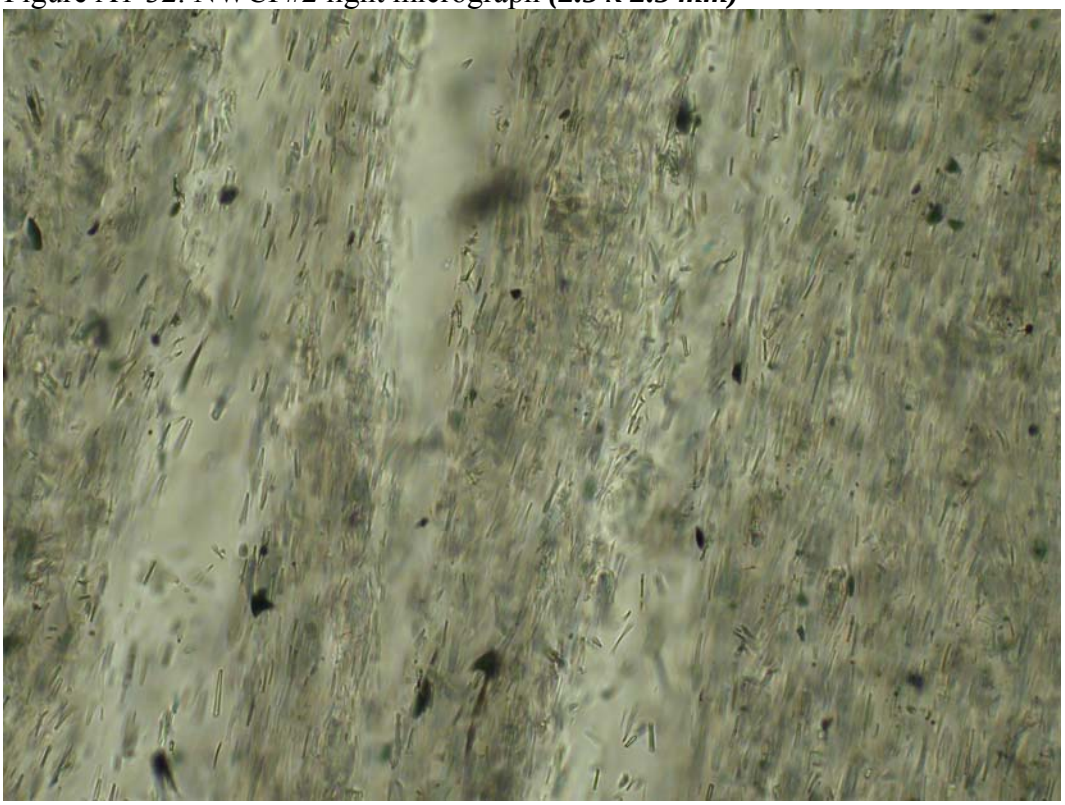

Figure A1-33. NWCF#3 light micrograph ***(2.5 x 2.5 mm)***

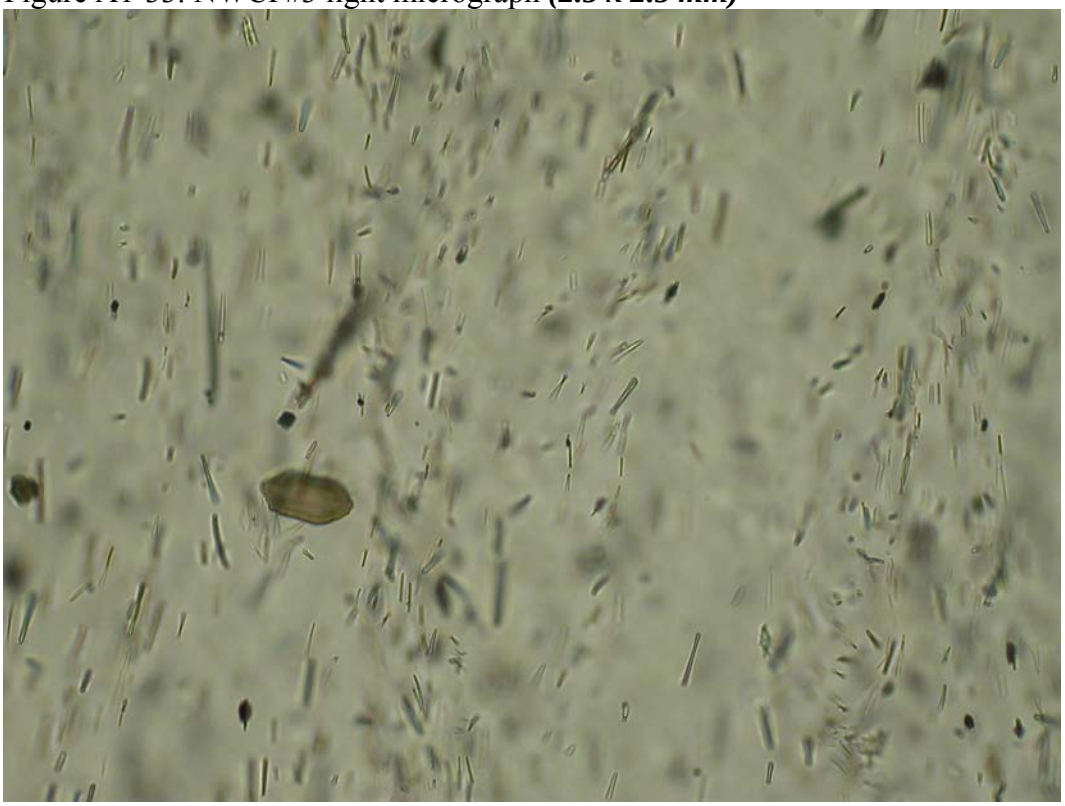

Figure A1-34. NWCF#4 light micrograph ***(2.5 x 2.5 mm)***

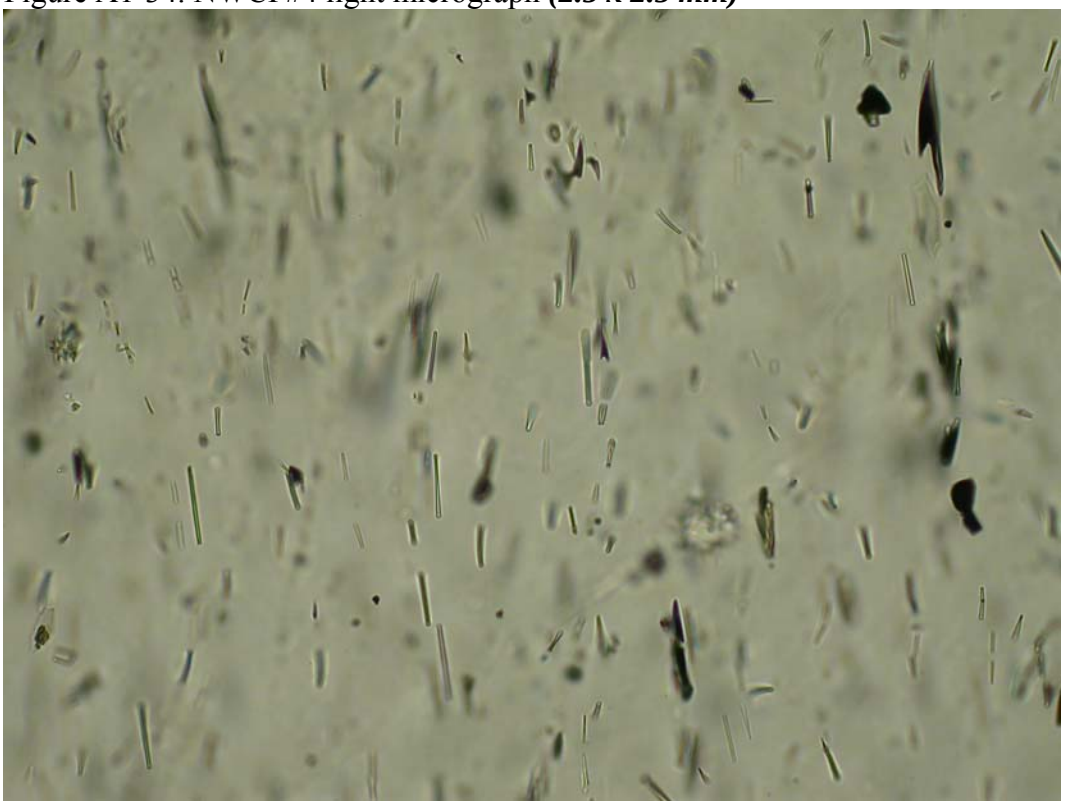

Figure A1-35. SCA confocal 3D rendering ***(224 x 224 x 100 μm)***

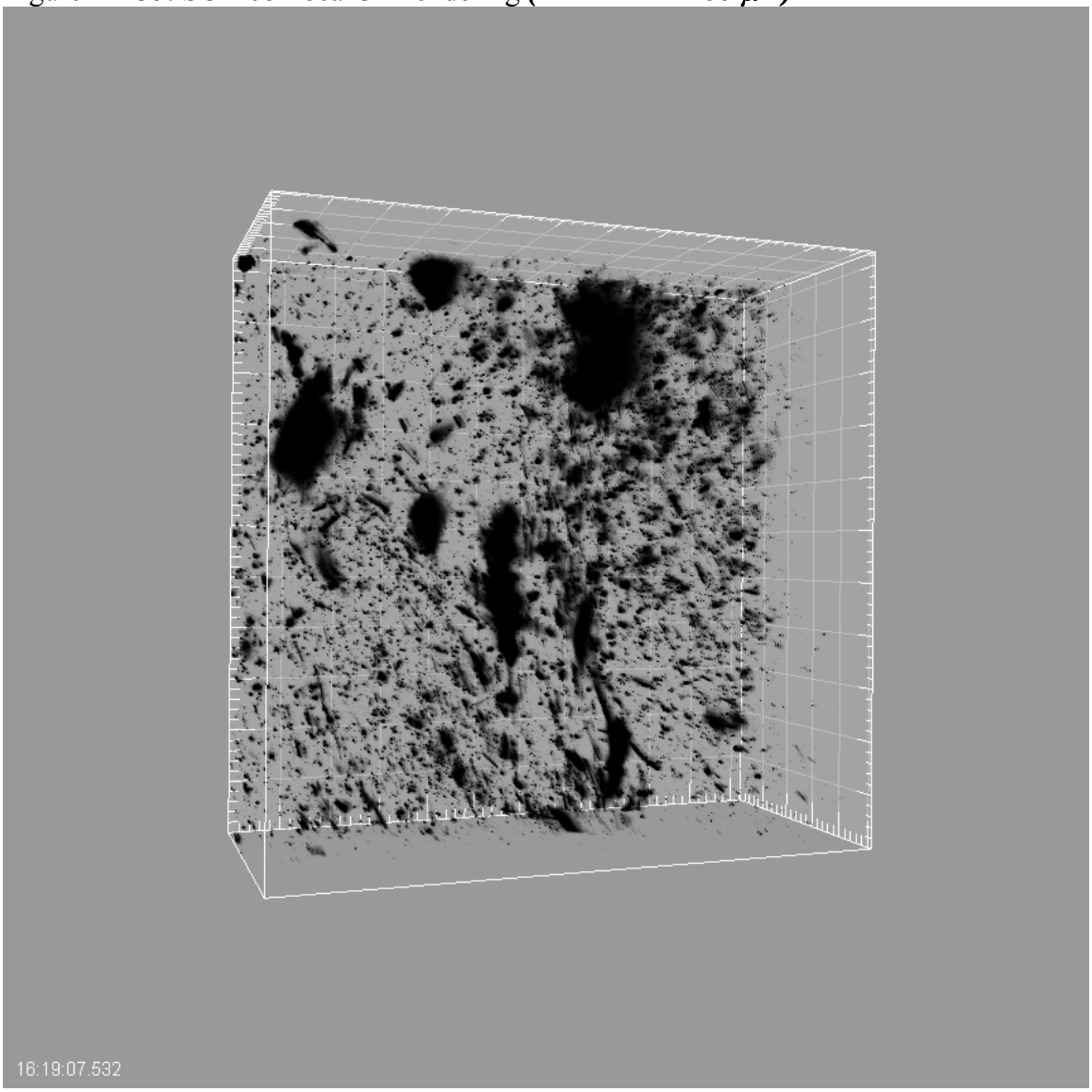

Figure A1-36. SCA#1 light micrograph ***(2.5 x 2.5 mm)***

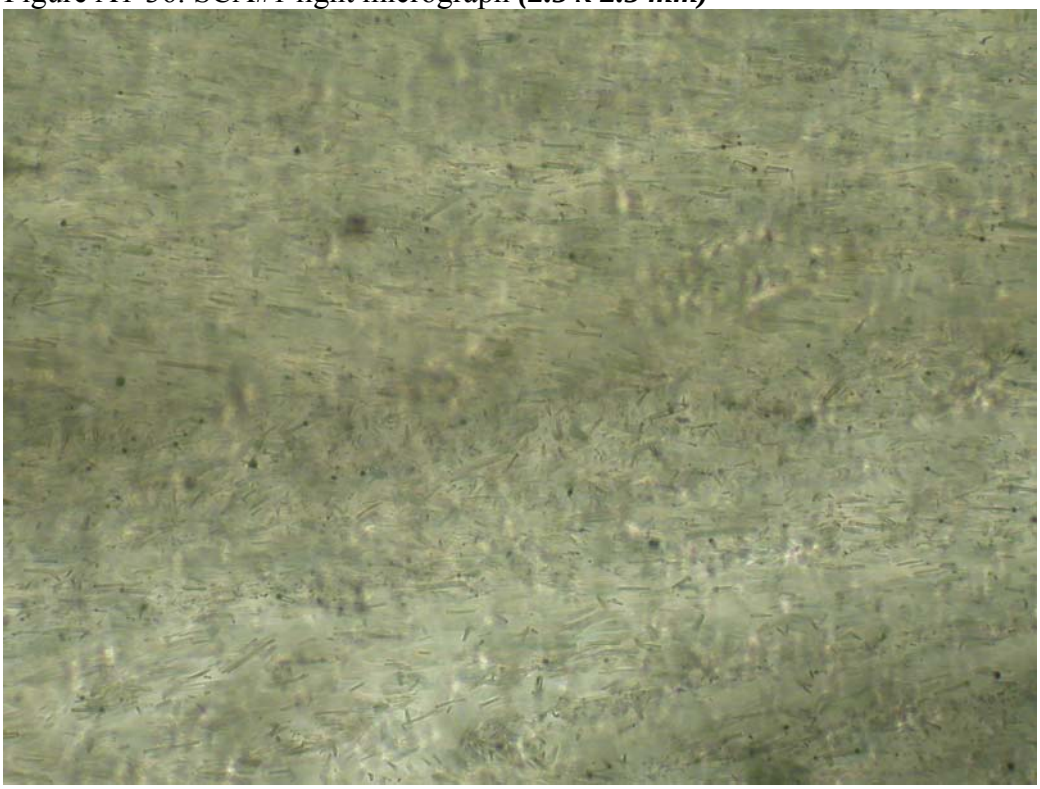

Figure A1-37. SCA#2 light micrograph ***(2.5 x 2.5 mm)***

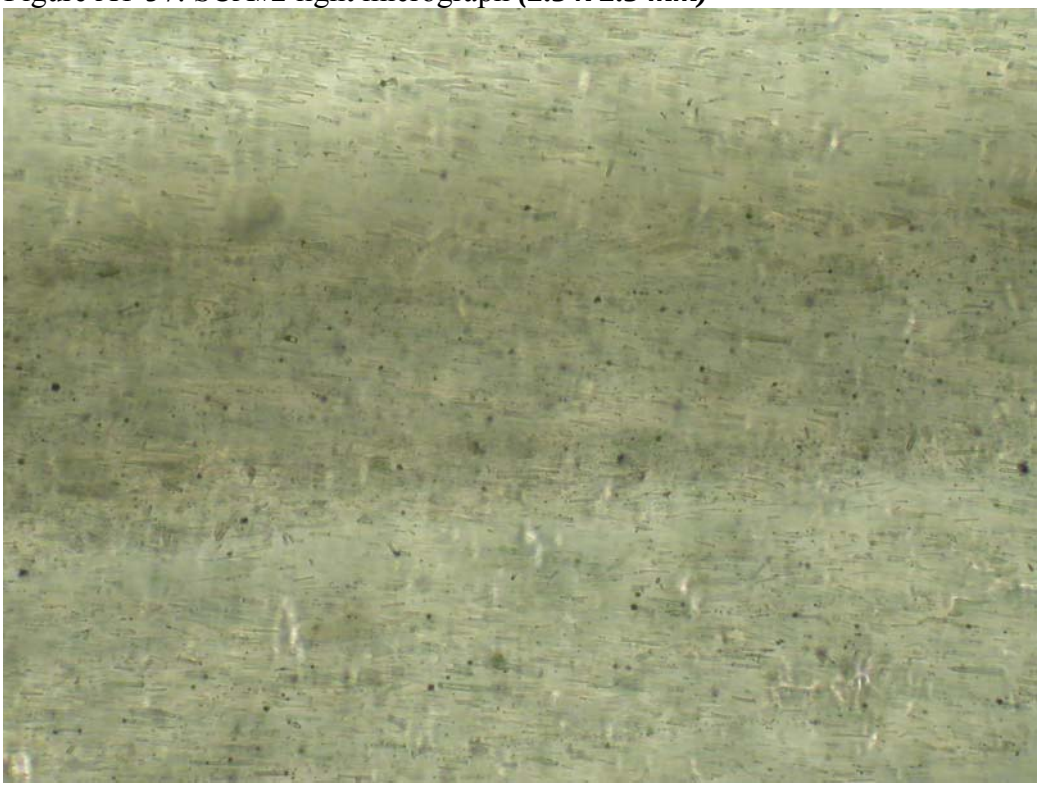

Figure A1-38. SCA#3 light micrograph ***(2.5 x 2.5 mm)***

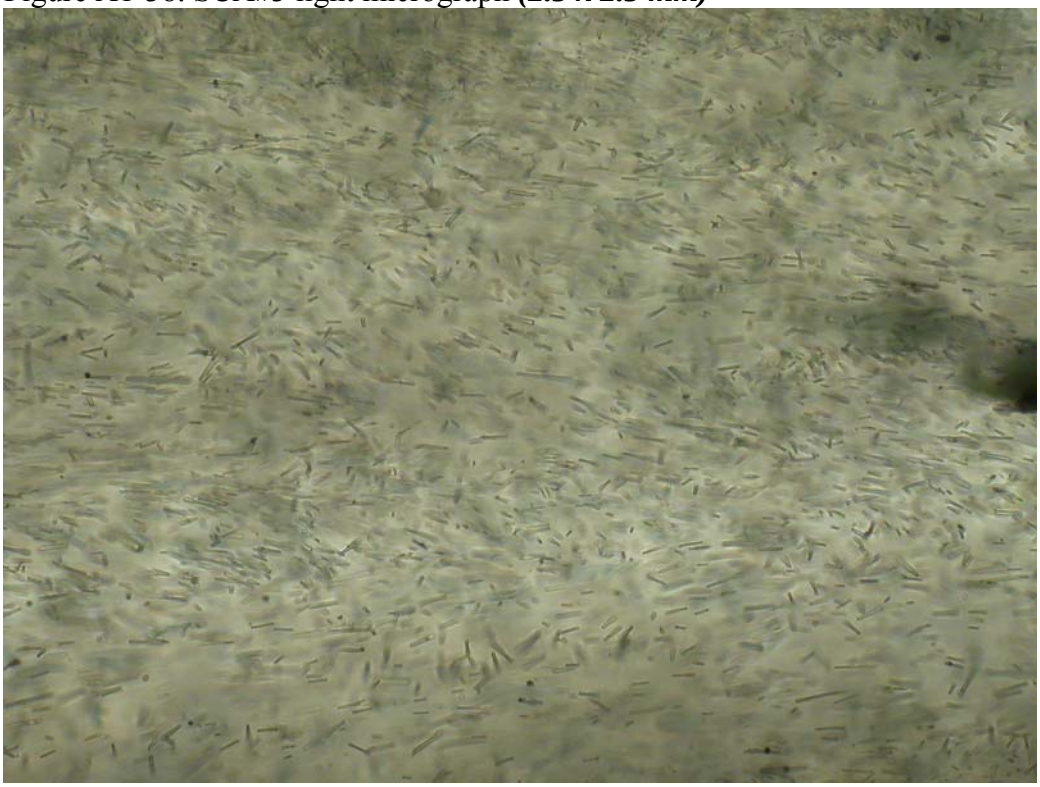

Figure A1-39. SCA#4 light micrograph ***(2.5 x 2.5 mm)***

Figure A1-40. SCE confocal 3D rendering ***(224 x 224 x 100 μm)***

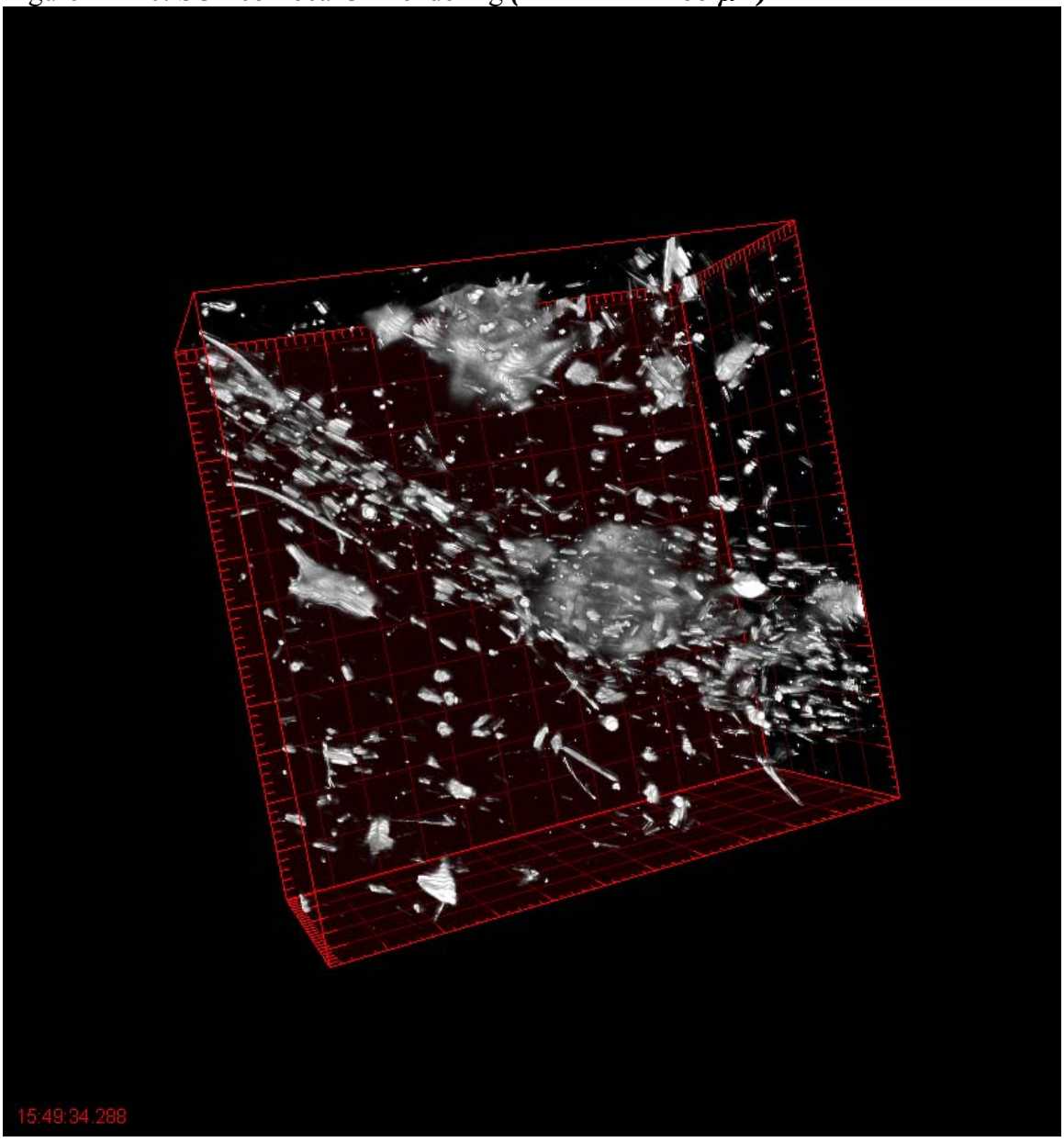

Figure A1-41. SCE#1 light micrograph ***(2.5 x 2.5 mm)***

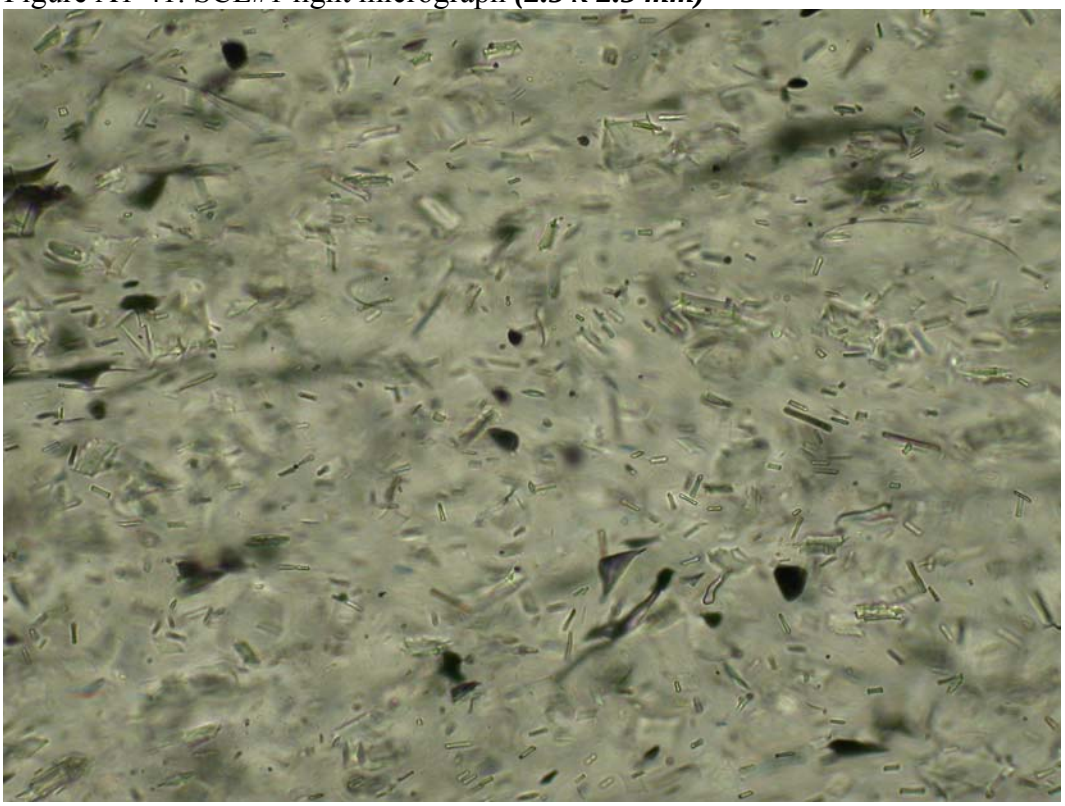

Figure A1-42. SCE#2 light micrograph ***(2.5 x 2.5 mm)***

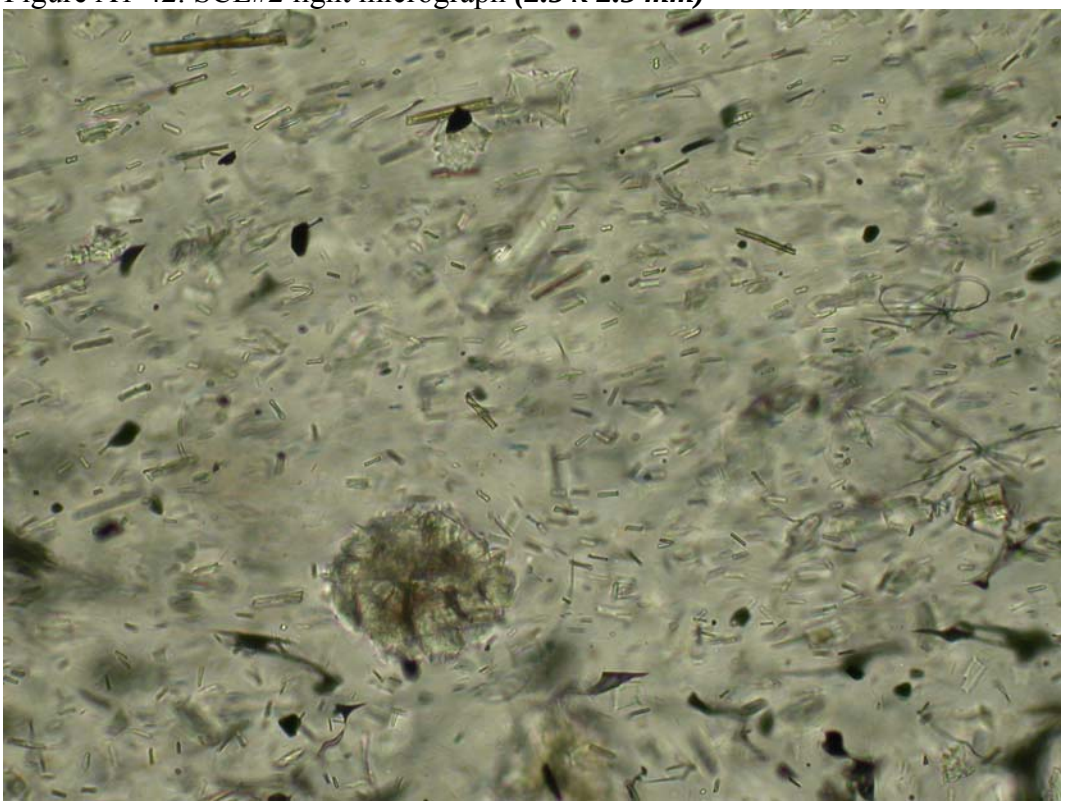

Figure A1-43. SCE#3 light micrograph ***(2.5 x 2.5 mm)***

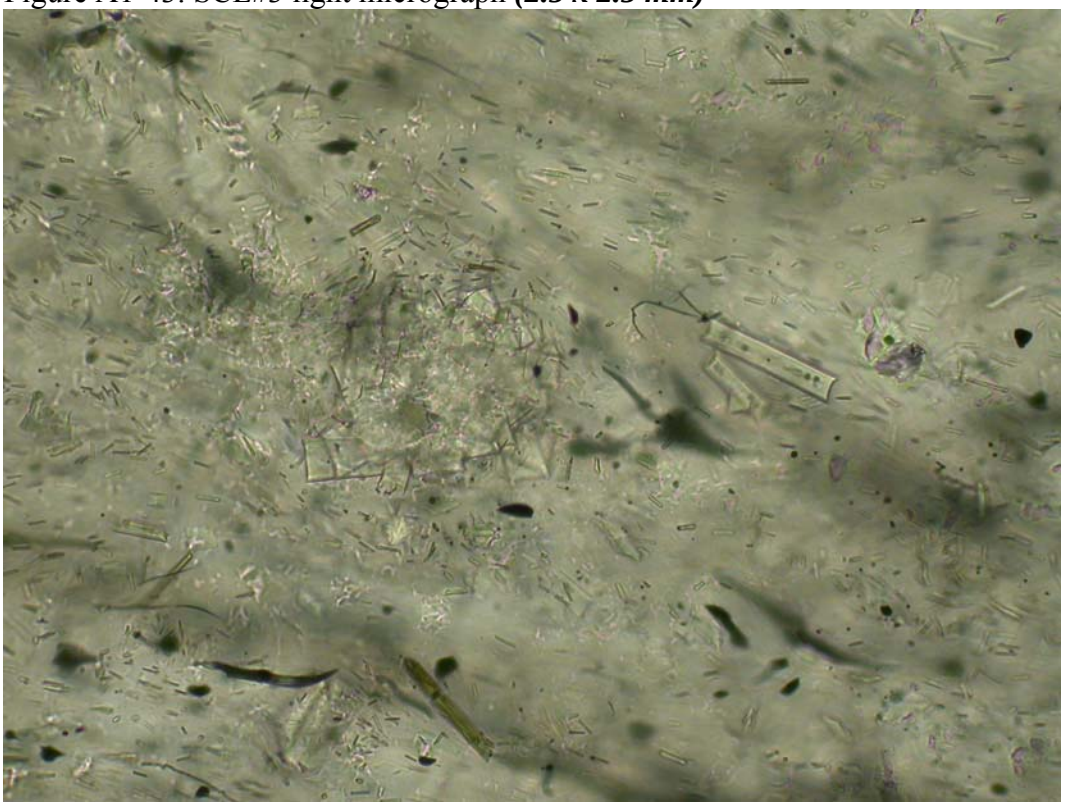

Figure A1-44. SCE#4 light micrograph ***(2.5 x 2.5 mm)***

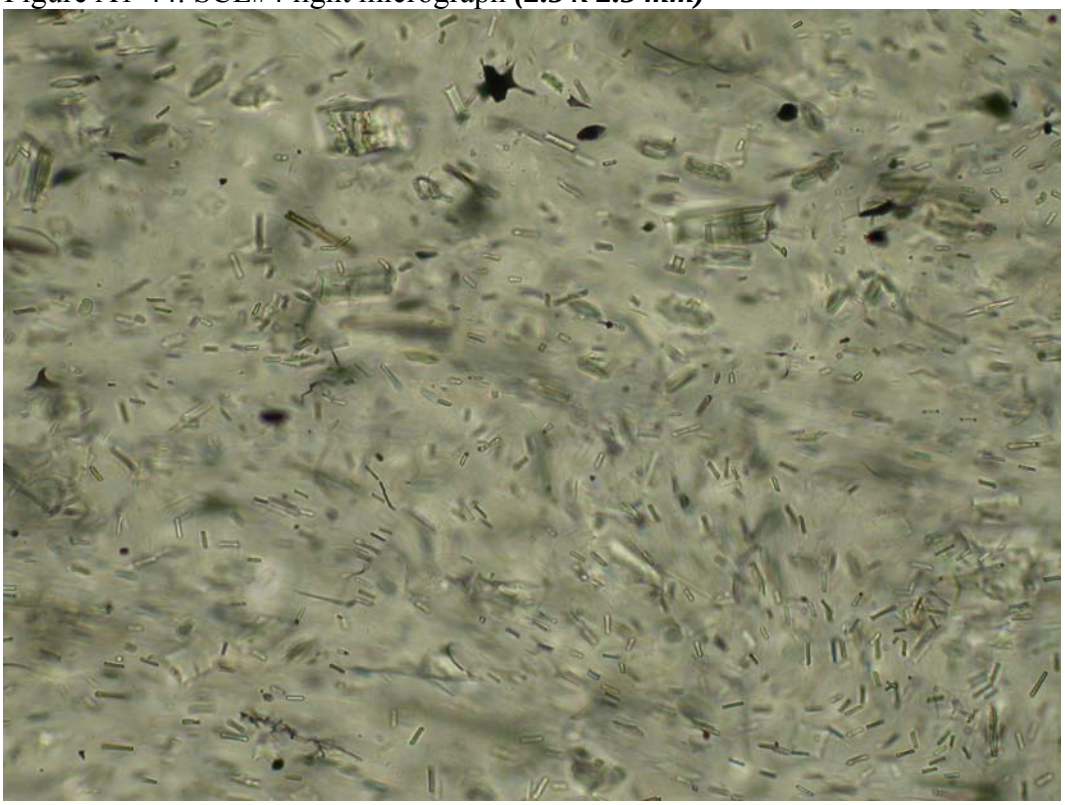

## Appendix B—Table of TVF Solutions for Individual Samples

Table A2-1: Constrained (A = -8.061) TVF values for each sample.

| Coulee | Sample | H2O wt% | A | B | C |
|---|---|---|---|---|---|
| SC | SCA | 1.120 | -8.061 | 15233 | 68.243 |
| | SCE | 0.095 | -8.061 | 20702 | -11.99 |
| NWC | NWCA1 | 0.704 | -8.061 | 16139 | 112.65 |
| | NWCA2 | 0.724 | -8.061 | 14898 | 163.47 |
| | NWCB1 | 0.705 | -8.061 | 18650 | 5.561 |
| | NWCC22 | 0.544 | -8.061 | 18336 | 41.015 |
| | NWCE | 0.637 | -8.061 | 19312 | -25.95 |
| | NWCF | 0.658 | -8.061 | 14451 | 173.31 |
| NC | NCA22 | 0.227 | -8.061 | 19088 | 28.948 |
| | NCA23 | 0.232 | -8.061 | 19575 | -1.715 |
| | NCA24 | 0.234 | -8.061 | 19783 | -16.78 |
| | NCA25 | 0.220 | -8.061 | 20008 | -20.94 |
| | NCA32 | 0.225 | -8.061 | 18246 | 78.09 |
| | NCC13 | 0.288 | -8.061 | 17371 | 108.75 |
| | NCC15 | 0.336 | -8.061 | 18802 | 0 |
| | NCC17 | 0.279 | -8.061 | 18095 | 75.438 |
| | NCC19 | 0.317 | -8.061 | 18916 | 24.535 |
| Remelt | SCEr(b)[a] | 0.066 | -8.061 | 21266 | -37.96 |
| | NWCEr(b)[a] | 0.062 | -8.061 | 20408 | 6.4616 |
| | SCEr[a] | 0.041 | -8.061 | 21641 | -35.85 |
| | NWCEr[a] | 0.042 | -8.061 | 21627 | -34.04 |
| | ASCEr[a] | 0.024 | -8.061 | 20559 | 61.253 |
| | ANWCEr[a] | 0.020 | -8.061 | 20073 | 84.572 |
| | ANCr[a] | 0.013 | -8.061 | 18877 | 172.65 |
| | ANCCr1[a] | 0.009 | -8.061 | 19956 | 108.71 |
| | ANCCr2[a] | 0.010 | -8.061 | 20207 | 88.389 |
| | ANCAr1 | 0.010 | -8.061 | 20723 | 36.432 |
| | ANCAr2 | 0.010 | -8.061 | 20723 | 36.432 |
| | ANCAr1pcc | 0.010 | -8.061 | 20723 | 36.432 |
| | ANCAr2pcc | 0.010 | -8.061 | 20723 | 36.432 |

[a]Alumina contaminated samples—not used in modeling.